Pontifícia Universidade Católica
do Rio de Janeiro

Vivian de Araújo Dornelas Nunes

Spatial organization of single-species populations

Tese de Doutorado

Thesis presented to the Programa de Pós-graduação em Física of PUC-Rio in partial fulfillment of the requirements for the degree of Doutor em Ciências - Física.

Advisor: Prof. Celia Beatriz Anteneodo de Porto

Rio de Janeiro
April 2020

Pontifícia Universidade Católica
do Rio de Janeiro

Vivian de Araújo Dornelas Nunes

Spatial organization of single-species populations

Thesis presented to the Programa de Pós-graduação em Física of PUC-Rio in partial fulfillment of the requirements for the degree of Doutor em Ciências - Física. Approved by the Examination Committee:

Prof. Celia Beatriz Anteneodo de Porto
Advisor
Departamento de Física – PUC-Rio

Prof. Alexandre Souto Martinez
USP

Prof. Ricardo Martinez Garcia
Fundação Instituto de Física Teórica

Prof. Daniel Adrian Stariolo
UFF

Prof. Edgardo Brigatti
UFRJ

Prof. Lucianno Augusto Coddato Antunes e Defaveri
Departamento de física – PUC-Rio

Rio de Janeiro, April 30th, 2020

Vivian de Araújo Dornelas Nunes

Received her bachelor in Physics from the Universidade Federal Fluminense (Rio de Janeiro, Brazil) in 2013 and her Master's Degree from the Pontifícia Universidade Católica do Rio de Janeiro (Rio de Janeiro, Brazil) in 2015. Research interests include topics in complex systems with application to biological problems, such as population dynamics and pattern formation.

Bibliographic data

Dornelas, Vivian

Spatial organization of single-species populations / Vivian de Araújo Dornelas Nunes; advisor: Celia Beatriz Anteneodo de Porto. – Rio de Janeiro: PUC-Rio, Departamento de Física, 2020.

93 f: il. color. ; 30 cm

1. Tese (doutorado) - Pontifícia Universidade Católica do Rio de Janeiro, Departamento de Física.

Inclui referências bibliográficas.

1. Física – Teses. 2. Dinâmica de populações. 3. Auto-organização. 4. Formação de padrões. 5. Difusão não linear. I. Anteneodo, Celia. II. Pontifícia Universidade Católica do Rio de Janeiro. Departamento de Física. III. Título.

CDD: 530

Acknowledgments

I wish to express my sincere appreciation to my advisor Celia Anteneodo for her conversations and guidance, for her support in this work, and for being always present and accessible. She is an inspiration in my career.

I am thankful to Eduardo Colombo for his collaboration with this work, for his patience and clarifications and for always being available to help me.

To the professors Alexandre Martinez, Daniel Stariolo, Edgardo Brigatti, Lucianno Defaveri, and Ricardo Garcia, I thank you for being part of the evaluation committee of this thesis. I also thank you for reading and discussing the present work.

I thank all the participants of the PUC-Rio Complex Systems research group for the motivating exchange of information. I am also thankful for the dedication of all the professors and staff personnel in the physics department of PUC-Rio.

Nothing would be possible without my husband, Renan, I would like to thank you for always being there, for helping me to remain calm even at the most desperate moments, for being my companion and for all the discussions about physics.

I wish to acknowledge the support and great love of my parents, my sisters, and my nephews. They kept me going on and provided me unique moments of relaxation.

I am grateful for the constant presence of my friends, who walk with me, helping to make the days lighter.

This study was financed in part by the Coordenação de Aperfeiçoamento de Pessoal de Nível Superior - Brasil (CAPES) - Finance Code 001, by the Conselho Nacional de Desenvolvimento Científico e Tecnológico (CNPq), and by the Fundação de Amparo à Pesquisa do Estado do Rio de Janeiro (FAPERJ). I thank the funding agencies and also the physics department at PUC-Rio and INCT-SC.

To everyone who directly or indirectly took part in my trajectory, my sincere appreciation.

Abstract

Dornelas, Vivian; Anteneodo, Celia (Advisor). **Spatial organization of single-species populations**. Rio de Janeiro, 2020. 93p. Tese de Doutorado – Departamento de Física, Pontifícia Universidade Católica do Rio de Janeiro.

It is common to observe in nature the emergence of collective behavior in biological populations, such as pattern formation. In this work, we are interested in characterizing the distribution of a single-species population (such as some bacteria or vegetation), based on mathematical models that describe the spatio-temporal evolution, and governed by elementary processes, such as: dispersion, growth, and nonlocal competition by resources. First, using a generalization of the FKPP equation, we analyze numerically and analytically the impact of density-dependent regulatory mechanisms, both on diffusion and growth. Such mechanisms represent processes of internal feedback, which shape the system's response to population overcrowding or rarefaction. We show that, depending on the type of the response in action, some individuals can organize themselves in disconnected sub-populations (fragmentation), even in the absence of external restrictions, that is in a homogeneous landscape. We discuss the crucial role that density-dependence has in the form of patterns, particularly in fragmentation, which can have important consequences for contact processes, such as the spread of epidemics. After understanding this phenomenon in a homogeneous environment, we study the role that a heterogeneous environment has in the spatial organization of a population, which was presented as a growth rate that varies with position. We investigate the structures that emerge near the border from one environment to the other. We found that, depending on the shape of nonlocal interaction and other model parameters, three different profiles can emerge from the interface: (i) sustained oscillations (or spatial patterns, without amplitude decay); (ii) attenuated oscillations (with amplitude decreasing from the interface); (iii) exponential decay (without oscillations) to a homogeneous profile. We related the wavelength and the rate of decay of oscillations with the parameters of the interaction (characteristic length and form of decay with distance). We discussed how the heterogeneities of the environment allow access to information (hidden in the homogeneous case) about the biological phenomena of the system, such as those that mediate competitive interactions.

Keywords

Population dynamics; Self-organization; Pattern formation; Nonlinear diffusion.

Resumo

Dornelas, Vivian; Anteneodo, Celia. **Organização espacial de populações de espécie única**. Rio de Janeiro, 2020. 93p. Tese de Doutorado – Departamento de Física, Pontifícia Universidade Católica do Rio de Janeiro.

É comum observar na natureza a emergência de comportamentos coletivos em populações biológicas, como formação de padrão. Neste trabalho, estamos interessados em caracterizar a distribuição de uma população de espécie única (como alguns tipos de bactérias ou de vegetação), a partir de modelos matemáticos que descrevem a evolução espaço-temporal, governados por processos elementares como: dispersão, crescimento e competição não-local por recursos. Primeiramente, utilizando uma generalização da equação de FKPP, analisamos numérica e analiticamente, o impacto de mecanismos de regulação dependentes da densidade, tanto na difusão quanto no crescimento. Tais mecanismos representam processos internos de retroalimentação, que modelam a resposta do sistema à superlotação ou rarefação da população. Mostramos que, dependendo do tipo de resposta em ação, os indivíduos podem se auto-organizar em subpopulações desconectadas (fragmentação), mesmo na ausência de restrições externas, ou seja, em uma paisagem homogênea. Discutimos o papel crucial que a dependência com a densidade tem na forma dos padrões, particularmente na fragmentação, o que pode trazer consequências importantes para processos de contato como disseminação de epidemias. Tendo compreendido esse fenômeno em um meio homogêneo, estudamos o papel que um ambiente heterogêneo tem na organização espacial de uma população, que representamos através de uma taxa de crescimento que varia com a posição. Investigamos as estruturas que emergem próximo a fronteira de um meio para o outro. Descobrimos que, dependendo da forma de interação não-local e de outros parâmetros do modelo, três perfis diferentes podem emergir a partir da interface: (i) oscilações não-atenuadas (ou padrões espaciais, sem decaimento da amplitude); (ii) oscilações atenuadas (com amplitude decaindo a partir da interface); (iii) decaimento exponencial (sem oscilações) a um perfil homogêneo. Relacionamos o comprimento de onda e a taxa de decaimento das oscilações com os parâmetros das interações (comprimento característico e forma de decaimento com a distância). Discutimos como as heterogeneidades do ambiente permitem acessar informações (ocultas no caso homogêneo) sobre os fenômenos biológicos do sistema, tais como os que mediam interações competitivas.

Palavras-chave

Dinâmica de populações; Auto-organização; Formação de padrões; Difusão não linear.

Table of contents

List of figures

Figure C.2 **Poles of the mode growth rate $\lambda(k)$ in the complex plane for γ_α and $D = 10^{-3}$.** The influence function used was γ_α, with $\ell = 2$ and α indicated in the figure. The blue dots are for N=100, and the red crosses for N=150. 93

List of tables

1
Introduction

The study of pattern formation has many applications and is of great interest to many areas of research, such as: Physics, Biology, Mathematics, among others. Patterns – which can be spatial or temporal – emerge when there is a correlation between the elements within a system [1, 5, 6, 7, 8, 9, 10, 11, 12].

We are interested in: understanding how they form in the biological population of single species that spatially self-organize; and, in particular, determining the critical conditions for the onset of patterns.

Studied populations range from simple organisms, such as cells and bacteria, to systems in ecological scale, such as vegetation.

We will see two different ways to observe pattern formation:

- The first one is when self-organized structures emerge from internal interactions. We will approach it in a homogeneous landscape, through dynamics with density-dependent feedbacks [7, 13, 14, 15, 16], in order to understand the shape of the stationary profiles of a population and, particularly, population fragmentation.
- Second, we will see that the external factor - such as the heterogeneous landscape [17, 18, 19, 20, 21, 22, 23, 24, 25, 26, 27], can impose patterns on a population, depending on the internal interactions of the system. In this case, different kinds of stationary profiles can emerge: sustained oscillations (or spatial patterns, without amplitude decay); decaying oscillations (with decreasing amplitude from the interface), or exponential decay towards a flat profile.

To study this emergence of patterns, we use a standard single-species model (a generalized Fisher-Kolmogorov-Petrovskii-Piskunov equation [28, 29, 30]) that includes nonlocal intraspecific competition for resources, beyond reproduction and dispersal terms.

We propose general forms of the influence function that sets how the interaction between individuals depends on the distance. This function effectively includes long-range interactions that can emerge due to shared resources and from the underlying dynamics of the environment. Following computational and theoretical approaches, we will investigate the spatial structures

that emerge in both the situations described above. We provide theoretical predictions based on mode linear stability analysis, in accordance with the numerical results.

This document is structured as it follows:

- In Chapter 2, we provide introductory information with general considerations. We present the adopted model, explaining its components, and we show how to analyze this model numerically and analytically;
- In Chapter 3, we study, in a homogeneous landscape, how density-dependent feedbacks influence the shape of the patterns, and the factors that favor population fragmentation;
- In Chapter 4, we study the effect that the heterogeneous landscape has on the spatial distribution of a population, more precisely between viable and non-viable regions.

  We provide an analogy between the solution of the density distribution in the steady-state, and the forced linear oscillator, which helps us to understand the structures that emerge from the interface. Moreover, we discuss how the information about the interaction kernel can be extracted from observable oscillations. Additionally, outcomes for 2D landscapes are shown to illustrate that the main phenomenology investigated is not restricted to 1D;
- In Chapter 5, we present the final considerations, summarizing what has been presented;
- In Chapter 6, we present a preliminary study about the role of limited heterogeneous habitats on population dynamics, considering a space-dependent diffusion.

2
Population dynamics

We present, in this chapter, previous concepts and some definitions that will be necessary for the understanding of the research presented in this work. The model adopted is described, as well as the numerical and analytical methods used to solve it. We start with a phenomenological description of pattern formation.

2.1
Pattern formation

Many systems observed in nature are spatially organized with a periodic – or almost periodic – distribution, without centralized control. There are many examples where the patterns are generated either by a heterogeneous landscape or by the intrinsic behaviors of the population taken into consideration. Some organisms can be responsible for shaping a landscape with patterns, such as: the termites, which create mounds with associated vegetation thickets, in many places of the world (Fig. 2.1 taken from Google [1]) ; the male *Tilapia mossambica*, which creates hexagonal territory; or bees, which always create the alveolar in a hexagonal shape because it uses less wax and makes the most of the hive space.

Patterns can also be found in collective behavior, such as: flocks of birds (murmuration) [31] and clusters of fish [32], which form structures in space-time; and in traffic and pedestrian dynamics [33].

Moreover, controlled experiments with bacterial colonies growing on a homogeneous substrate [3, 34, 35] also show different types of patterns. They indicate that the emergence of self-organization might be intrinsic to the population. Although it is a very broad topic, we will restrict our study to a biological population that is composed of simple organisms of a single species. The population follows the Markovian dynamics, without memory. Populations of some bacteria and plants can be labeled in this category. We will explore patterns that emerge from intraspecific interactions and/or from a heterogeneous landscape. Particularly, we investigate the pattern formation that emerges from the generalized Fisher-Kolmogorov-Petrovskii-Piskunov (FKPP) equation, which we present in the next section.

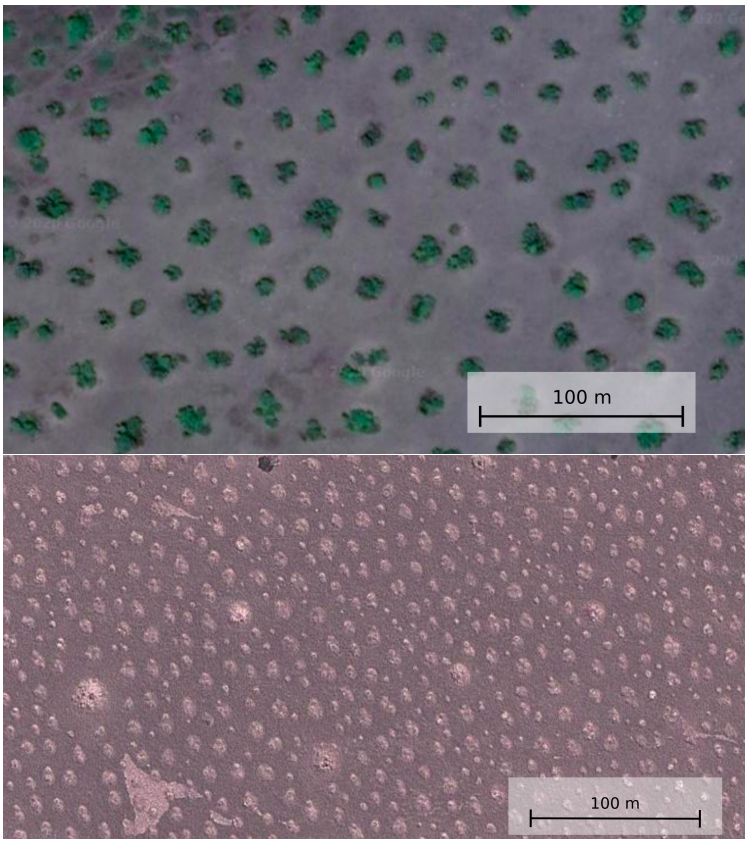

Figure 2.1: **Examples of patterns created by animals.** In the upper panel, we can see a satellite picture of termite mounds with associated vegetation in Pantanal, Brazil (11°56'34.8"S 50°46'37.2"W). In the lower panel, multiscale mound patterning, potentially created by two different social-insect species [1], in the Bangweulu floodplain Zambia – an ecosystem described by the explorer David Livingstone as "A World of Water and Anthills" (11°06'40.1"S 30°10'51.5"E). Imagery: Google, DigitalGlobe.

2.2 Single-species model

There are many mathematical models in the literature for the spatio-temporal dynamics of a single-species population that describe: diffusion, growth, competition and interaction between species [36]. The classic simplest model is the Fisher-Kolmogorov-Petrovskii-Piskunov (FKPP) equation [28, 29], where the population density $\rho(\vec{x}, t)$ at position $\vec{x}$ and time t is given by

$$\partial_t \rho(\vec{x}, t) = D\nabla^2 \rho(\vec{x}, t) + a\rho(\vec{x}, t) - b\rho^2(\vec{x}, t), \tag{2-1}$$

where D is the diffusion coefficient, a is the (clonal) reproduction rate, and b is the strength of (intraspecific) competition that bounds population growth. Those are all positive constants. While $a > 0$ guarantees a positive growth rate (a necessary condition for the survival of the species), $b > 0$ guarantees

that the interaction term is negative (intraspecific competitive interaction), a condition for the logistical effect to be obeyed.

In Eq. (2-1) competition is local, in the sense that it occurs at scales much shorter than those associated to the diffusion process. However, competition effects might also extend to larger scales, making the interaction essentially nonlocal. For instance, nonlocal cooperation and competition can be present in vegetation mediated by roots [37, 38, 39]. Also, nonlocality can emerge due to the spread of substances released or consumed by the individuals [8, 11, 16, 37, 40, 41].

Then, assuming that interaction can act at a distance according to a kernel (also called influence function) γ, and, that diffusion and growth are not constant, in one dimension, Eq. (2-1) is extended as

$$\partial_t \rho(x,t) = \partial_x(D(\rho)\partial_x \rho) + f(\rho)\rho - b\rho[\gamma \star \rho](x,t)\,, \tag{2-2}$$

where $[\gamma \star \rho](x,t) \equiv \int_{-\infty}^{\infty} \gamma(x-x')\rho(x',dt)dx'$, and the kernel is normalized, i.e., $\int_{-\infty}^{\infty} \gamma(x)dx = 1$. Furthermore, we assumed $\gamma \geq 0$ to describe competitive interactions between individuals. That generalization takes density-dependent feedback into account.

The FKPP equation is intended to describe the temporal evolution of population distributions, but it may also describe gene distribution or niche occupation [28]. We describe below the meaning and the contribution of each term to the dynamics.

Diffusion

Density-dependent mobility can arise due to the environments' structure [42, 43], such as in porous-media. Also, it can originate from complex biological and social reactions in response to overcrowding or rarefaction of the population density [23, 44]. For instance, in populations of insects, such as ants, it has been observed that the diffusion coefficient can be facilitated or hindered by population concentration [36]. In this situation and in other examples [14, 36, 45, 46, 47], a power-law form for the diffusion coefficient can be used as phenomenological description. Therefore, we will consider the diffusion coefficient $D(\rho) = \tilde{D}\rho^{\nu-1}$ where ν is a positive constant. Then, the generalized diffusion equation is given by

$$\partial_t \rho = D\partial_{xx}\rho^{\nu}. \tag{2-3}$$

It generates two different anomalous diffusive behaviors. The solutions for this equation are depicted in Fig. 2.2 for $\nu < 1$ (left) and $\nu > 1$ (right).

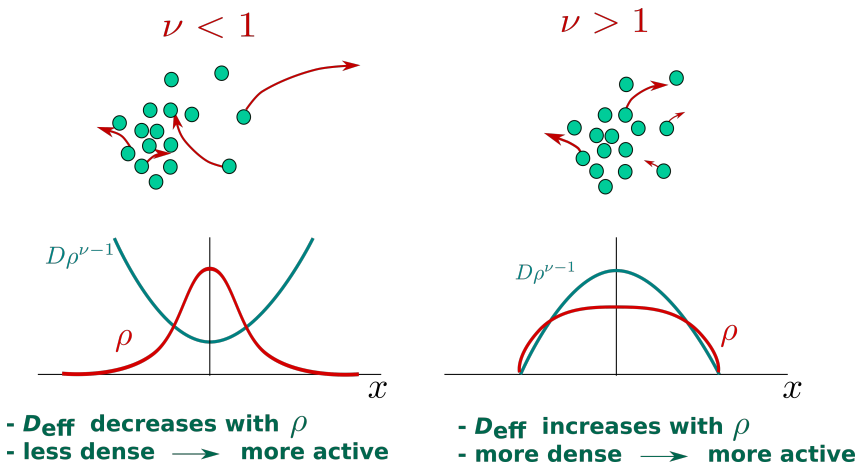

Figure 2.2: **Schematic representation of nonlinear anomalous diffusion.** On the left, we have a superdiffusive system, and on the right, a subdiffusive one.

When $\nu > 1$, the dynamics is subdiffusive. That is, the variance of the spatial distribution increases sub-linearly with time. This anomaly occurs because mobility increases with density, and so, more populated regions become more active. In this case, the density profile tends to follow platykurtic distributions (sub-Gaussian). And when $\nu < 1$, the dynamics are superdiffusive (the variance increases super-linearly with time). In that case, mobility decreases with density, and less dense region are more active. The density profile tends to follow leptokurtic distributions (super-Gaussian) [48].

Growth

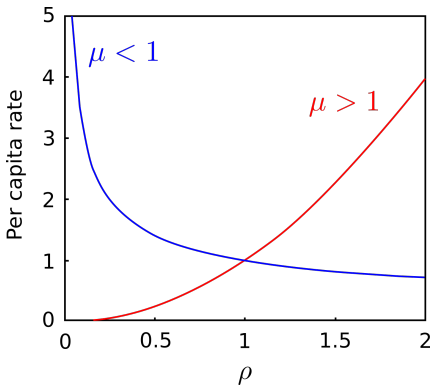

Figure 2.3: **Schematic representation of the per capita growth** rate as a function of the density ρ, for super-exponential growth $\mu > 1$ and sub-exponential growth $\mu < 1$.

Population growth can also be governed by density-dependent factors.

For instance, related to the Allee effect, the per capita reproduction rate vanishes at the low concentration limit. But there are also cases where reproduction is favored when the concentration is low, due to the absence of overpopulation disadvantages.

In order to consider different behaviors, we will also consider the power law $f(\rho) = a\rho^{\mu-1}$, where the solution for $\dot{\rho} = \rho^{\mu}$ is given by

$$\rho(t) = \rho_0 \left[1 + \frac{1-\mu}{\rho_0^{1-\mu}} at\right]^{\frac{1}{1-\mu}}. \tag{2-4}$$

If $\mu \to 1$, the growth in time is exponential, while $\mu = 0$ represents linear growth. In the Fig. 2.3 the per capita rate of the growth is depicted as a function of ρ, for $\mu > 1$ and $\mu < 1$; and in the Fig. 2.4, the temporal evolution of the density is represented for different growth exponent.

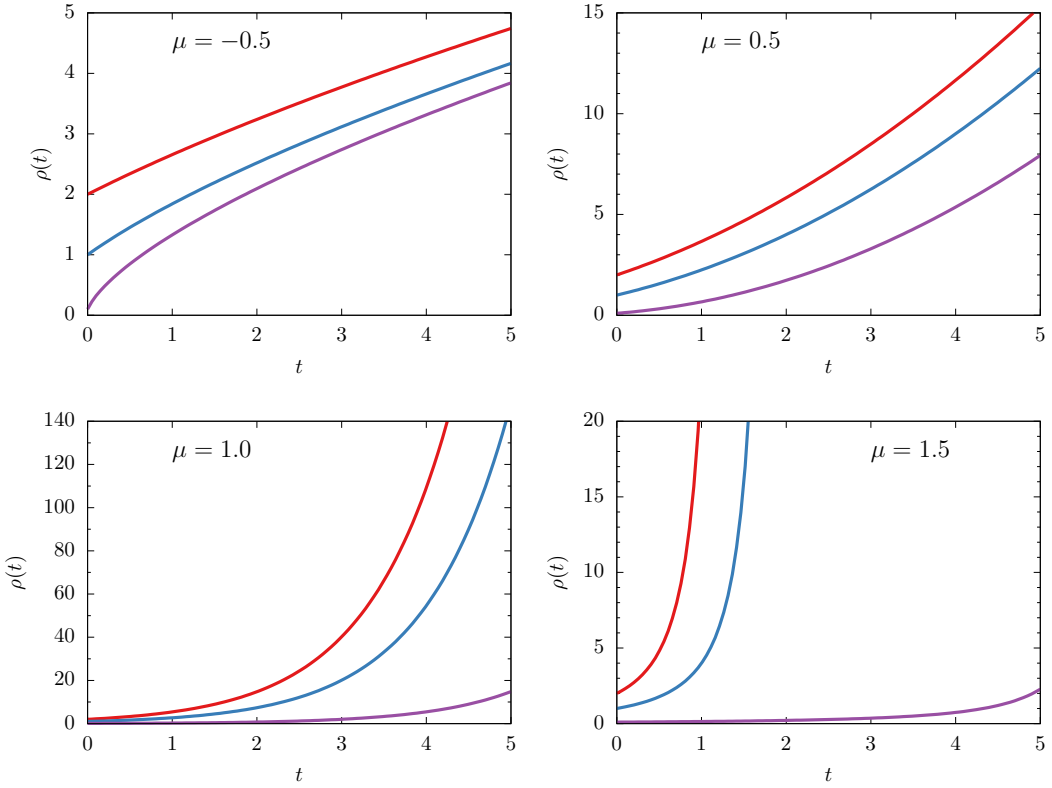

Figure 2.4: **Examples of density variation with time, for different values of μ and different initial conditions.** Red curve: $\rho_0 = 2$; blue curve: $\rho_0 = 1$; purple curve: $\rho_0 = 0.1$.

When $\mu < 1$, the population grows more in less occupied regions, filling the emptiest spaces and decreasing the variation in density. When $\mu > 1$, we have the opposite effect, favoring the growth in more populated areas.

Competition

We consider that an individual has its resources limited by the number of neighbors in the region of influence. For instance, plants absorb nitrogen from the soil through the roots, reducing nutrients and, occasionally, killing nearby plants at spatial scales much larger than the size of the individual. Because of such mechanisms, it is necessary to assume a nonlocal competition, which can be mediated by an influence function or an effective kernel, which determines how that neighborhood affects the individual. Under some conditions, such spatial coupling may promote spatial instability, a key ingredient for pattern formation.

Differently from the original FKPP Eq. (2-1), the nonlocal FKPP equation – given by Eq. (2-2) – can exhibit self-organized structures depending on the particular properties of the kernel and the values of the diffusion and reproduction rates [49, 50, 51, 52].

With these generalizations, Eq. (2-2) becomes

$$\partial_t \rho(x,t) = D\partial_{xx}(\rho^\nu) + a\rho^\mu - b\rho[\gamma \star \rho](x,t)\,. \tag{2-5}$$

We will study the effect of some types of influence functions, which we will define throughout the work.

2.3 Linear stability analysis

By studying pattern formation, through the generalized FKPP equation, we find nonlinear effects that emerge from the interaction between the nonlinear feedbacks in diffusion and growth processes, and also on nonlocality.

With analytical methods, we will be able to understand the relationships between interactions and the shape of patterns. As the equation from which we will start is nonlinear, our analytical results are based on the linearization of the equation of evolution around a homogeneous state. This leads us to a linear stability analysis that will allow us to identify the emergence of structures with a characteristic spatial scale.

However, as the information obtained analytically is limited due to the nonlinear character of the system, we also present numerical methods (which will be described in Sec. 2.4) that provide information about the entire evolution.

The steps presented here for the linear stability analysis, are the same followed in chapters 3 and 4. Then, we start by assuming a small perturbation

around the nontrivial homogeneous solution of the main equation, $\rho_0 = (b/a)^{1/(\mu-2)}$, i.e.,

$$\rho(x,t) = \rho_0 + \varepsilon(x,t). \tag{2-6}$$

The first term of Eq. (2-5), after expanding and neglecting second-order terms, is

$$\begin{aligned} \rho^\nu &= \rho_0^\nu + \nu\rho_0^{\nu-1}\varepsilon, \\ \partial_{xx}\rho^\nu &= \nu\rho_0^{\nu-1}\partial_{xx}\varepsilon. \end{aligned}$$

Replacing the expansions in Eq. (2-5) and considering that the kernel is normalized ($\int_{-\infty}^{\infty}\gamma(x)dx = 1$), we have

$$\partial_t\varepsilon = D\rho_0^{\nu-1}\partial_{xx}\varepsilon + b(\mu\rho_0 - 1)\varepsilon - b\rho_0\int_{-\infty}^{\infty}\gamma(x-y)\varepsilon(y)dy, \tag{2-7}$$

which in Fourier space becomes [1]

$$\partial_t\tilde{\varepsilon}(k,t) = \lambda(k)\tilde{\varepsilon}(k,t)\,, \tag{2-8}$$

where the rate $\lambda(k)$ is given by the mode growth rate

$$\lambda(k) = -k^2 D\rho_0^{\nu-1} - b\rho_0\tilde{\gamma} + b(\mu\rho_0 - 1). \tag{2-9}$$

It is an important quantity that will appear all throughout the work. In terms of it, $\tilde{\varepsilon}(k,t) = \tilde{\varepsilon}(k,0)\mathrm{e}^{\lambda(k)t}$. Thus, if $\lambda < 0$, any initial perturbation will fade out, such that in the long-time limit, the population distribution $\rho(x)$ will be flat (homogeneous distribution). On the contrary, if there are unstable modes, with $\lambda(k) > 0$, stationary sustained oscillations will be produced with a characteristic mode $k^\star$ (the maximum of λ), which is, initially, the fastest growing one [53].

Since the equation is very nonlinear and nonlocal (integro-differential), limitations arise even for very particular cases. For instance, for the linear case, $\nu = \mu = 1$ (which recovers the nonlocal competitive FKPP, many times investigated in the literature), no solution for the stationary patterns is known. Only for the case without the diffusive term, a nonlinear procedure [52, 54] gives the stationary solution. Near the transition to patterns (small amplitude), the solution for sine-like patterns can be obtained by perturbative approaches [55].

[1] The Fourier transform of a function $f(x)$ is defined as $\tilde{f}(k) = \int_{-\infty}^{\infty} f(x)e^{-ikx}dx$.

2.4 Numerical method

Numerical integration of Eq. (2-5), with periodic boundary conditions, was performed starting from a homogeneous state, plus a random perturbation, uniformly distributed with a very small amplitude, following a standard forward-time-centered-space scheme [56] (depicted in Fig. 2.5).

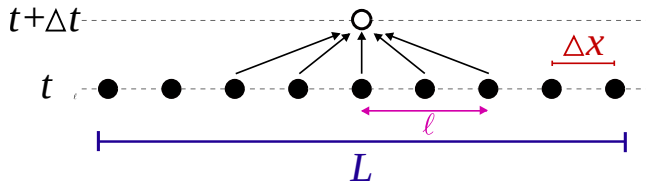

Figure 2.5: **Schematic representation of the FTCS method.** At each time increment Δt, for an x position, the densities of the population within an ℓ neighborhood are taken into account, which influence according to an interaction kernel γ. L is the system size.

The used algorithm is fourth order Runge-Kutta in time and second order in space (method adopted in all the numerical simulations). We let the dynamics evolve until the stationary regime has been reached. In simulations, we used different values of space and time increments (dx and dt), according to the parameters and model studied. The choice was made according to a convergence analysis that will be described later.

Following this method, we represent in Fig. 2.6 the temporal evolution of density as a function of position for a specific case of Eq. (2-5) where $\lambda(k^\star) > 0$. The parameters used are described in the figure.

In order to provide a concrete response regarding the accuracy of our numerical scheme, we estimate the error in our simulations. In the Fig. 2.7, we show the temporal evolution of the maximal and minimal values of ρ as a function of time for different discretization steps dt. In the Fig. 2.8, the error associated to $\rho(t = 200)$ is shown as function of dt.

The error of a given value of ρ was estimated as $\frac{|\rho-\rho_1|}{\rho_1} \times 100$, where ρ_1 is the limit value for $dt \to 0$, that is $\rho(dt = 10^{-6})$ in the figure.

Notice that the error decays with dt, and for sufficiently small dt it falls within a desired accuracy. For instance, 1%, when $dt = 10^{-4}$, for the minimal value of ρ ($\rho_{min} \simeq 4 \times 10^{180}$ in the case of the figure) while the error is still smaller for the maximal value of ρ.

In Fig. 2.9 we can see the pattern being created as the time evolves. In this example, the minimum density stabilizes at a constant value. Similar cases will be studied in Chapter 3.

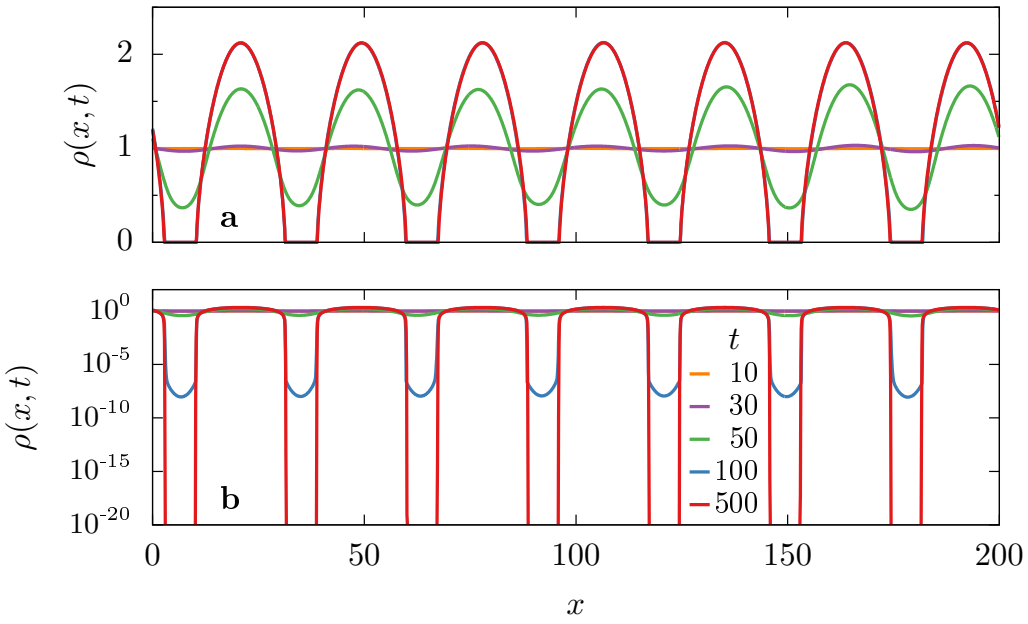

Figure 2.6: **Temporal evolution of population density.** Numerical simulation of Eq. (2-5), with periodic boundary conditions, was performed using the homogeneous influence function in an $\ell = 20$ neighborhood, for a population of $L = 200$ size. The other parameters are: $D = a = b = 1$, $\mu = 1.6$, $\nu = 4.0$, and the increments $dx = 0.08$ and $dt = 10^{-5}$.

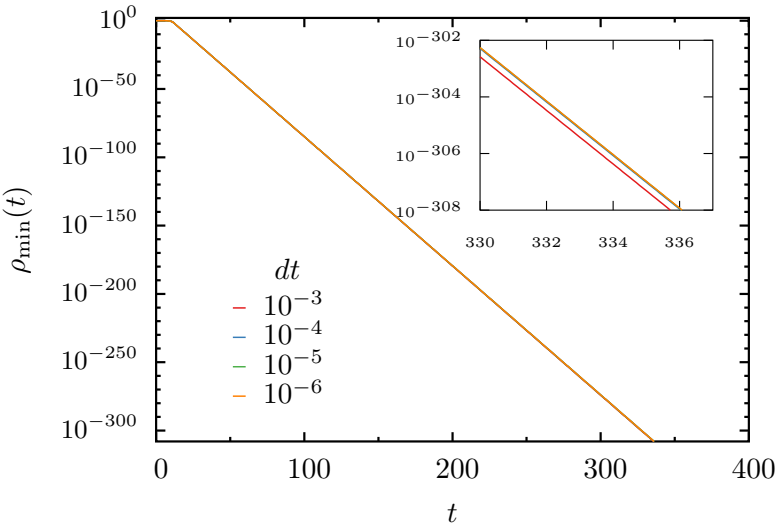

Figure 2.7: **The minimal value of $\rho(x)$ as a function of t**, corresponding to the case $\nu = 4.0$ and $\mu = 1.6$, presented in Fig. 2.6, for different values of the integration step dt indicated on the figure. The inset shows a zoom near 10^{-308}. All simulation runs started from the same initial conditions.

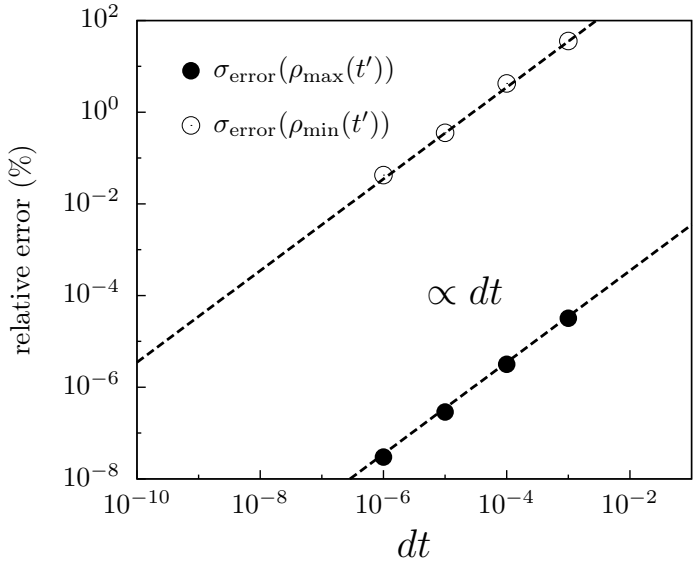

Figure 2.8: **The percentual error of the extreme values of ρ as a function of dt.** The parameters are the same of Fig. 2.7, and $t = 200$. Notice that, even for the minimal density ($\rho_{min} \simeq 4 \times 10^{180}$), errors are smaller than 1% for sufficiently low dt and decay with decreasing dt.

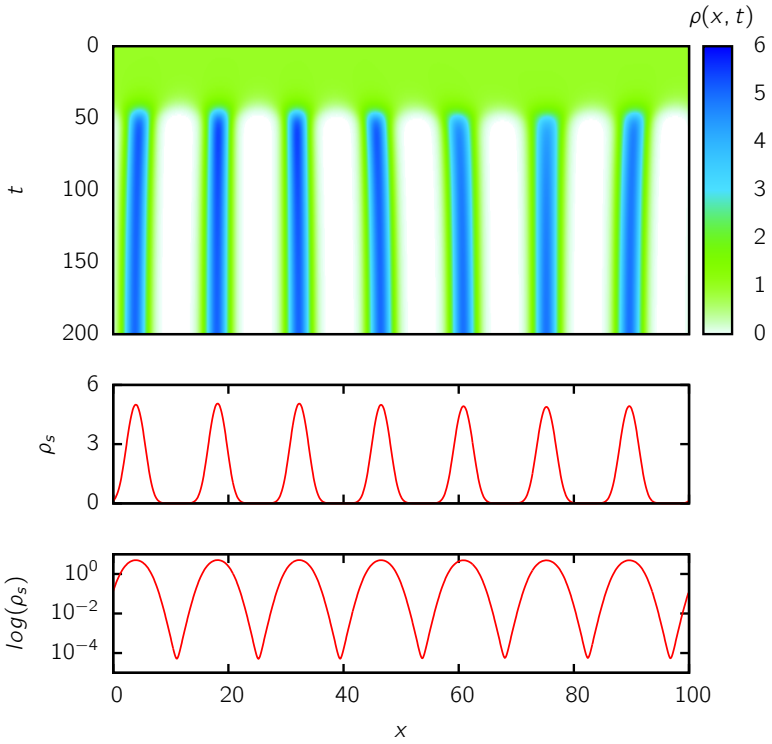

Figure 2.9: **Temporal evolution of population density and stationary pattern**, using the homogeneous influence function with $\ell = 10$. The other parameters are $D = 0.1$, $a = b = 1$, and $\nu = \mu = 1$.

3
Self-induced population fragmentation

Population fragmentation is characterized by critical changes in the spatial distribution of individuals, creating isolated sub-groups of a given initial population. This phenomenon has important consequences for secondary processes such as epidemic spreading, species invasion [6] or also speciation [57]. Fragmentation is often attributed to landscape heterogeneity, which embraces the spatial distribution of geographical and environmental features [58]. If natural barriers are sustained for long periods of time, fragmentation can be induced [57].

This scenario has been vastly studied in the context of metapopulation theory, which takes into account the ecological landscape heterogeneity [20]. The degree of fragmentation of the landscape, which is imposed to the population, is widely known for playing an important role and determining the species richness and ecosystem stability, against external perturbations [20, 59, 60]. But regardless of environment heterogeneity, arrangements of individuals in space can also emerge solely from their interactions, bringing critical consequences to the evolutionary dynamics and social behavior of living organisms [61, 62, 63, 64, 65].

Precisely, we explore in this chapter the conditions under which population dynamics can self-induce fragmentation in the absence of external barriers. The results of this research were published in the Ref. [66].

3.1
Model

Following the model given in the Sec. 2.2, we investigate the class of dynamics where diffusion and growth coefficients have power-law density dependencies. Before proceeding, we adimensionalize Eq. (2-5), by defining the scaled variables

$$\begin{aligned} \rho' &= \rho/\rho_0, \\ t' &= a\rho_0^{\mu-1}t, \\ x' &= \sqrt{a\rho_0^{\mu-\nu}/D}\; x, \end{aligned} \tag{3-1}$$

where $\rho_0 = (b/a)^{1/(\mu-2)}$ is the uniform stationary solution, that becomes $\rho_0' = 1$. Then, substituting the scaling relations (3-1) into Eq. (2-5) and eliminating the prime superindexes, Eq. (2-5) becomes

$$\partial_t \rho(x,t) = \partial_x(\rho^{\nu-1}\partial_x\rho) + \rho^\mu - \rho\int_{-\infty}^{\infty}\gamma(x-y)\rho(y)dy\,. \tag{3-2}$$

In this way, the exponents μ and ν are the only remaining parameters, once fixed kernel γ. For logistic effect (referring to limited resources), we must have $\mu < 2$, to ensure that the population size remains bounded. The influence kernel that we consider in this chapter is the homogeneous influence function, also known as top-hat kernel, which is constant inside a certain region of width 2ℓ,

$$\gamma_h(x) = \frac{1}{2\ell}\Theta(\ell - |x|)\,, \tag{3-3}$$

being non-null only if $|x| < \ell$, and which Fourier transform is $\tilde{\gamma}_h(k) = \sin(k\ell)/(k\ell)$.

Typical profiles that emerge in our numerical simulations are presented in Fig. 3.1, where we can also observe the mode growth rate that assumes positive values.

3.2 Linear stability analysis

We will follow the standard procedure, explained in Sec. 2.3, where we assume a small perturbation around the nontrivial homogeneous steady state, i.e., $\rho(x,t) = 1 + \varepsilon(x,t)$. The linearization of Eq. (3-2) provides the mode growth rate

$$\lambda(k) = -k^2 - \gamma_h(k) + \mu - 1\,. \tag{3-4}$$

The first term on the right side of Eq. (3-4) is associated with diffusion and is always negative, tending to stabilize the homogeneous state. The term $\tilde{\gamma}_h(k)$, associated with nonlocality, takes positive and negative values and therefore, can contribute to destabilizing the homogeneous state and can originate pattern formation. Additionally, the nonlinearity in the growth rate ($\mu \neq 1$) shifts the mode growth rate according to the linear case ($\mu = 1$), contributing to the destabilization when $\mu > 1$, and to stabilization when $\mu < 1$. Notice that the diffusion exponent ν does not appear explicitly in the mode growth rate due to the normalization used.

We can find the dominant mode $k^\star$, which is the maximum of $\lambda(k)$, by considering the derivative of Eq. (3-4) equal to zero. Also, we can numerically calculate its approximate value by $k^\star\ell \simeq 3\pi/2$. This value gives us information about the wavelength.

To obtain patterns, it is necessary that $\lambda(k) > 0$; that is, μ is greater

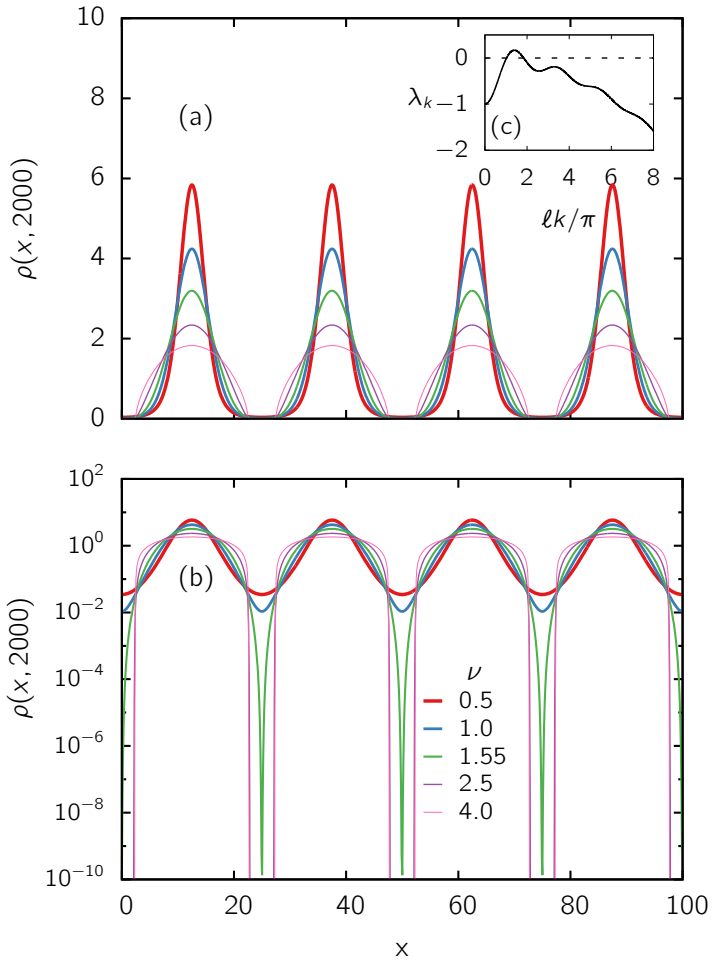

Figure 3.1: **Patterns:** a) We present numerical results of Eq. (3-2) for the density $\rho(x)$ at $t = 2000$, using $L = 100$, $\ell = 20$, $\mu = 1.0$, and different values of diffusion exponent ν indicated in the legend. b) The same on the log-scale. c) The mode growth rate, given by Eq. (3-4), which is independent of ν.

than a critical value

$$\mu_p \equiv (k^\star)^2 - \frac{1}{k^\star \ell} + 1, \tag{3-5}$$

that constitutes the frontier for the onset of patterns. Moreover, when patterns appear, the number m of peaks can be estimated by

$$m = \frac{k^\star L}{2\pi} \simeq 0.715 \frac{L}{\ell}, \tag{3-6}$$

where L is the system size.

Notice that nonlinearities are also contained in the spatial and time scales, according to Eqs. (3-1); and for that reason, they influence pattern wavelength and growth rate. Therefore, although ν does not appear explicitly in Eq. (3-4), it has an indirect influence.

The theoretical linear approximation is not valid when approaching the

limit of consistency of the model, i.e., when $\mu \approx 2$. If $\mu > 2$, the population grows indefinitely. In order to analyze what happens with the number of peaks when we approach this limit, we represent in Fig. 3.2 the shape of patterns for $L = 200$, $\ell = 20$, $\nu = 4.0$ and different values of μ. In this case, we started with 7 peaks ($m = 7.5$) and the value decreases, while increasing μ.

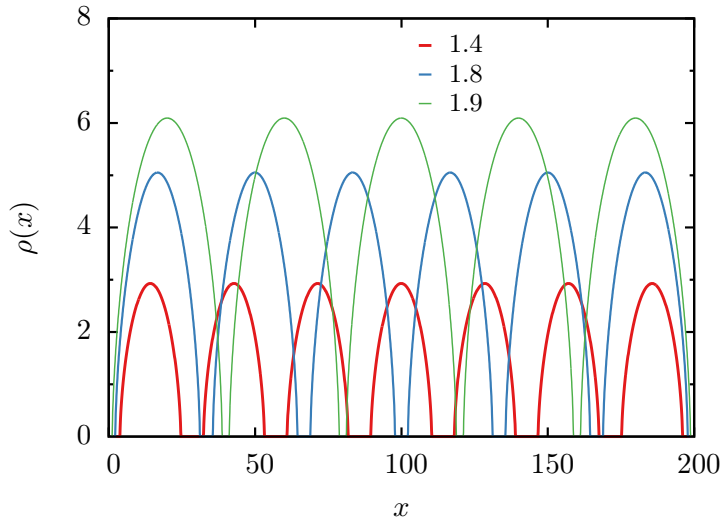

Figure 3.2: **Number of peaks and nonlinearity.** For $L = 200$, $\ell = 20$, $\nu = 4.0$, and different values of μ – indicated on the legend, numerical simulations of Eq. (3-2) show that increasing the growth exponent μ decreases the number of peaks of the stationary patterns.

We can interpret the change of the number of peaks in terms of the interactions between the individuals. As we increase the exponent μ, the population's growth becomes greater in more populated regions, producing a large concentration in the peak. If the diffusion exponent ν is greater or equal to one, we have two phenomena occurring: the population is growing and spreading further. In consequence, we observe fewer peaks when increasing the value of μ.

3.3 Numerical results

In all the numerical simulations of this chapter – exceptions aside, we set the system size $L = 100$ and the competition interaction range $\ell = 20$. As a consequence of this choice, Eq. (3-6) predicts that, when there are patterns (i.e., when $\mu > \mu_p \simeq 0.84$), the estimated number m of peaks is $m = 3.75$. Therefore, we are more likely to observe 4 peaks. But, we chose realizations with the same number of peaks for comparisons.

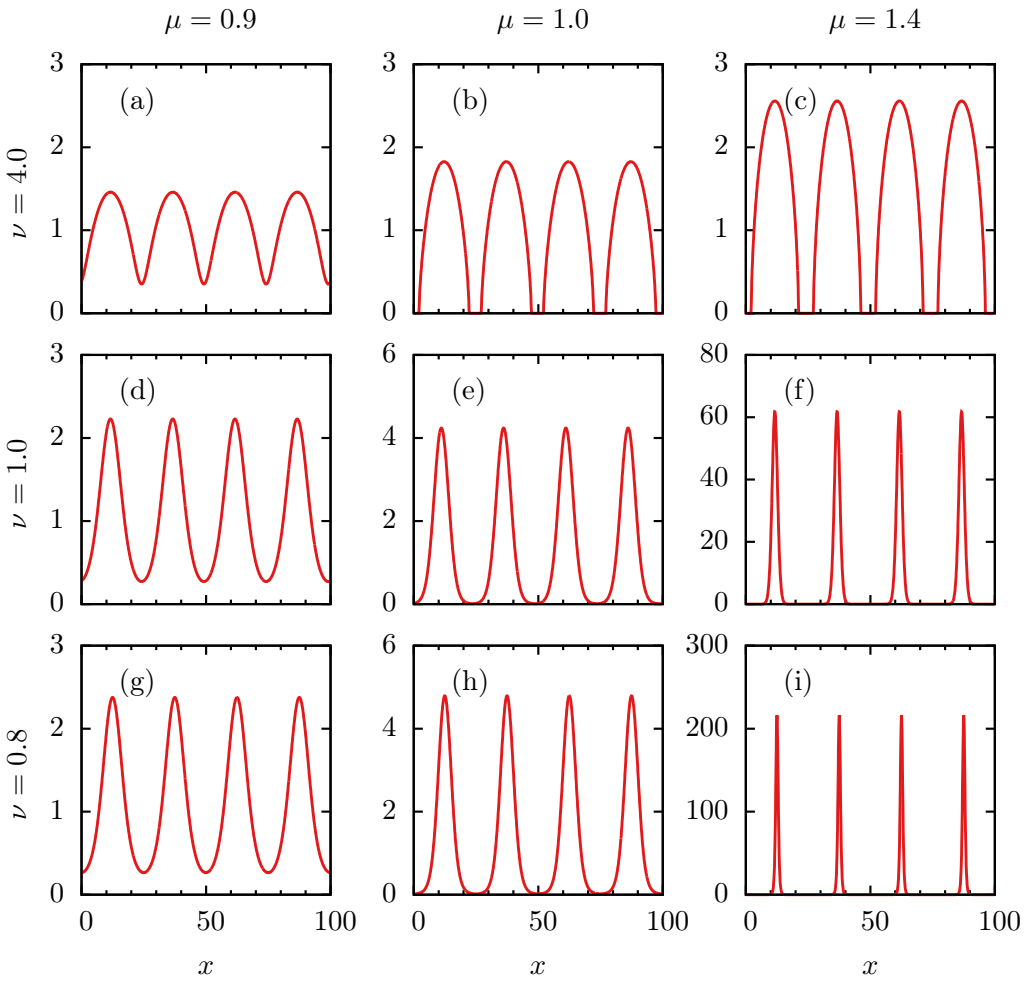

Figure 3.3: **Stationary profiles.** We present the stationary density $\rho(x)$ for different values of ν: 0.8 (superdiffusion), 1.0 (normal diffusion) and 4.0 (subdiffusion), and different values of the growth exponent μ: 0.9, 1.0 and 1.4.

The shape of the patterns in function of ν and μ are presented in Fig. 3.3, on the region where $\lambda(k) > 0$. In the standard case $\mu = \nu = 1$, each peak has a Gaussian-like shape. But when feedbacks are taken into account, mobility and reproduction rates respond to the degree of agglomeration of individuals. Then, when $\nu > 1$, the peaks tend to be more platykurtic (sub-Gaussian distribution); that is, they have thinner tails, since the diffusion rate vanishes at low densities. Similarly, when $\nu < 1$ the peaks tend to be more leptokurtic (super-Gaussian) – fatter tails, as the diffusion rate diverges at low densities.

Concerning the exponent μ, it is evident that the patterns that emerge when $\mu < 1$ have a minimum value, which is noticeably non-zero, in contrast to the cases $\mu \geq 1$. These traits can be associated with the type of density-dependent feedback (governed by μ): when $\mu < 1$, population growth is enhanced in low-density regions, raising the population level in the valley

between clusters; while for $\mu > 1$, the opposite effect occurs.

The combination of diffusion and growth nonlinearities generates the diverse profiles shown in Fig. 3.3. In Sec. 3.4, we present mathematical functions that described these patterns very well. Next, we will discuss the emergence of these profiles, focusing on the characterization and definition of fragmented states (Figs. 3.3b-c).

To identify the fragmentation process, we follow the temporal evolution of the smallest value of the concentration of individuals, $\rho_{\min}(t)$. Representative cases are shown in Fig. 3.4a, where, in addition to the minimal value, the largest value $\rho_{\max}(t)$ is also inserted in the graphic.

We note that, for small enough values of μ, $\rho_{\min}(t)$ stabilizes at a finite level. In contrast, for μ greater than a critical value ($\mu_c \simeq 1$ for $\nu = 4.0$, such as the case of Fig. 3.4a), $\rho_{\min}(t) \sim \exp(-t/\tau)$, decreasing exponentially with time to the computational limit ($\varrho \sim 10^{-308}$). Note, in Fig. 3.4b, that the critical value of μ is function of ν. For $\mu < \mu_p$, the stationary value of $\rho_{\min} = \rho_0 = 1$ and there are no patterns, as anticipated.

The characteristic time τ is represented in Fig. 3.5 as a function of the exponents, including the cases shown in Fig. 3.4a.

When ν and μ obey certain conditions, the numerical outcomes suggest the emergence of disconnected clusters, separated by depopulated regions. To better characterize the fragmented patterns and the conditions for their emergence, we consider, in addition to the stationary values ($\rho_{\max}$ and $\rho_{\min}$), the width σ of each cluster at half height and the length Δ of the region where ρ attains ϱ, which we interpret as null density [1]. The results are shown in Fig. 3.6, varying diffusion exponent ν while keeping the growth exponent μ constant. For $\mu = 0.9$ (Fig. 3.6a), the shape of the patterns is almost insensitive to ν. Importantly, we do not detect a region where the density vanishes (for this reason symbols of Δ are absent in the plot). That is to say, fragmentation does not occur. Differently, in Fig. 3.6b-c, an abrupt drop of $\rho_{\min}$ is observed as a function of μ. Simultaneously, a non-zero Δ is detectable in these cases. Therefore, patterns become fragmented and that occurs beyond a critical value of ν, which decreases with μ.

A phase diagram, obtained from numerical simulations, which is presented in Fig. 3.7, depicts the regions in the $\mu - \nu$ plane where patterns can develop, and where they are fragmented or not. The white region on the left of the vertical solid line corresponds to the values of the exponents for which no patterns arise, according to the condition given by Eq. (3-5). At the same time,

[1] We identify this region as zero density, since the null state is numerically stable within it. Specifically, by zeroing the density values, they remain stable.

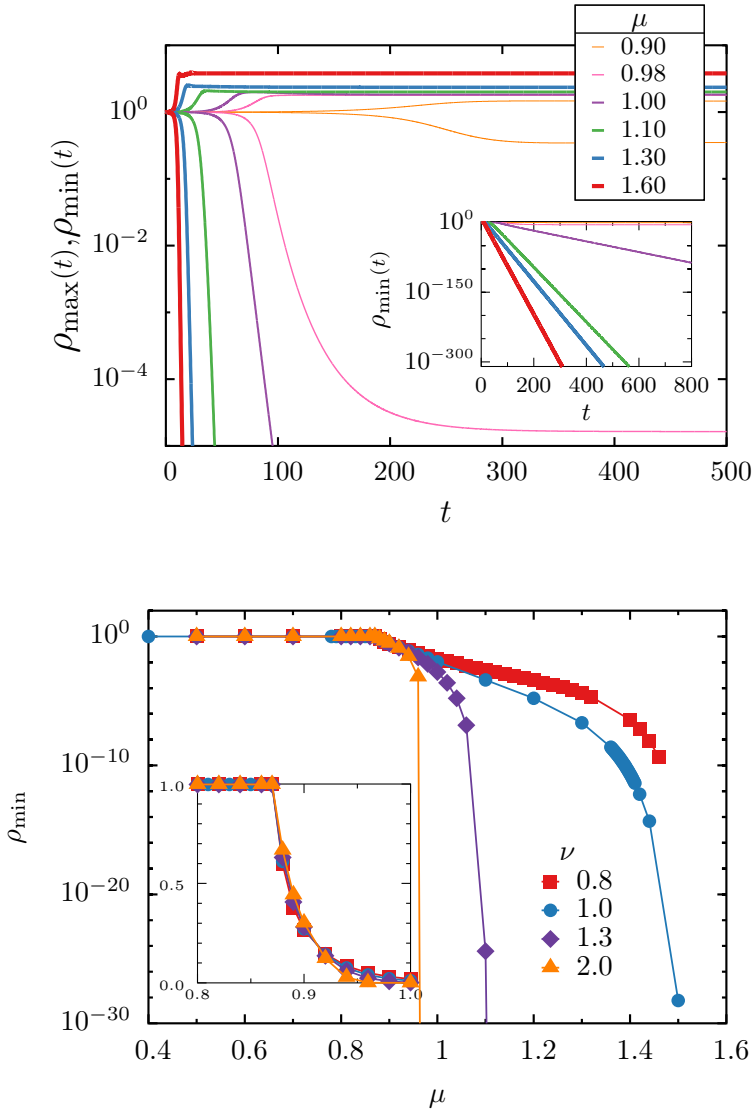

Figure 3.4: **Maximal and minimal densities:** (a) Temporal evolution of $\rho_{max}(t)$ and $\rho_{min}(t)$, for $\nu = 4.0$ and values of μ indicated in the legend. Inset: $\rho_{min}(t)$ on a larger scale. (b) Minimal density as a function of the growth exponent for different values of the diffusion exponent. Inset: the same, with another scale.

patterns emerge in the complementary domain. The solid dark area denotes fragmented patterns, as defined above.

Fragmentation occurs depending on the balance between diffusion and growth at low densities. Looking at Fig. 3.7, we see that fragmentation is favored when the diffusion coefficient and per capita reproduction rate increase super-linearly with the population concentration (ν and μ larger than one). Differently, when ν and μ are small, diffusion and per capita growth diverge at low densities, promoting the fast occupation of unpopulated regions, thus

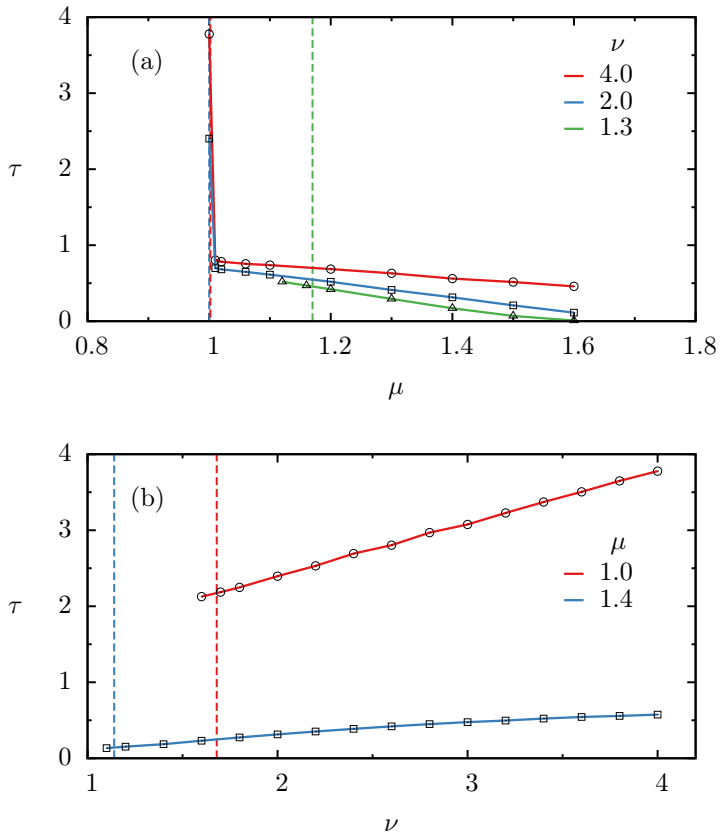

Figure 3.5: **Characteristic time** τ of the exponential decay of $\rho_{\min}(t) \sim \exp(-t/\tau)$ as a function of: (a) μ (for fixed values of ν) and (b) ν (for fixed μ), as indicated in the figures. The dashed vertical lines correspond to the values at which fragmentation occurs for the same color curve, as explained in the text.

connecting clusters.

More details about the pattern shape transitions are shown in Fig. 3.8. We see that, crossing the frontier of fragmentation along the line $\nu = 4$ (Fig. 3.8a), there is a smooth variation in the shape quantities σ, Δ and $\rho_{\max}$, as in the cases of Fig. 3.6. (Except that, as $\mu \to 2$, nonlinearities affect the number of peaks m and hence, the measured quantities.) But when ν becomes small, the behavior of pattern features changes. In Fig. 3.8b-c, we note a region where quantities that characterize the shape vary exponentially with μ, followed by a regime in which changes occur more rapidly. Note, for example, that while the height of a peak $\rho_{\max}$ rapidly increases, its width σ decreases with μ, suggesting that each peak tends to approach a Dirac delta-like profile. The effect is accentuated for small ν, as can be seen in Fig. 3.8c.

Moreover, it causes numerical difficulties. These difficulties prevent the determination of whether a Dirac delta is attained or not for finite μ, since

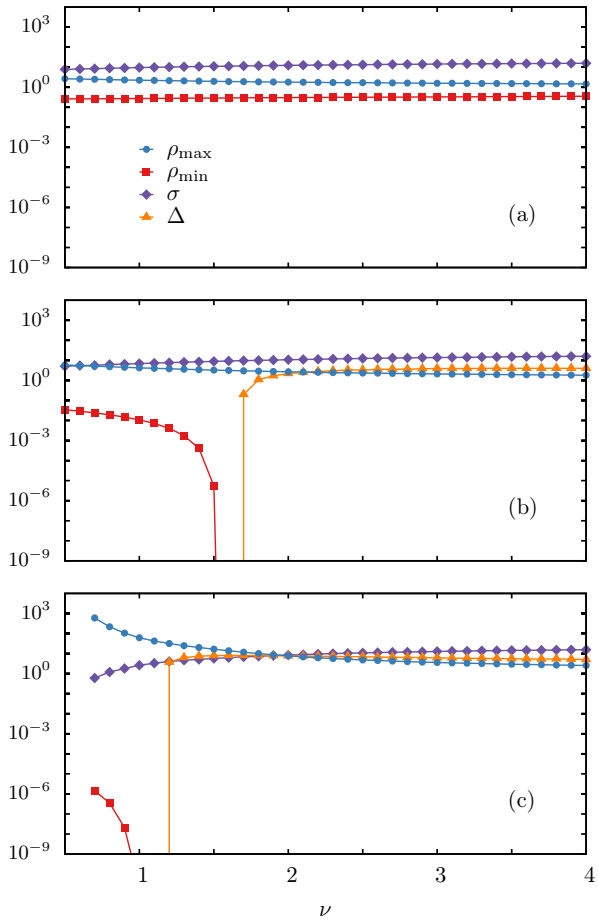

Figure 3.6: **Characteristics of the stationary profiles.** Stationary values of maximal density (ρ_{max}), minimal density (ρ_{min}), width at half height (σ) and valley width (Δ) as a function of ν, for (a) $\mu = 0.9$, (b) $\mu = 1.0$, (c) $\mu = 1.4$.

the increments dx and dt – used in simulations – must be reduced and thus, increase the computational cost, as we can see in the Fig. 3.9.

It is worth mentioning that, although the dependency of ρ_{min} on the model exponents is similar to the dependency in Fig. 3.6b-c, mainly the abrupt drop, we could not follow the behavior until ϱ is attained (or not) due to strong instability in the numerical integration when $\mu \to 2$ (hatched region in Fig. 3.7). Such complications interfere with a definite conclusion regarding the fragmentation process for large values of μ, and especially for small ν.

Finally, concerning the timescales of the pattern shape transition, we address further comments related to Fig. 3.5. For large values of ν ($\nu = 2.0, 4.0$ in Fig. 3.5a), the time τ explodes as μ approaches the critical value for fragmentation. In these cases, the characteristic time of relaxation towards a local null population level – when fragmentation occurs, and the time of relaxation towards a finite minimum population – when the opposite happens,

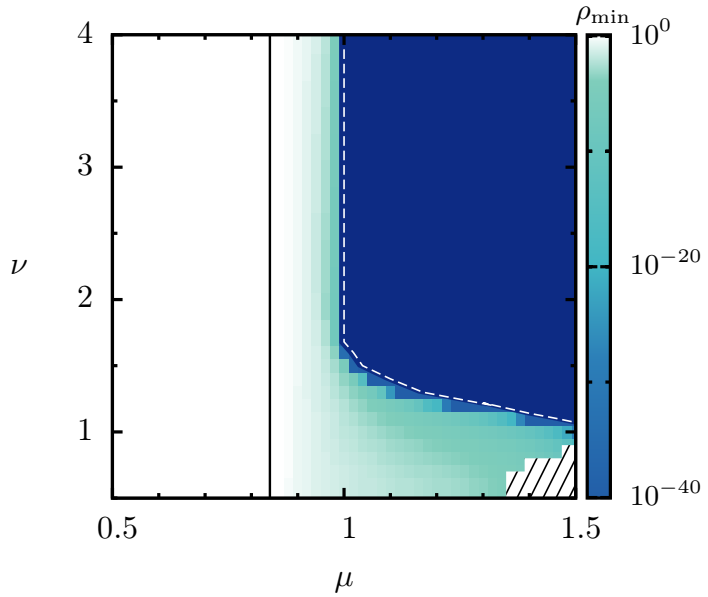

Figure 3.7: **Phase diagram in the $\mu - \nu$ plane.** The color scale represents the stationary minimal density $\rho_{\min}$.The vertical solid line at $\mu_p \simeq 0.84$ delimits superiorly the domain where no patterns are formed, according to Eq. (3-5). In that region, $\rho_{\min} = \rho_{\max} = 1$. Above μ_p, patterns emerge, and their minimal value gradually decreases. The dashed line separates the non-fragmented region, in color-scale, from the fragmented one, in solid dark color. The hatched region corresponds to non-calculated values due to computational limitations.

both suffer a drastic change. That is, along with the transition related to the minimum value of the stationary density $\rho_{\min}$, there is a transition in the time scale of the dynamics, which becomes slower when μ approaches the critical point (see Fig. 3.5a-b).

In contrast, there are other cases where a drastic change in the time scale is not observed, and there is continuity of the values of τ across the fragmentation boundary. That is, the time of decay of the density towards a finite level (on the left of the vertical lines in the figure) or towards zero (on the right of the vertical lines) does not suffer discontinuity. This indicates that, depending on the region of the $\mu - \nu$ plane, the transition to fragmentation can occur in two distinct ways.

3.4 Mathematical description of the patterns

We show in this section two mathematical descriptions of the patterns that emerge from the generalized Fisher-Kolmogorov-Petrovskii-Piskunov

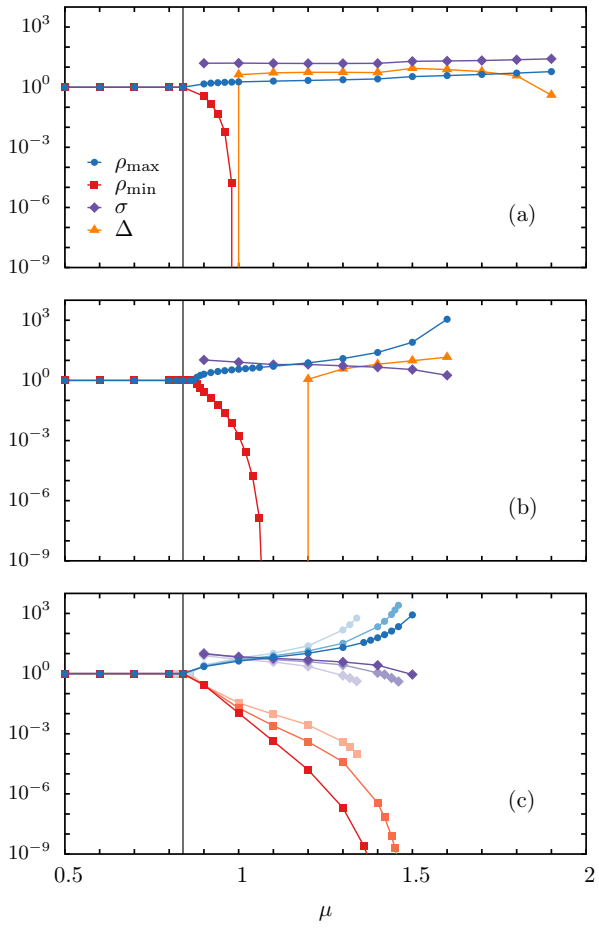

Figure 3.8: **Characteristics of the stationary profiles.** Stationary values of the maximal density ($\rho_{\max}$), minimal density ($\rho_{\min}$), width at half height (σ) and valley width (Δ) as a function of μ, for (a) $\nu = 4.0$, (b) $\nu = 1.3$ and (c) $\nu = 0.5$, 0.8 and 1.0, where more intense colors correspond to higher values of ν. The vertical lines represent $\mu_p \simeq 0.84$.

equation (Eq. 3-2), such as those we presented in Fig. 3.3. The first model is a periodic extension of a generalization of the Gaussian function, which describes all the curves in very good approximation. Besides, some specific patterns can also be approximated by the Fourier series expansion, using just a few terms, as we will see below.

3.4.1 Generalization of the Gaussian function

Inspired by the porous media equation [43],and other related ones [67, 68, 69, 48, 70] – to which the solutions resemble the curves of interest – we consider the ansatz

$$f(x) = A\left(1 - \frac{\beta x^2}{2s^2}\right)_+^{1/\beta}, \tag{3-7}$$

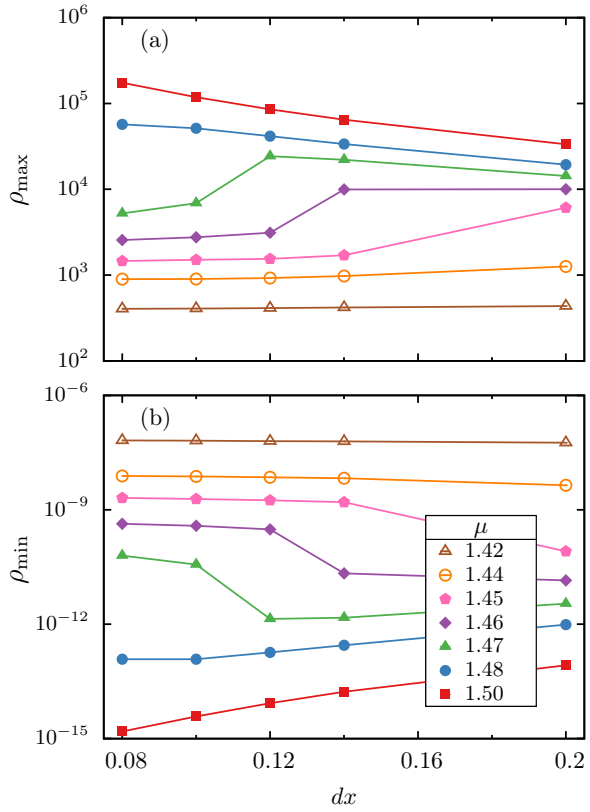

Figure 3.9: **Maximal and minimal values of the density as a function of integration spatial step** dx, for $\nu = 0.8$ and different values of μ. Some values of μ need a lower value of dx in the numerical simulation, in order to observe their convergence (hatched region in Fig. 3.7).

where A, s are positive constants, and β is real. The sub-index "+" means null value if the expression between parentheses is non-positive. That is, $f(x)$ has compact support $[-x_0, x_0]$, with $x_0 = s\sqrt{2/\beta}$.

If $\beta \to 0$, Eq. (3-7) results in the Gaussian function; otherwise, it represents the generalized Gaussian that arises within Tsallis statistics [71]. To describe the steady states observed in our case, we consider the periodic extension of Eq. (3-7) with period Λ, that is

$$f^{\text{ext}}(x) = \sum_{k\in\mathbb{Z}} f(x - k\Lambda). \tag{3-8}$$

Figure 3.10 shows stationary patterns – represented by the gray circles, adjusted by Eqs. (3-7)-(3-8) – represented by the red lines, and the Table 3.1 shows the values of the fitting parameters, where only one wavelength Λ of $\rho(x)$ (between successive minima of ρ) is ploted. Notice that the offset observed in some of the cases, arises from the superposition given by the periodic extension.

We observe, in Fig. 3.10 and Table 3.1, that when $\nu = \mu = 1$, the shape

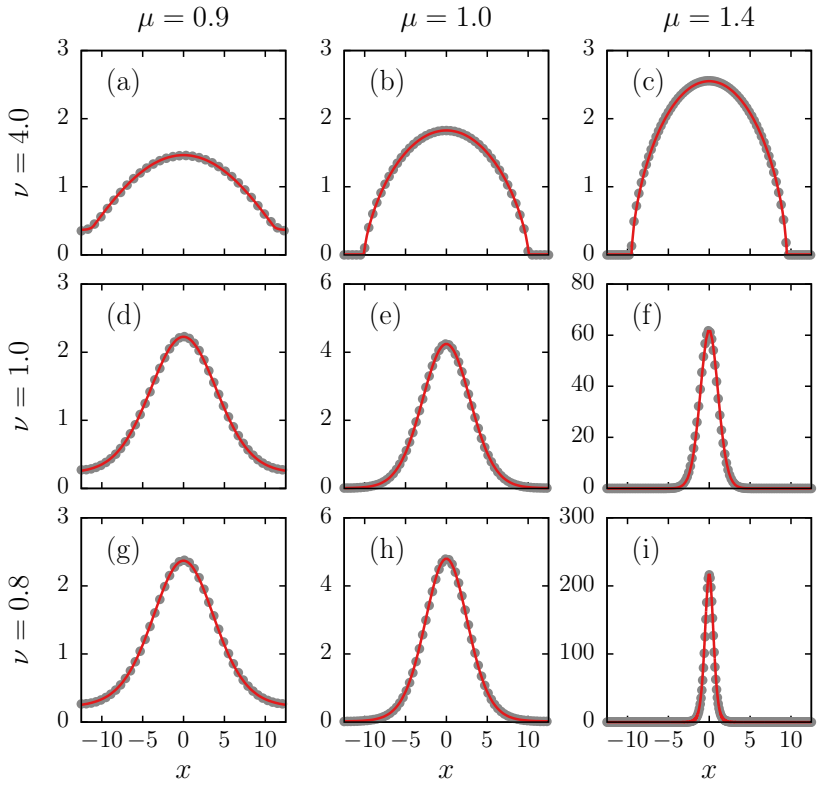

Figure 3.10: **Approximation by a generalization of the Gaussian function.** Stationary profiles obtained numerically – represented by the gray circles, along with the description given by Eq. (3-7) – represented by the red lines, for the values of μ, ν indicated in the figure. Fitting values of the parameters are given in Table 3.1.

		$\mu = 0.9$	$\mu = 1.0$	$\mu = 1.4$
$\nu = 4.0$	A	1.4645[7]	1.8264[7]	2.5578[6]
	β	0.793[3]	1.428[3]	1.594[2]
	s	8.761[9]	8.521[7]	8.501[4]
$\nu = 1.0$	A	2.222[1]	4.245[2]	61.5[2]
	β	-0.316[3]	-0.076[2]	-0.11[1]
	s	4.149[6]	2.912[3]	1.077[6]
$\nu = 0.8$	A	2.367[2]	4.797[8]	213.0[4]
	β	-0.395[4]	-0.153[7]	-0.259[8]
	s	3.777[9]	2.560[9]	0.472[2]

Table 3.1: Parameter values from the (nonlinear least-square) fitting of Eq. (3-8), in the interval $[-\Lambda, \Lambda]$, to stationary patterns displayed in Fig. 3.10, after centering a maximum at $x = 0$. The square brackets contain the estimated error in the least significant figure (e.g., the notation 213.0[4] stands for 213.0 ± 0.4).

is nearly Gaussian, since $\beta \simeq 0$. Gaussian approximations were found for a similar evolution equation with normal diffusion [55]. But when the exponents

become different from 1, deviations from the Gaussian form occur.

When $\nu > 1$ (subdiffusion), $\beta > 0$ and clusters are platykurtic. On the other hand, $\nu < 1$ (superdiffusion), $\beta < 0$ and clusters are leptokurtic. More importantly, according to Eq. (3-7), for $\beta > 0$, clusters have the compact-support property (smooth boundary for $0 < \beta < 1$ and sharp boundary for $\beta > 1$). This natural cut-off could, in principle, be associated with fragmentation. But since clusters are not isolated, there is an additional condition for fragmentation: clusters should not overlap. This condition occurs when the length of the support is shorter than the pattern wavelength, that is, $2x_0 < \Lambda$. It is interesting to point out that these conditions – not shown – match the fragmentation region relatively well, in the phase diagram of Fig. 3.7.

The accordance between the ansatz in Eq. (3-7) and numerical patterns opens an interesting question regarding the possibility of achieving, at least approximately, an analytical solution of Eq. (3-2), as found for some linear processes [52, 55, 72]. Nevertheless, from the direct substitution of the periodic ansatz into Eq. (3-2), a straightforward result was not found. Moreover, the relation between the ansatz exponent β and the model exponents μ, ν is not evident, but there is a strong trend given by a factor $(\nu-1)/2$ (see Fig. 3.11a).

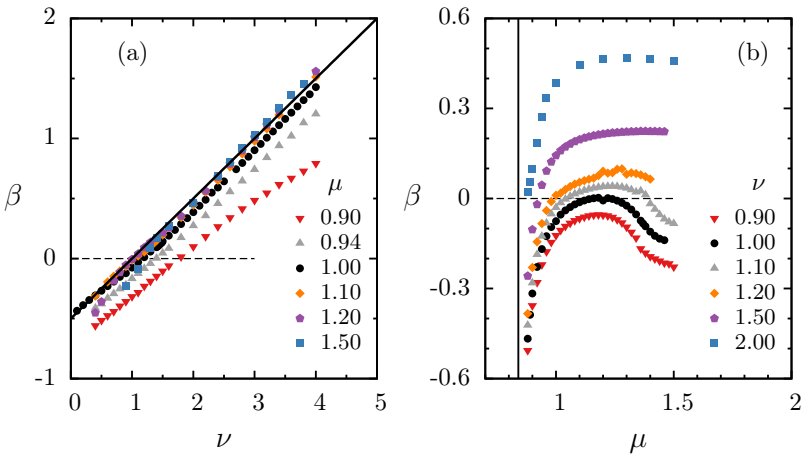

Figure 3.11: **Ansatz exponent** β as a function of model exponents ν (a), μ (b). The solid line in (a) corresponds to $\beta = (\nu - 1)/2$, drawn for comparison. The vertical solid line in (b) represents $\mu = \mu_p \simeq 0.84$. The value $\beta = 0$ is highlighted by dashed horizontal lines.

This main contribution to β corresponds to the exponent that emerges in the pure nonlinear diffusion [73]. Besides that, the exponent also depends on μ in a nontrivial way, as it can be seen in Fig. 3.11b, thus the values of β result from the interplay between both processes.

3.4.2 Fourier series expansion

We also performed Fourier series expansions of the curves in Fig. 3.3, such that the partial series of order n is given by

$$f_n(x) = \frac{\rho_0}{2} + \sum_{k=1}^{n} \rho_k \cos\left(\frac{kx\pi}{\Lambda/2}\right), \tag{3-9}$$

where the coefficients are given by

$$\rho_k = \frac{2}{\Lambda}\int_{-\Lambda/2}^{\Lambda/2} \rho(x) \cos\left(\frac{kx\pi}{\Lambda/2}\right) dx. \tag{3-10}$$

In Fig. 3.12, the gray circles represent $\rho(x)$ from numerical simulations, the green lines show the Fourier expansions of second order, $f_2(x)$, the red lines are $f_3(x)$, and the blue lines show $f_n(x)$, where the values of n are indicated in the legend. The insets show ρ_k vs k.

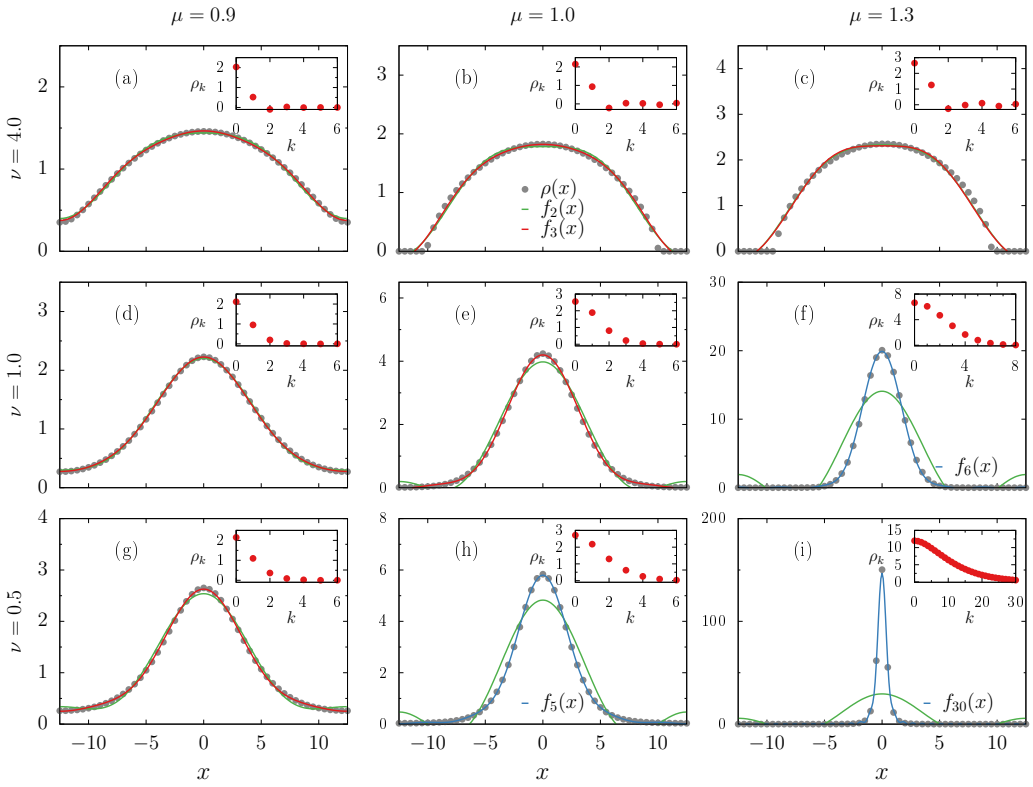

Figure 3.12: **Approximation by Fourier series expansion** for the values of μ, ν indicated in the figure. Inset: coefficients ρ_k, Eq. (3-10), as a function of k.

For some patterns, the coefficients rapidly tend to zero, and the associated series converges to $\rho(x)$ even for $n \leq 3$. However, higher terms will be needed for larger μ.

Differently from the case considered in [55] in which the first order approximation works well, it is required here a higher order term of the Fourier expansion.

So, in this section, we have an additional way to describe the patterns – under certain circumstances – that has a simpler expression and is easy to manipulate.

3.5 Summary and discussion

Using as a starting point a nonlocal Fisher-Kolmogorov-Petrovskii-Piskunov equation, which became a relevant description in mathematical biology [5, 8, 38, 41, 74, 75], we introduce density-dependent feedbacks in diffusion and growth processes, and investigate their effects in shaping the population distribution. We choose the particular form of power-law dependencies on the density, that allows contemplating a large class of responses to population density, as found in populations of insects, bacteria, vegetation, and among other cases – where diffusion and growth can be either enhanced or harmed by the concentration of individuals.

The emerging patterns have shapes ranging from mild oscillations around a reference level to disconnected clusters. The regulatory mechanisms of population growth, represented by μ, are crucial for the emergence of patterns as well as for their fragmentation. The same can be said about the type of diffusion controlled by ν, despite, in general, diffusion has a homogenizing effect.

Particularly, we focused on the self-induced population fragmentation, determining the conditions that nonlinearities must obey. Briefly, we observed that fragmentation is favored when growth and diffusion coefficients are positively correlated with population density. Moreover, it arises from a complex interplay between growth and dispersal processes, and nonlocality.

Beyond linear stability analysis, our results are supported by numerical simulations. Since Eq. (3-2) is nonlinear and nonlocal, it is difficult to access, analytically, the features of the stationary solutions. Despite that, analytical solutions can be obtained in very special cases. For instance, neglecting diffusion and considering constant growth rate ($\mu = 1$), for the homogeneous influence function, it is possible to obtain the peaks' shape [52, 72]. Regarding the role of density-dependent feedbacks, insights can be brought from studies out of the pattern formation context, where the evolution of a single peak follows a similar nonlinear but local equation [27, 43, 48, 70]. In these works, the single peak generated by power-law density-dependencies can have a shape,

which can range from concave to sharp, as found in the present context. In particular cases, the exact solutions fit into the class of a generalized Gaussian shape [43, 48, 70, 73].

These previous works motivated us to propose a periodic extension of that ansatz for the profiles shown in Fig. 3.3, namely Eq. (3-8), which describes remarkably well the numerical patterns (see Fig. 3.10). The parameter β in Eq. (3-7) can be used to characterize pattern shape. Notice that $\beta = 0$ corresponds to a Gaussian function, while $\beta > 0$ (< 0) to platykurtic (leptokurtic) clusters.

In particular, for $\beta > 0$, each individual cluster has compact-support. This condition is associated with the emergence of fragmentation, along with the constraint of non-overlap, $2x_0 < \Lambda$. These two conditions reproduce well the fragmented-patterns region in the phase diagram (Fig. 3.7), where $\rho_{\min} \to \varrho$. Let us mention that this phase diagram will change with other choices of the length ℓ of the box-like kernel, as well as of other shapes of the influence kernel, but it qualitatively exhibits the diversity of patterns that Eq. (3-7) can yield.

To establish a connection between the parameters $\{\mu, \nu\}$ in Eq. (3-2) and $\{A, s, \beta\}$ in Eq. (3-7), one also faces obstacles due to the particular nonlinear and nonlocal character of the dynamics. For instance, standard perturbative approaches can provide sine-like solutions near the transition to patterns (small-amplitude limit). However, these solutions cannot be analytically compared with the ansatz given by Eq. (3-8), since it has no closed form in Fourier-space. A perturbative treatment would find additional challenges related to the fact that fragmentation occurs far from the transition to patterns.

Regarding the definition of fragmentation, previous models for pattern formation that helped to explain self-organization in mussels [76], bacteria [34], vegetation under the sea [77] and in semi-arid ecosystems [38, 78], produce an arrangement of high density clusters interleaved by low density regions. In some cases, when clusters are sharply defined or well-spaced, the population level in between can be very low. More specifically, in these cases, population concentration is expected to decay exponentially as we move away from the peaks (see for instance Ref. [78]).

Taking into consideration that a biological population is constituted by a finite number of individuals, the occurrence of very low densities in the mean-field description can be associated with an effective fragmentation of the population. This is because in the continuous density description, it is possible to emulate the finiteness of the population by means of a threshold value, inversely proportional to the number of individuals and below which the density is considered null.

Under this perspective, the region for fragmentation in the phase diagram of Fig. 3.7 would be effectively enlarged as the number of individuals diminishes. In contrast, according to our model, density-dependent feedbacks drive the population density between clusters to zero in the long-time limit, such that the stationary profiles are composed by clusters with the compact-support property. As a consequence, actual fragmentation occurs and it is robust independently of the number of individuals, or threshold value, considered.

Beyond the nonlocal interactions embedded in the influence function, when there are isolated clusters, individuals are only in direct contact with those within the same cluster. This restricts the propagation of contact processes, such as diseases or information, transferred from one individual to another. Initiating the contagion within an isolated cluster, the affected population would be confined such as the recent covid-19 pandemic [79], (despite the human behavior being more complex); while, in non-fragmented patterns, the information can percolate to the whole population.

Furthermore, as widely studied in the context of metapopulations, a fragmented habitat can promote population segregation, which also brings consequences to the stability and diversity of ecosystems [59, 60]. In our case, the distinct profiles that emerge from the dynamics are also expected to influence the fate of the population.

4
Landscape-induced spatial oscillations in population dynamics

After having studied the spatial organization of single-species populations using the generalized FKPP equation in a homogeneous landscape, and understanding how the nonlocality and the nonlinearities affect the patterns, we will study in this chapter the dynamics of the population in a heterogeneous landscape, since, in biological systems, environmental factors can suffer spatial variations [3, 58, 80]. To discern the effect of the environment, we will remove the nonlinearities introduced in the previous chapter, considering $\nu = \mu = 1$.

Heterogeneity is commonly found in natural environment, [10, 81, 82, 83]. In this chapter, we explore the idea that they can stress the system and resonate with the internal scales, generating spatial oscillations in the distribution of the population [10, 81, 83]. We will focus on sharp spatial changes in the environmental conditions relevant for the population under consideration [3, 58, 84]. This kind of change is found in diverse situations in nature, e.g., on the interface between forest and grassland [58], at the bounds of oases [80] or harmful regions [38], or in artificial lab experiments [3], where there is a neat contrast of spatial domains with different growth rates.

We will see that three kinds of stationary (long time) population profiles can develop from the interface: *sustained oscillations* (or spatial patterns, without amplitude decay), *decaying oscillations* (with decreasing amplitude from the interface) or *exponential decay* towards a flat profile. These behaviors are represented schematically in Fig. 4.1, and will be discussed quantitatively later. The results of this research were published in Ref. [2].

4.1
Model

The generalized FKPP equation – presented in Sec. 2 and used in Sec. 3 – assumes a homogeneous environment, which is implicit in the coefficients that do not depend on the position. We consider the following extension of Eq. (2-5),

$$\partial_t \rho(x,t) = D\partial_{xx}\rho(x,t) + \Psi(x)\rho(x,t) - b\rho(x,t)[\gamma \star \rho](x,t)\,, \qquad (4\text{-}1)$$

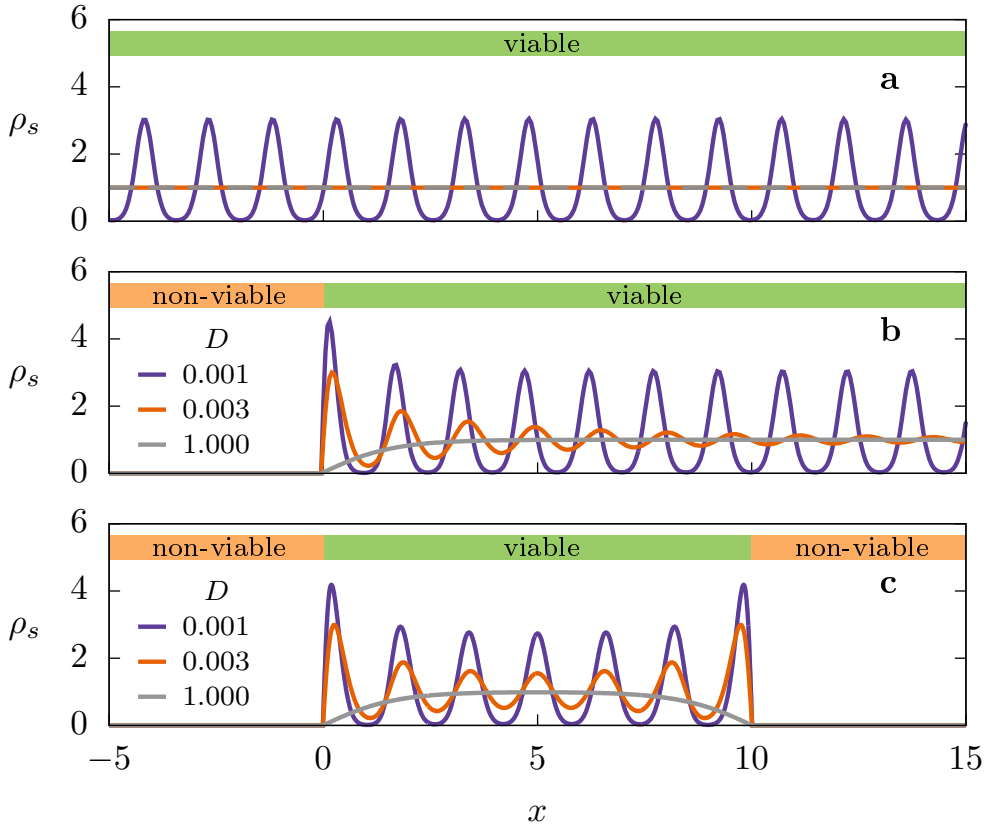

Figure 4.1: **Population distribution in an environment that is: (a) homogeneously viable; (b) heterogeneous, with viable and non-viable regions; and (c) heterogeneous, with a viable region between non-viable ones.** Depending on the values of the parameters in Eq. (4-1), spatial patterns can: develop around the uniform steady state in (a); and be preserved in the viable region of the corresponding cases, in (b) - (c). But even when the steady-state is uniform in case (a), decaying oscillations can emerge in (b) - (c). The parameters are $a = b = 1$; values of D are provided in the legend; and for the kernel γ_q defined in Eq. (4-2), we set $q = -0.5$ and $\ell = 2$. For panel (b) and (c), A in Eqs. (4-10)-(4-5) is $A \to \infty$.

where the spatially-dependent reproduction rate $\Psi(x)$ reflects the overall habitat quality at a given location x [58]. Since we want to study sharp spatial changes, we attribute the Heaviside step or rectangular functions to $\Psi(x)$.

As for the kernel, we have chosen two families of influence functions that allow us to continuously vary its compactness, as represented in Fig. 4.2a-c. See Ap. A for other kernels.

The first one is the kernel based on a normalized generalization of the exponential function, known as q-exponential [85], defined by

$$\gamma_q(x) = \frac{2-q}{2\ell}[1-(1-q)|x|/\ell]_+^{1/(1-q)} \equiv \frac{2-q}{2\ell}\exp_q(|x|/\ell)\,, \qquad (4\text{-}2)$$

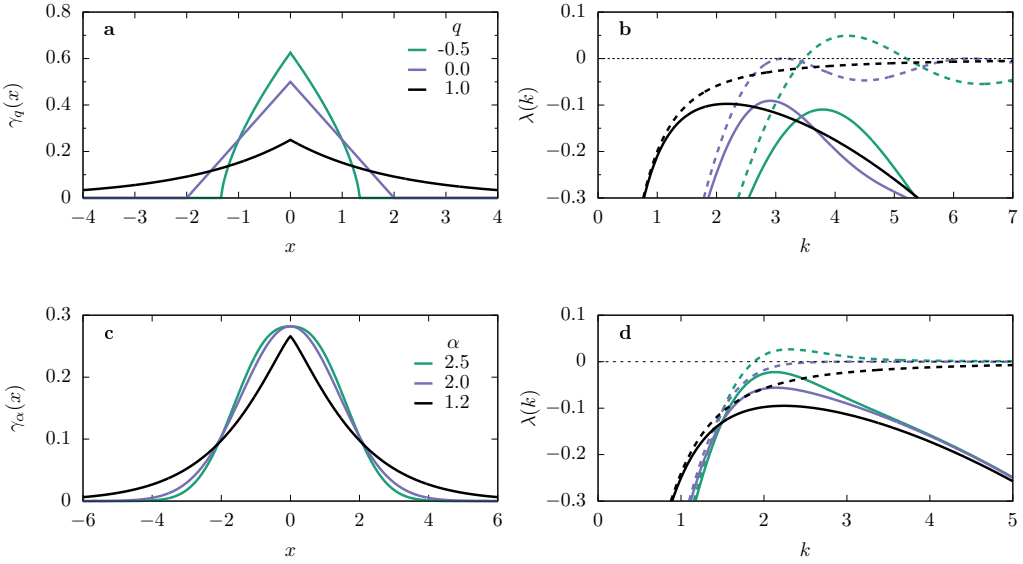

Figure 4.2: **Interaction kernel and mode stability in a homogeneous environment.** (a) $\gamma_q(x)$, defined in Eq. (4-2), for the values of q indicated on the figure, and $\ell = 2$. (b) Mode growth rate $\lambda(k)$, corresponding to the values of q plotted in (a). (c) $\gamma_\alpha(x)$, defined in Eq. (4-3), for the values of α indicated on the figure, and $\ell = 2$. (d) Mode growth rate $\lambda(k)$, corresponding to the values of α plotted in (c). While the case $q = 0$ (triangular kernel) is the critical one – for which the maximal value of $\lambda(k^\star) = 0$ at finite $k^\star$, when $D = 0$, the critical one for γ_α is $\alpha = 2$. We use $a = b = 1$ for the panels (b) and (d), and dashed lines correspond to $D = 0$, whereas solid lines correspond to $D = 0.01$. Notice that, when diffusion is absent, the mode growth rate is proportional to the kernel Fourier transform.

where q and ℓ control the shape of the kernel. The sub index $+$ means $[z]_+ = 0$ if $z \leq 0$.

In the limit $q \to 1$, the standard exponential is approached yielding $\gamma_1(x) \propto e^{-|x|/\ell}$. In the critical case $q = 0$, $\gamma_q(x)$ produces the triangular kernel, which Fourier transform is $\tilde{\gamma}_0(k) = \sin^2(k\ell)/(k\ell)^2$. The kernel shapes are illustrated in Fig. 4.2a. As we will see, it is especially relevant that, only for $q < 0$, can the Fourier transform of $\gamma_q(x)$ take negative values. Then, we focus on the range $-1 \leq q < 1$, around this critical value. Moreover, in this range, the interaction is restricted to a finite region and the kernel moments are well-defined, a fact that will facilitate both: the numerical and the theoretical approaches.

We also consider, as a second class of kernels, the stretched exponential family defined by

$$\gamma_\alpha(x) = \frac{e^{-(|x|/\ell)^\alpha}}{2\ell\,\Gamma(1+1/\alpha)}\,, \tag{4-3}$$

with $\alpha > 0$ for normalizability. When $\alpha = 1$, the stretched exponential

family produces the double exponential kernel, which Fourier transform is $\tilde{\gamma}_1(k) = \frac{1}{1+\ell^2 k^2}$. That includes the Gaussian ($\alpha = 2$), which Fourier transform is $\tilde{\gamma}_2(k) = e^{-\ell^2 k^2/4}$. And it also reproduces the top-hat kernel in the limit $\alpha \to \infty$. The Fourier transform of $\gamma_\alpha(x)$ can take negative values if $\alpha > 2$.

For a homogeneous landscape, $\Psi(x) = a$, from the linear stability analysis, we find the mode growth rate $\lambda(k)$, which was presented in Sec. 2, such as

$$\lambda(k) = -Dk^2 - a\tilde{\gamma}(k)\,, \tag{4-4}$$

is plotted in Fig. 4.2b (d), for each kernel γ_q (γ_α) shown in Fig. 4.2a (c).

Note that, $\lambda(k) > 0$ occurs for sufficiently small D if the Fourier transform of the kernel takes some negative values. Then, by substituting $\tilde{\gamma}$ into Eq. (4-4), we conclude that sustained oscillations can only appear if $q < 0$ ($\alpha > 2$). This is a necessary but not sufficient condition that arises by imposing $\lambda(k^\star) > 0$ in the most favorable case $D = 0$ (hence $\tilde{\gamma}(k^\star) < 0$), to induce the growth of certain modes. Remembering that $k^\star$ is the dominant mode.

In contrast, for $q \geq 0$ ($\alpha \leq 2$), the uniform state is intrinsically stable (that is, independently of the remaining parameters). In Fig. 4.2b(d), we plot the mode growth rate for $D = 0$ and $D > 0$, which shows how diffusion affects mode stability, damping fluctuations.

Concerning the interaction length $\ell > 0$, when $D = 0$, the mode growth rate is a function of $k\ell$ only, then ℓ acts just as a scale factor. Therefore, when ℓ goes to zero (implying local dynamics), the dominant wavenumber $k^\star$ is shifted to infinity, meaning that patterns go continuously to a flat profile in that limit. In contrast, for $D > 0$, the first term in Eq. (4-4) has a more homogenizing effect the larger is $k^\star$, hence the smaller is ℓ.

As a consequence, there is a critical value of ℓ, below which patterns do not emerge, even if for finite ℓ there is nonlocality [53]. Finally, there is also a critical value of a_c of the reproduction rate, when $D > 0$, and with all the other parameters fixed, such that sustained oscillations emerge only for $a > a_c$.

In summary, in the cases where $\lambda(k^\star) \leq 0$ (i.e., either $q \geq 0$, or alternatives involving $q < 0$, such as large enough D, small enough ℓ) or small enough a, information regarding the interaction scale ℓ or other details of the kernel profile are not stamped in the spatial distribution $\rho(x,t)$, which becomes uniform at long times.

It is worth noting that: although one has finite support (γ_q), the other has tails (γ_α) below the critical value; however, both are qualitatively similar, as we will confirm later. Therefore, we are going to use the family of the q-exponential kernel, and then, we extend the result to stretched exponential.

4.2 Numerical results

In this section, the heterogeneity of the landscape is introduced by assuming that its profile can be written as $\Psi(x) = a + \psi(x)$, where $\psi(x)$ represents the spatial variations of the environment around a reference level a.

The results that we will present were obtained through theoretical and numerical techniques. The theoretical approach is based on mode linear stability analysis. In parallel, we will show results obtained by numerically solving Eq. (4-1).

4.2.1 Refuge

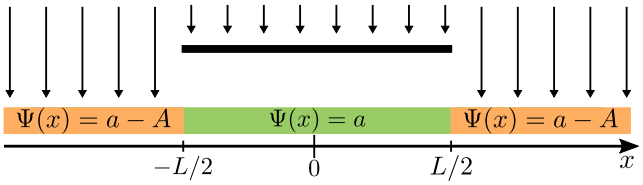

Figure 4.3: **Pictorial representation of a one-dimensional refuge.** Within the L size refuge, the damaging A effect is blocked.

As paradigm of a heterogeneous environment with sharp borders, we first consider that the spatial variations around the reference level a are given by

$$\psi(x) = -A[1 - \Theta(L/2 - |x|)]\,, \tag{4-5}$$

where Θ is the Heaviside step function and $A > 0$. This equation represents a refuge of size L with growth rate a, immersed in a less viable environment with growth rate $a - A$, as depicted in Fig. 4.3.

In a laboratory situation this can be constructed by means of a mask delimiting a region that protects organisms from some harmful agent. For instance, shielding bacteria from UV radiation [3]. In natural environments, this type of localized disturbance appears due to changes in the geographical and local climate conditions[58], or even engineered by other species [38].

In Sec. 4.1, we have seen that the uniform distribution is intrinsically stable when $q \geq 0$. In contrast, even if for $q \geq 0$, spatial structures can emerge due to heterogeneities in $\Psi(x)$, as illustrated in Fig. 4.4 for the case $D = 0.01$.

In the limit of weak heterogeneity, i.e., under the condition $|\psi(x)|/a \ll 1$, we obtain an approximate analytical solution assuming that the steady solution of Eq. (4-1) can be expressed in terms of a small deviation $\varepsilon(x)$ around the homogeneous state $\rho_0 = a/b$. Then, when we substitute $\rho(x) = \rho_0 + \varepsilon(x)$ into

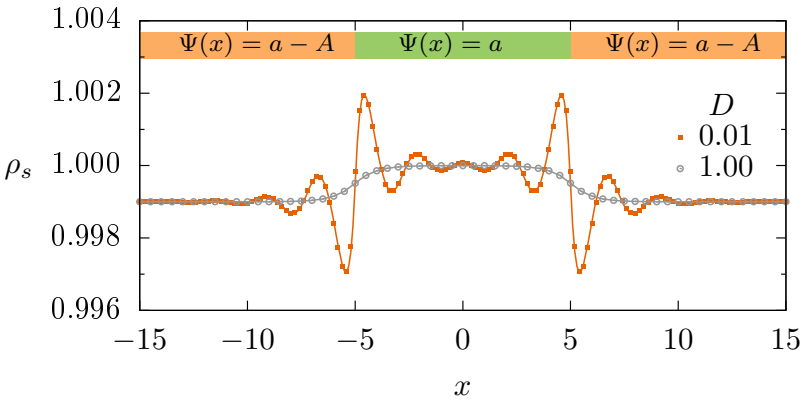

Figure 4.4: **Stationary population density ρ_s vs. x in a refuge.** This heterogeneous environment is defined by Eq. (4-5), with $a = b = 1$, $A = 10^{-3}$ and $L = 10$. The vertical lines indicate the refuge boundaries. We used the kernel $\gamma_q(x)$, with $q = 0.1$ and $\ell = 2$, and two different values of D. Symbols are results from numerical integration of Eq. (4-1), and solid lines, from the small-A approximation given by Eq. (4-9) – in excellent accordance with the exact numerical solution. Let's recall that, in a homogeneous environment, no oscillations appear for $q \geq 0$.

the Eq. (4-1), we obtain

$$\partial_t \varepsilon = D\partial_{xx}\varepsilon + (a + \psi(x))(\rho_0 + \varepsilon) - b(\rho_0 + \varepsilon)[\gamma \star (\rho_0 + \varepsilon)]\,, \tag{4-6}$$

where, the last term is

$$b(\rho_0 + \varepsilon)[\gamma \star (\rho_0 + \varepsilon)] = b\rho_0^2 + b\rho_0(\gamma \star \varepsilon) + b\varepsilon\rho_0 + \mathcal{O}(\varepsilon^2) \tag{4-7}$$

discard terms of order equal or higher than, $\mathcal{O}(\varepsilon^2, A\varepsilon, A^2)$, and Fourier transform, we obtain

$$\tilde{\rho}_s(k) = 2\pi\rho_0\delta(k) + \frac{\rho_0\tilde{\psi}(k)}{-\lambda(k)}\,, \tag{4-8}$$

where $\lambda(k)$ was already defined in Eq. (4-4) and $\tilde{\psi}(k)$ is the Fourier transform of the small fluctuations in the landscape quality, which, for the case of Eq. (4-5) is $\tilde{\psi}(k) = A[2\sin(Lk/2)/k - 2\pi\delta(k)]$.

Finally, assuming that $\lambda(k^\star) < 0$, the steady density distribution is given by $\rho_s = \rho_0 + \varepsilon_s$, that is,

$$\rho_s(x) = \rho_0 + \mathcal{F}^{-1}\left\{\frac{\rho_0\tilde{\psi}(k)}{-\lambda(k)}\right\}\,, \tag{4-9}$$

where the inverse Fourier transform $\mathcal{F}^{-1}$ must be numerically computed in general. For small heterogeneity, Eq. (4-9) is in very good accordance with the exact numerical solution obtained by integration of the dynamics Eq. (4-1), as it can be seen in Fig. 4.4. Notice the two different profiles, depending on the

diffusion coefficient D: one gently following the landscape heterogeneity, and the other strongly oscillatory.

For small D, the induced oscillations display two evident characteristics, which depend on $\tilde{\gamma}_q$: well-defined wavenumber and decaying amplitude for increasing distances from the interfaces at $x = \pm L/2$ (highlighted by dashed vertical lines in Fig. 4.4). We will see that the details of the kernel γ_q can be seen through the characteristics of the oscillations.

4.2.2 Semi-infinite habitat

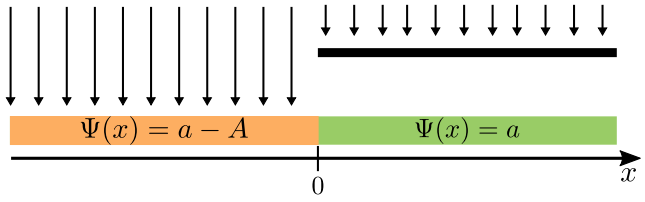

Figure 4.5: **Pictorial representation of a semi-infinite habitat.** For $x \geq 0$ the harmful effect A is blocked.

Since oscillations are induced by changes in the landscape, it is worth focusing, from now on, on one of the interfaces. Moreover, we assume a refuge much larger than the wavelength of the oscillations, sufficient to follow over several cycles the structure originated on the interface. To do that, we consider a semi-infinite habitat defined by

$$\psi(x) = -A\Theta(-x)\,, \tag{4-10}$$

where for convenience the interface was shifted to $x = 0$, such that the low-quality region is at $x < 0$, as depicted in Fi. 4.5.

As an additional feature, we consider that the harmful conditions are very strong, that is, $A \to \infty$. The purpose is twofold: on the one hand, it allows to test the robustness of the results beyond the small-A approximation; on the other hand, it allows a simplification as it follows. When $A \gg a$, ρ is very small in the unfavorable region. Then, the nonlinear competition term can be neglected, and the Eq. (4-1) can be approximate by

$$\partial_t \rho(x \leq 0, t) \simeq D\partial_{xx}\rho + (a - A)\rho, \tag{4-11}$$

so, the stationary solution is

$$\rho(x \leq 0) \sim e^{\sqrt{(A-a)/D}\,x}, \tag{4-12}$$

leading to a steady distribution that decays exponentially from the interface, as observed in Fig. 4.6. Thus, in the limit $A \to \infty$, we have $\rho(x \leq 0, t) = 0$. This is the setting used to produce Fig. 4.1b, by numerical integration of Eq. (4-1).

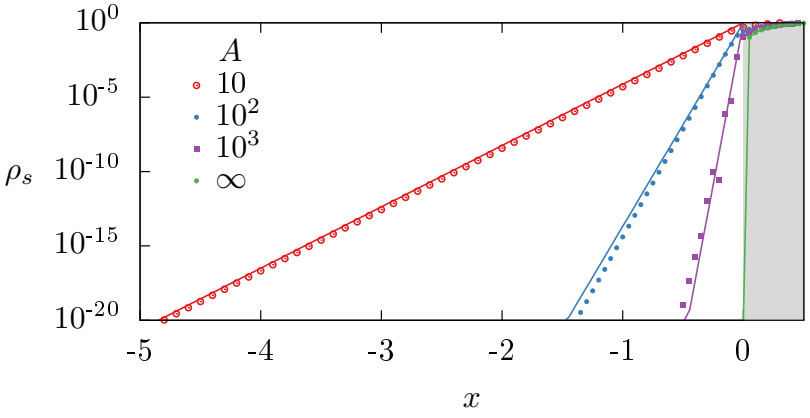

Figure 4.6: **Decay exponential from the interface ($A >> a$).** Numerical integration of Eq. (4-1) (dots in the figure), and exponential decay predicted by Eq. (4-12) (solid lines) for the kernel γ_q with $q = 0.1$ and $\ell = 2$. The grey region represents the refuge and we use $D = 0.1$ and the values of A are given on the legend.

As sketched in Fig. 4.7, for each steady distribution attained at long times, we measure the wavelength, from which we obtain the wavenumber $\bar{k}$, and the decay length $\bar{x}$, by observing that the envelope of the oscillations decays as $\exp(-x/\bar{x})$.

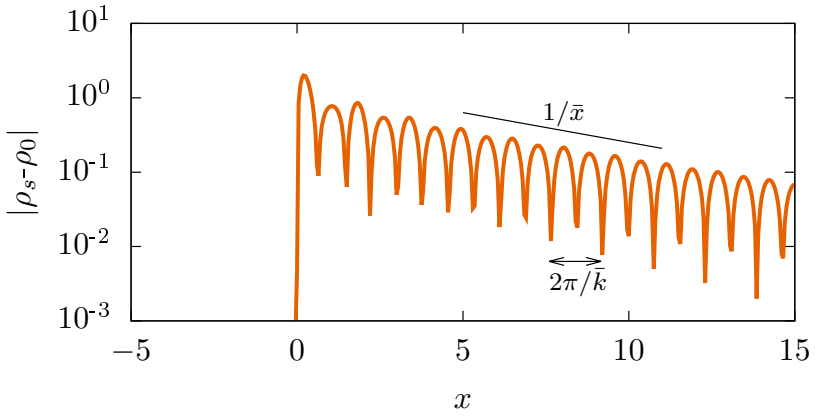

Figure 4.7: **Characterization of stationary profiles.** Long-time solutions approach a stationary state characterized by the wavelength $2\pi/\bar{k}$ and the decay length $\bar{x}$. This example was obtained from numerical integration of Eq. (4-1), assuming a semi-infinite habitat, with parameters $D = 0.003$, $\gamma_q(x)$ with $\ell = 2$ and $q = -0.5$.

The stationary spatial structures that emerge for $x > 0$ can be classified into the three types depicted in Fig. 4.1b and Fig. 4.8:

(i) *sustained oscillations* (lilac line, with $\bar{k} > 0$ and $\bar{x} \to \infty$);

(ii) *decaying oscillations* (orange line, with $\bar{k} > 0$ and finite $\bar{x}$);

(iii) *exponential decay* (gray line $\bar{k} = 0$ and finite $\bar{x}$).

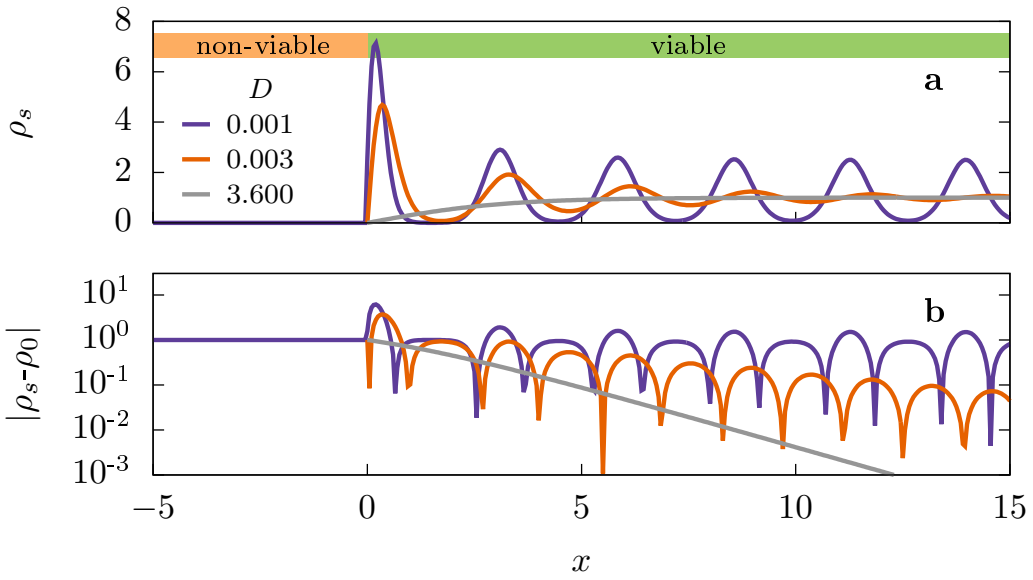

Figure 4.8: **Long-time solutions of a population in a semi-infinite habitat. (a) Stationary density, (b) Density variation around the homogeneous solution.** Parameters are $a = b = 1$, $A \to \infty$, values of D are given on the legend, and for kernel γ_α defined in Eq. (4-3), $\alpha = 2.3$ and $\ell = 2$. Note that the profiles are similar to those obtained in Fig. 4.1b.

Observing Fig. 4.8, which was obtained from a numerical simulation using the stretched kernel, by Eq. (4-3), one can note the similarity with the other family of kernels adopted in Fig. 4.1b (using γ_q).

In these figures, three types of profiles appear when D changes. We also systematically varied the shape parameter q to construct the phase diagram in the plane $q - D$ presented in Fig. 4.9a. Similarly, we will see further the phase diagram in the plane $(2 - \alpha) - D$ in Fig. 4.11a.

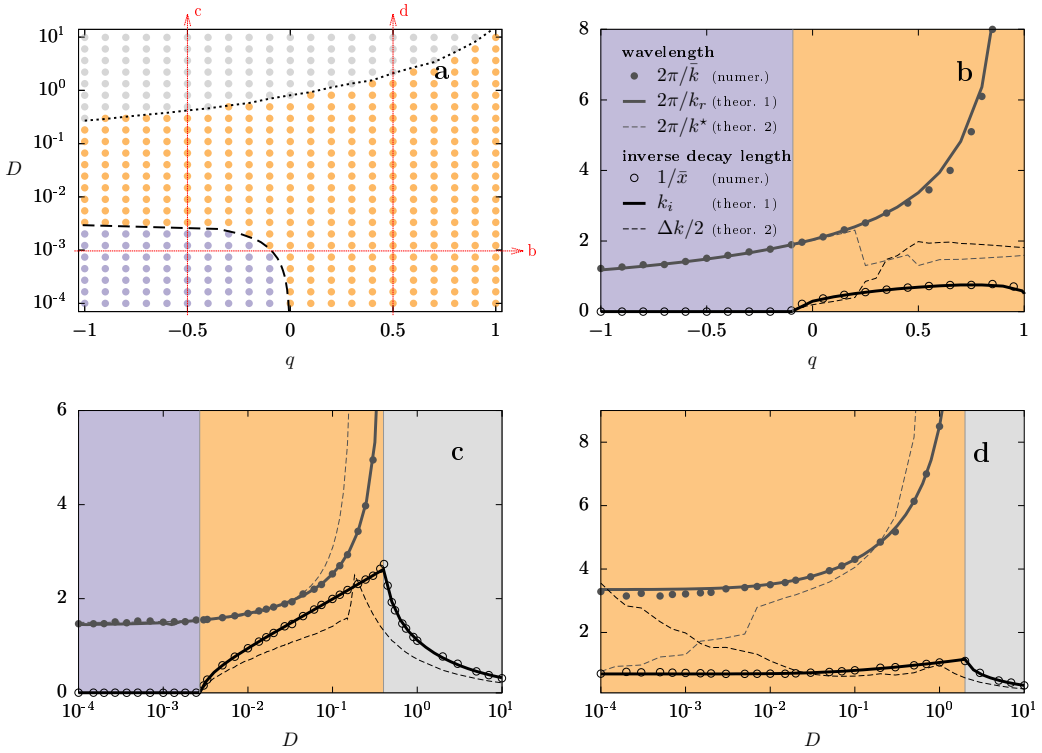

Figure 4.9: **Phase diagram and characteristics of the stationary profiles as a function of diffusion coefficient D and q,** in the semi-infinite habitat. We used the kernel $\gamma_q(x)$, with $\ell = 2$. (a) Phase diagram on the $q - D$ plane, and cut at (b) $D = 10^{-3}$, (c) $q = -0.5$ (d) $q = 0.5$. The remaining parameters are $a = b = 1$. In diagram (a), for each point on the grid, the type of regime was determined based on the values of $2\pi/\bar{k}$ and $\bar{x}$ that characterize the solutions of Eq. (4-1): *sustained oscillations* ($\bar{k} > 0$ and $\bar{x} \to \infty$, lilac), *decaying oscillations* ($\bar{k} > 0$ and finite $\bar{x}$, orange), and *pure exponential decay* ($\bar{k} = 0$ and finite $\bar{x}$, gray). The lines between regimes were determined from $k = \pm k_r + ik_i$, the complex pole of $\tilde{R}(k)$ with the smallest positive imaginary part (dashed line for $k_i = 0$ and dotted line for $k_r = 0$). Its components were also used to determine the full-lines (theoretical 1) in panels (b)-(d). The symbols correspond to measurements of numerical profiles and the thin dashed lines to the harmonic estimate (theoretical 2) given by Eq. (4-19).

4.3 Theoretical framework

To perform a theoretical prediction of $\bar{k}$ and $\bar{x}$, within the linear approximation, we consider that these oscillation parameters should be related to the poles of the integrand $e^{ikx}\tilde{\psi}(k)/[-\lambda(k)]$ in the expression for the inverse Fourier transform that provides the solution, according to Eq. (4-9). As far as the external field $\psi(x)$ does not introduce non-trivial poles, like in the case of a Heaviside step function ($\tilde{\psi}(k) \sim 1/k$), only the complex zeros of $\lambda(k)$ matter.

The dominant mode (the mode that decays more slowly) is given by the pole $k_r + ik_i$ with minimal positive imaginary part; which, except for amplitude and phase constants, will provide approximately patterns of the form $\mathrm{e}^{-k_i x}\cos(k_r x)$, allowing the identifications $\bar{k} = k_r$ and $1/\bar{x} = k_i$. The zeros of $\lambda(k)$ were obtained numerically, by using the Taylor expansion of $\lambda(k)$ around $k = 0$ and solving $Dk^2 + \sum_{n=0}^{N} \frac{1}{n!}\frac{d^n\tilde{\gamma}}{dk^n}|_{k=0}\, k^n = 0$, in the limit of sufficiently large N (See Ap. C). This calculation is in very good accordance with the results of numerical simulations presented in Fig. 4.9 (called theor. 1), explaining the observed regimes (see Tab. 4.1). In fact, the modes that persist beyond the interface have relatively small amplitudes, so that the system response is approximately linear in this region.

Regime	Zeros of $\lambda(k)$	Characteristics of poles
Exponential decay	$k_r = 0$	Pure imaginary
Decaying oscillations	$k_r, k_i \neq 0$	Complex conjugate
Sustained oscillations	$k_i = 0$	Two real roots

Table 4.1: **Characteristics of poles.** Predictions of the oscillatory regime by poles of $1/\lambda(k)$, used as *theoretical 1* in Figs. 4.9 and 4.11.

Recall that this analysis assumes mode stability ($\lambda(k) < 0$). When $\lambda(k^\star) > 0$, the system is intrinsically unstable, with the poles having a null imaginary part (lying on the real axis). Nevertheless, the initially fastest growing mode, given by the maximum of $\lambda(k)$, tends to remain the dominant one in the long term [53], yielding $\bar{k} \simeq k^\star$ for the sustained oscillations ($\bar{x} \to \infty$).

Alternatively, to obtain further insights, it is useful to consider the response function $\tilde{R}(k)$ that, from Eq. (4-8), is

$$\tilde{R}(k) \equiv \frac{|\tilde{\varepsilon}_s(k)|^2}{|\tilde{\psi}(k)|^2} = \frac{\rho_0^2}{\lambda^2(k)}\,. \tag{4-13}$$

Moreover, despite it missing some information on the dynamics (contained in the phase of $\lambda(k)$), it can provide a more direct estimation of the observed parameters than through poles calculations. In order to do that, we resort to the bell-shaped response of a forced linear oscillator, described by

$$\ddot{y} + 2\zeta k_0 \dot{y} + k_0^2 y = f(x)\,, \tag{4-14}$$

where ζ is the damping coefficient, k_0 the natural frequency of the system, and $f(x)$ the external forcing, in Fourier space we have

$$-\lambda_H(k)\tilde{y} \equiv (-k^2 + 2\zeta k_0 ki + k_0^2)\,\tilde{y}(k) = \tilde{f}(k)\,, \tag{4-15}$$

which the response function is

$$\tilde{R}_H(k) \equiv \frac{1}{|\lambda_H(k)|^2} = \frac{1}{(k^2 - k_0^2)^2 + 4\zeta^2 k_0^2 k^2}\,, \tag{4-16}$$

whose zeros (poles of $1/\lambda_H(k)$) are

$$k = k_0(\pm\sqrt{1-\zeta^2} + i\zeta). \tag{4-17}$$

Note that, under a step forcing $f(x) = k_0^2\Theta(x)$, which simulates our present setting, those poles carry the essential information of the damped oscillation solution, given by $\tilde{y}(k) = \tilde{f}(k)/[-\lambda_H(k)]$. In the underdamped case ($\zeta < 1$), this solution is explicitly given by

$$y(x) = \left[1 - \frac{k_0}{\kappa} e^{-x/\xi}\sin(\kappa x + \phi)\right]\Theta(x)\,, \tag{4-18}$$

where $\kappa = k_0\sqrt{1-\zeta^2}$, real parte of Eq. (4-17), $\xi = 1/(\zeta k_0)$, the inverse of the imaginary part of Eq. (4-17), and the phase constant $\phi = \tan^{-1}(\xi\kappa)$.

The solution for the overdamped case emerges for $\zeta > 1$, when the zeros of $\lambda(k)$ are pure imaginary with $k_i = k_0(\zeta \pm \sqrt{\zeta^2 - 1})$. The connection between the poles of $\tilde{R}_H(k)$ and the dynamic solution is possible because, as previously discussed, $\tilde{f}$ does not introduce relevant poles, and the forced solution has a similar form to the homogeneous one for more details.

	Steady density distribution	Forced linear oscillator
External driving force	$\psi(x) = -A\Theta(-x)$	$f(x) = k_0^2\Theta(x)$
FT equation	$\tilde{\varepsilon}_s(k) = \dfrac{\rho_0\tilde{\psi}(k)}{-\lambda(k)}$	$\tilde{y}(k) = \dfrac{\tilde{f}(k)}{-\lambda_H(k)}$
Mode growth rate	$\lambda(k) = -Dk^2 - a\tilde{\gamma}(k)$	$-\lambda_H(k) = -k^2 + i2\zeta k_0 k + k_0^2$
Response function	$\tilde{R}(k) = \left\lvert\dfrac{\tilde{\varepsilon}_s(k)}{\tilde{\psi}(k)}\right\rvert^2 = \dfrac{\rho_0^2}{\lvert\lambda(k)\rvert^2}$	$\tilde{R}_H(k) = \left\lvert\dfrac{\tilde{y}(k)}{\tilde{f}(k)}\right\rvert^2 = \dfrac{1}{\lvert\lambda_H(k)\rvert^2}$

Table 4.2: **Summary of the analogy made between the solution of the steady-state density distribution and the forced linear oscillator.** These results were used as a base to *theoretical 2* in Figs. 4.9 and 4.11. Remembering that $\rho_s = \rho_0 + \varepsilon_s$.

The harmonic model is, in fact, the minimal model for the observed

structures and the correspondence between Eqs. (4-16) and (4-18) , which will allow the estimation of the oscillation features. In the limit of small ζ, $\tilde{R}_H(k)$ there is a sharp peak, characterized by a large quality factor $Q \equiv k^\star/\Delta k$, where Δk is the bandwidth at half-height of $\tilde{R}(k)$ around $k^\star$ [1]. First, we see that the position of the peak of $\tilde{R}_H$ approximately gives the oscillation mode κ, according to $k^\star = k_0\sqrt{1-2\zeta^2} = \kappa + \mathcal{O}(\zeta^2)$. Second, the bandwidth is related to the decay length through $\Delta k = 2/\bar{x} + \mathcal{O}(\zeta^2)$ [86].

Combining all together, as long as $\tilde{R}(k)$ resembles the bell-shaped form of $\tilde{R}_H(k)$, we can use, at first order in ζ, the estimates

$$\bar{k} \simeq \arg\max_k (\tilde{R}) \equiv k^\star \quad \text{and} \quad \bar{x} \simeq \frac{2}{\Delta k}\,. \tag{4-19}$$

The expression for $\bar{x}$ is also valid in the overdamped limit of large ζ, in which case, the maximum is located at $k^\star = 0$.

The adequacy of the harmonic framework is illustrated in Fig. 4.10. In the case $D = 2 \times 10^{-1}$, the harmonic response is able to emulate $\tilde{R}(k)$. Then, if the linear approximation holds, one expects that the estimates given by Eq. (4-19) should work. In fact, they do work in this case, as we will see below. Alternatively, when $D = 2 \times 10^{-4}$, $\tilde{R}(k)$ does not follow the harmonic shape, and the prediction of the decay length fails.

In Fig. 4.9, we compare the values of $\bar{k}$ and $\bar{x}$ extracted from the numerical solutions of Eq. (4-1), to those estimated by Eq. (4-19) (dashed lines) and, more accurately, to those predicted from the poles of $\tilde{R}(k)$ (solid lines), which perfectly follow the numerical results. The harmonic estimates are shown in the full abscissa ranges, as a reference, even in regions where the approximation is not expected to hold, because discrepancies give an idea of the departure from the harmonic or linear responses.

Figure 4.9c shows outcomes for a fixed $q < 0$ ($q = -0.5$), corresponding to a vertical cut in the diagram of Fig. 4.9a. Sustained oscillations (i.e., $\bar{x} \to 0$) can emerge for $q < 0$ when diffusion is weak, namely: for $D < D_c \simeq 0.0025$ (lilac colored region), where D_c is obtained from $\lambda(k^\star) = 0$. When D increases beyond this critical value, oscillations are damped with a finite characteristic length $\bar{x}$. For even larger values of D, oscillations completely disappear ($\bar{k} \to 0$).

Note that numerics and theory (symbols vs. lines) agree, close to the pattern transition point D_c, where the response peak is sharp (large Q). Despite the lack of accordance for a larger D, the theoretical prediction qualitatively works with a shift of transition to an exponential decay (dotted line).

[1] If $k_- < k_+$ are the points which $\tilde{R}(k_\pm) = \tilde{R}(k^\star)/2$. Then, $\Delta k/2 = (k_+ - k_-)/2$. If only k_+ exists, then we estimated $\Delta k/2 = k_+ - k^\star$.

Figure 4.9d (which corresponds to vertical cut at $q = 0.5$ in the diagram of Fig. 4.9a) shows the corresponding results for a fixed $q > 0$ ($q = 0.5$), which is characterized by the absence of sustained patterns. Above $D \simeq 0.02$, the response $\tilde{R}(k)$ is unimodal, a bell-shaped curve that resembles the harmonic response, as shown in Fig. 4.10, producing a good agreement between theory and numerical results, despite being far from the large-Q limit. However, for smaller values of D, the profile is multipeaked, compromising the use of the harmonic approximation. Besides that, the observed mode is wrongly predicted by $k^\star$, suggesting strong nonlinear effects. Even so, it is interesting that a detailed analysis of the response function still allows extracting the effective dominant mode, given by the position of its first small hump at $k \simeq 2.1$ representing a ghost dominant mode.

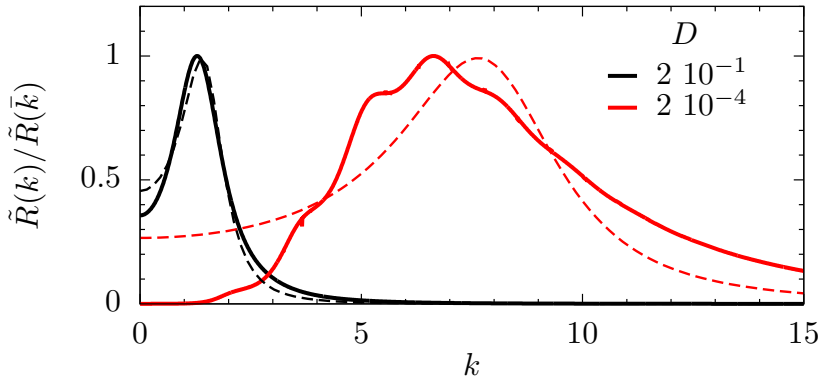

Figure 4.10: **Comparison of $\tilde{R}(k)$ with the harmonic response $\tilde{R}_H(k)$.** $\tilde{R}(k)$ of our model, given by Eq. (4-13) (solid lines) and harmonic response $R_H(k)$, given by Eq. (4-16) (dashed lines), where the values of k_0 and ζ were obtained by fitting Eq. (4-16) to $\tilde{R}(k)$. In all cases, $q = 0.5$, $\ell = 2$ and two different values of D shown on the legend were considered. Notice that, for $D = 2 \times 10^{-1}$, the response can be described by the harmonic approximation. For $D = 2 \times 10^{-4}$, the response is multipeaked, the harmonic approximation fails, and also the observed dominant mode is not given by the absolute maximum, but by the small hump at $k \simeq 2.1$, as predicted by the analysis of complex poles.

Figure 4.9b displays $\bar{k}$ and $\bar{x}$ as a function of q, for a fixed value of the diffusion coefficient ($D = 10^{-3}$), corresponding to a horizontal cut in Fig. 4.9a. Recall that the smaller the value of q, the more confined is the interaction (thus, the larger is $\bar{x}$). For $q < q_c \approx -0.093$, there are sustained oscillations ($\bar{x} \to \infty$). Above q_c, oscillations decay, which is indicated by the transition of $1/\bar{x}$ from null to finite values. Again, near this transition, the linear response prediction is good. Nevertheless, far from the critical point, it fails, as noticed

above $q \simeq 0.2$, where there is a strong mismatch between the main mode of the linear response analysis and the numerical one. Also, in this case, a small hump in the response function represents the dominant mode.

Finally, we do the same analysis for the influence function γ_α, and similar results are shown in Fig. 4.11. On panel b, we have results for a horizontal cut in $D = 10^{-3}$, where for $\alpha < \alpha_c \simeq 1.84$ ($2 - \alpha \simeq -0.16$), there are sustained oscillations.

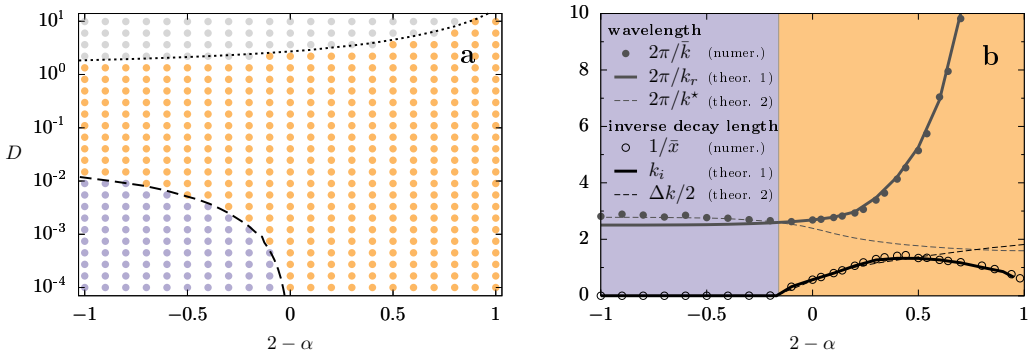

Figure 4.11: **Phase diagram and characteristics of the stationary profiles as a function of the shape parameter** $2 - \alpha$, for kernel $\gamma_\alpha(x)$ with $\ell = 2$. The remaining conditions and the conventions are the same as in Fig. 4.9.

4.4 Inferring information about the interactions

In this section, we extend the discussion about the mapping between kernel and the oscillation parameters, showing the way hidden information about the interactions can be extracted from landscape-induced oscillations.

In Sec. 4.3 we have shown how the interaction kernel determines the dominant wavelength $\bar{k}$ and the decay length $\bar{x}$. Now, we aim to show how, reciprocally, information about the interaction kernel can be extracted from the induced oscillations, assuming that the population dynamics is governed by the generalized FKPP equation, Eq. (4-1), with unknown kernel γ.

Using the theoretical estimates given by Eq. (4-19), within their validity range, we plot in Fig. 4.12a the contour lines for certain wavelengths $\bar{k}$ and decay lengths $\bar{x}$: $\bar{k}(\ell, q) =$ constant, and $\bar{x}(\ell, q) =$ constant. These contour lines depend both on ℓ and q. However, since $\bar{k}$ is strongly controlled by ℓ, while $\bar{x}$ is more closely related to the shape parameter q, there is a crossing of the lines that identifies the kernel properties. For comparison, we consider in Fig. 4.12b, the stretched-exponential kernel $\gamma_\alpha(x)$.

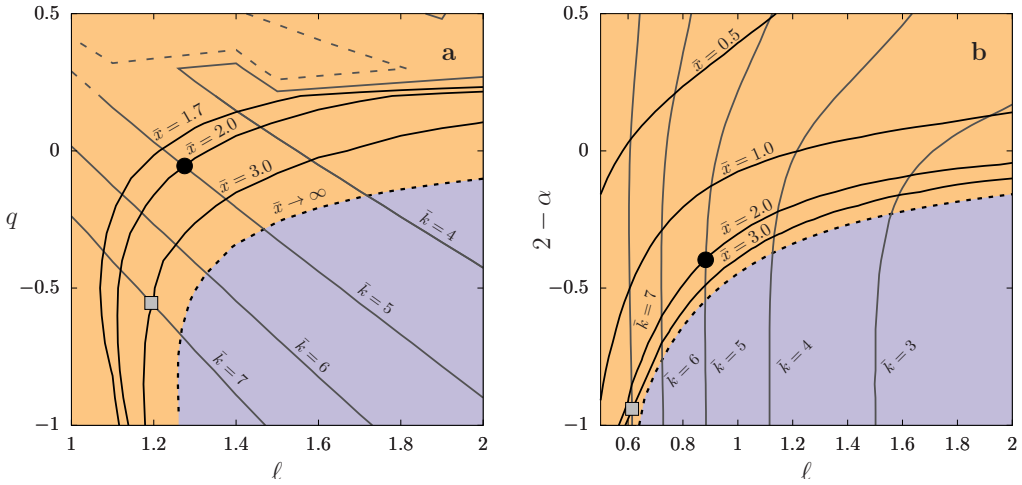

Figure 4.12: **Determination of the oscillation wave number, $\bar{k}$, and the decay length, $\bar{x}$.** Contour lines for the fixed wavelengths and the decay lengths. Colors for different oscillatory regimes as in previous figures. We considered interaction following kernel γ_q in (a) and γ_α in (b). The remaining parameters are $D = 10^{-3}$ and $a = b = 1$. Two points are highlighted: $(\bar{k}, \bar{x}) = (7, 3)$ (black circle) and (5,2) (gray square). Figure reprinted from [2]

Let us imagine that decay oscillations with specific values of $\bar{k}$ and $\bar{x}$ are observed (black circles and gray squares in Fig. 4.12). Then, assuming a particular kernel, we can extract the interaction length ℓ and the shape exponent β, from the $(\ell, \beta) \leftrightarrow (\bar{k}, \bar{x})$ mapping, where β represents either q or α.

Then, solving numerically the Eq. (4-1) with the parameters extracted, we obtain the oscillation shown in Fig. 4.13 (panel a for the black circles, panel b for the gray squares). However, since the information provided by the theory is limited, it is not possible to infer exactly which particular form of γ governs the dynamics just by measuring $(\bar{k}, \bar{x})$ of the oscillations.

Nevertheless, the characteristic length and compactness of the influence function can be accessed. In the insets of Fig. 4.13, we show the kernels which parameters have been extracted from the mapping of each point $(\bar{k}, \bar{x})$ of Fig. 4.12. Although one has finite support while the other has (stretched exponential) tails, both present similar coarse-grained appearance for given $(\bar{k}, \bar{x})$.

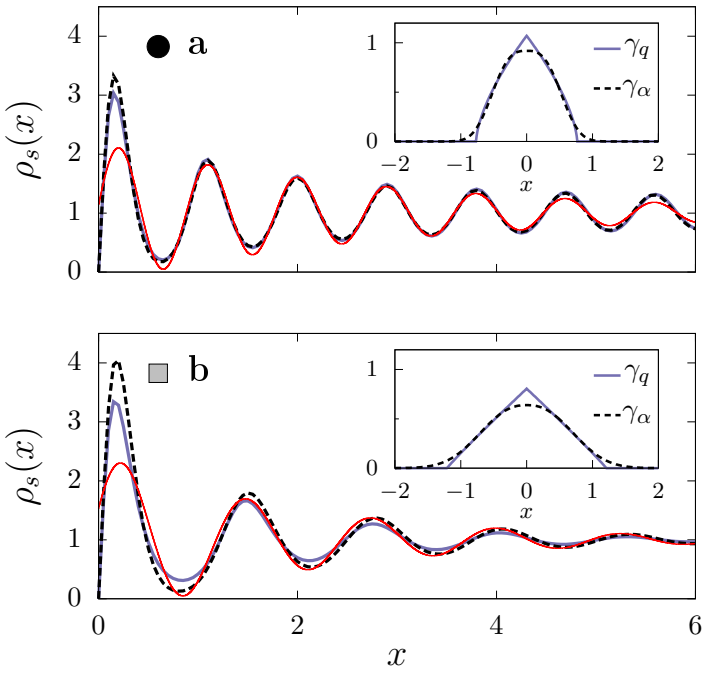

Figure 4.13: **Oscillations produced using parameters for the highlighted points in Fig. 4.12.** (a) $(\ell, q) = (1.19, -0.55)$, $(\ell, \alpha) = (0.61, 2.94)$ (black circle), and (b) $(\ell, q) = (1.275, -0.055)$, $(\ell, \alpha) = (0.883, 2.397)$ (gray square). The kernels γ_q (solid blue) and γ_α (dashed black) are shown in the respective insets. The red line shows a fit with mode $\bar{k}$ and decay $\bar{x}$, namely $\rho_H(x) = 1 + Be^{-x/\bar{x}} \sin(\bar{k}x + \phi)$, where B and ϕ were adjusted.

4.5 Comparison with experimental data

Natural situations, in which we can investigate the influence of heterogeneities in a population of a single species, are difficult to find. However, there are experiments, such as the one in Ref. [3], where the dynamics of non-chemotactic bacteria were investigated considering a refuge in a harmful context. More precisely, where external variation is controlled by an external heterogeneous UV-light field. Due to the simplicity of the organism, the Eq. (4-1) was considered a good candidate as a model. We observed that the density distribution obtained in the experiment reproduces the shape captured by our model in Fig. 4.1c, mainly, the peaks on the interface and the attenuated oscillations within the refuge.

In Fig. 4.14 we show the result of our simulation using the model given by Eq. (4-1). The spatial organization is qualitatively similar to the case experimentally investigated by Perry, although it needs to incorporate other elements for more realistic reproduction.

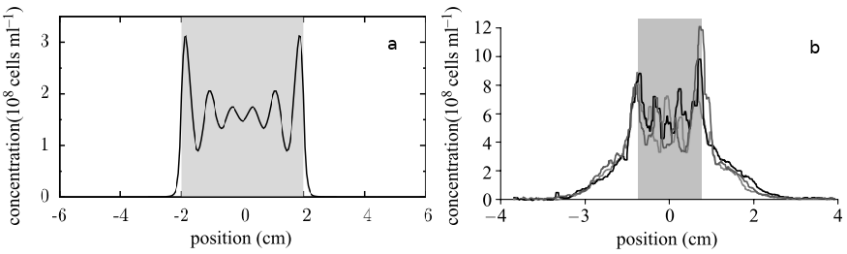

Figure 4.14: **Comparison with experimental data of patterns in a refuge.** a) Stationary patterns within a refuge in the center (gray region, $L = 4$), using influence function γ_q where $q = -0.8$ and $\ell = 2$. The other parameters are $D = 3 \times 10^{-3}$ and $A = 1$; b) Reprinted from Ref. [3].

4.6 Two-dimensional landscapes

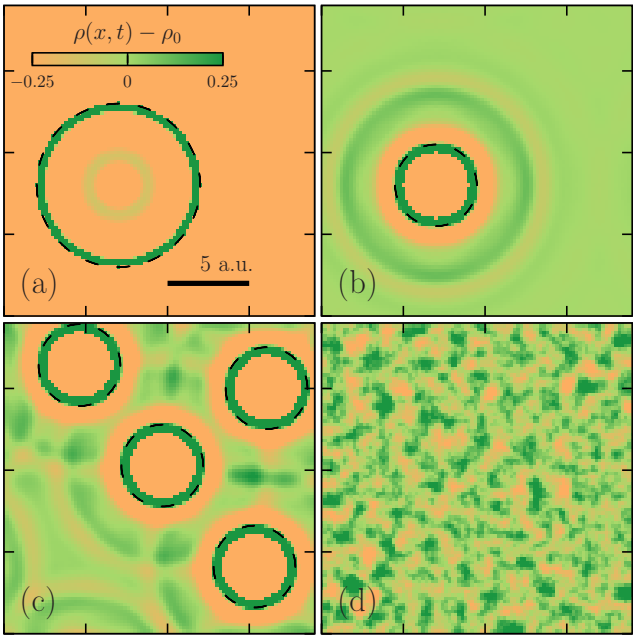

Figure 4.15: **Long-time spatial distribution in 2D.** Simulated scenarios: (a) a circular region (with radius 5 a.u., highlighted with a black dashed boundary) where the growth rate is positive a (in a strong negative background $a - A$); (b) a circular region (with radius 2.5 a.u., highlighted with a black dashed boundary) where the growth is strongly negative $a - A$ (while outside, it is positive, a); (c) four regions with negative growth rates $a - A$ (in a positive background, a); (d) random landscape with growth rates uniformly distributed in $[0.5a, 1.5a]$. In all cases, the interaction kernel is γ_q, with $\ell = 2$ and $q = 0.5$, $D = 10^{-3}$, $a = b = 1$ and $A = 10$. Colors show the deviation from the homogeneous state $\rho(x,t) - \rho_0$ (where $\rho_0 = 1$ for the chosen values of the parameters). For the numerical integration, a pseudo-spectral method was used with $\Delta x = 0.2$ and $\Delta t = 10^{-3}$. For details see Ref. [4]. Figure reprinted from [2].

In this section we show results of simulations for relevant 2D scenarios, verifying that the picture of induced oscillations described up to now for 1D also holds in 2D.

Snapshots of simulations for different 2D landscapes are presented in Fig. 4.15: a refuge (a), a defect (b), multiple defects (c) and spatial randomness (d) where a wide range of spatial scales are present [81, 87]. It is worth to remark that, in 2D, for the kernel γ_q, patterns only appear in homogeneous landscapes if $q < q_c \simeq 0.25$ (i.e., if $\lambda(k^\star) > 0$). Thus, in all the cases of Fig. 4.15 (using $q = 0.5$) we would not find oscillations if the landscape were homogeneous.

In Fig. 4.15, we see that, for 2D, the same picture as in 1D is found: the decaying oscillations appear near the landscape disturbances with a clear wavenumber and decay length. The linear response approach presented in this chapter can straightforwardly be extended to 2D.

Figure 4.15d shows a case where the landscape is random (in space, but time-independent). This situation, investigated in many previous studies [10, 81], produces a pattern that is noisy, but has a dominant wavelength, which is related to ℓ. Furthermore, although there is not a clear identification of the decay length from pattern observation, the linear theory would allow us to estimate the characteristic spatial correlation length from the width of the spectrum.

4.7 Concluding remarks

We have studied the non-local FKPP equation, which is a general modeling of nonlocally competing populations, in the presence of heterogeneous environments. We have identified three types of spatial structures close to a discontinuity of the environment: (i) *sustained oscillations*, (ii) *decaying oscillations*, and (iii) *exponential decay*. We have also shown that these structures, observed through the integration of the population dynamics Eq. (4-1), can be understood within a theoretical framework, as discussed in Sec. 4.2.2.

In the numerical examples, we have chosen to use the families γ_q and γ_α as interaction kernels, because it allows scanning shapes of different compactness. It is worth to remark that, due to the computational cost, our numerical study was carried out for 1D, but the same phenomenon also emerges in 2D environments, as shown in Sec. 4.6. The approach developed here can be straightforwardly extended to reach a broader ecological context.

The interesting point is that sharp heterogeneities reveal information on the interaction scales that are otherwise hidden. Then, the natural or artificial

interposition of an interface can act as a lens that allows seeing what is veiled in a homogeneous landscape. A closer look at this connection is shown in Sec. 4.4.

Finally, let us comment that our choice of sharp interfaces was motivated by the purpose of showing the emergence of essentially three simple classes of structures (i)-(iii), defined above. The single-interface case we analyze is particularly interesting because it puts into evidence the dominant wavenumber and the decay length.

In spite of that, this result is actually broader and can be used to understand the effects of arbitrary heterogeneous landscapes, such as the multiple and random cases shown in Fig. 4.15. It is noteworthy that similar structures emerge behind propagating fronts [10, 88].

Lastly, it is also interesting to remark that the reported results can reach contexts beyond population dynamics, since nonlocality is commonly found in complex systems.

5
Conclusions

The objective of this work is to show the role that the density-dependence mechanism and the heterogeneous environment have in the spatial organization of single-species populations. Population dynamics was mathematically modeled by the generalized Fisher-Kolmogorov-Petrovskii-Piskunov equation, that includes diffusion, growth and nonlocal neighborhood competition/interference through an integral kernel. This description is enough to describe patterns observed experimentally in bacterial colonies (for instance see Sec. 4.5).

Through computational and theoretical approaches, we investigated the shape of the stationary pattern, and we divided this work into two main parts, which correspond to different classes of environments where the individuals live:

– *Homogeneous landscape:* fragmentation is often attributed to landscape heterogeneity in literature, but we show that this kind of arrangement of individuals in space can emerge solely from their interactions.

  In our studies, we include nonlinearities in diffusion and reproduction rates to mimic density-dependent feedbacks. This takes into account the fact that the concentration of individuals can affect the rate of dispersion of the population (yielding subdiffusive and superdiffusive processes) due to the reaction to overcrowding and sparseness.

  Furthermore, concentration can also influence the growth rate, either spoiling or supporting an individual's reproduction. We determined a phase diagram in the space of parameters that characterize the nonlinearities, exhibiting the domains where patterns emerge.

  We also identify and classify different shapes of patterns: continuous, fragmented and peaked. Besides that, we discuss their implications for population stability and survival. We concluded that fragmentation is favored when growth and diffusion coefficients are positively correlated with population density; and when ν and μ are small, the diffusion and the per capita growth diverge at low densities, promoting fast occupation of unpopulated regions and thus, connecting clusters.

– *Heterogeneous landscape:* we investigated the spatial structures that emerge near defects associated with sharp spatial changes in the population growth rate.

We found that, depending on the influence function, three different profiles of the population density originate from the interface: sustained oscillations, decaying oscillations, and exponential decay towards a flat profile.

We provide theoretical predictions of the wavelength and the decay length of the induced wrinkles in population density based on mode linear stability analysis, in good accordance with numerical results.

Moreover, a more direct estimation is done on the light of the response function of a forced linear oscillator, which provides insights on the observed phenomenon. We found that, while the characteristic spatial scale of the kernel mainly regulates the mode of oscillation, its compactness regulates the decay-length.

Thus, within the decaying oscillation regime, there is information crossing between the oscillation metrics in the kernel parameter space. This allows access to hidden information about the underlying complex biological phenomena that mediate competitive interactions.

The robustness of these findings is tested through two generalized classes of influence functions and by investigating one- and two-dimensional landscapes. The theoretical framework takes a significant step in the direction of narrowing the connection between individual and population-level dynamics. Our findings provide new insights about the role of environmental heterogeneities in population spatial patterns.

6
Perspectives

From the research presented up to now, many scenarios can be studied to increase the scope of this work. For example, environmental conditions are not constant. Factors such as temperature, wind, humidity, nutrients, among others, can fluctuate over time. To include this phenomenon, a noise can be introduced in the control parameters. Furthermore, we might analyze other forms of density dependence in the parameters, as well as other forms of heterogeneity.

We are currently studying the case where the environment heterogeneity is reflected in a space-dependent diffusion coefficient. Below, we present the obtained results, which will be part of a future publication.

The system analyzed here consists of a population growing inside an L-size refuge, considering extreme conditions in which the population does not survive outside, i.e., $\rho(0,t) = \rho(L,t) = 0$. Within this refuge, the conditions of diffusion are not homogeneous. At first, we consider Stratonovich's formalism to describe diffusion, where the diffusive term is given by $\partial_x[\sqrt{D}\partial_x(\sqrt{D}\rho)]$. Later, it can be extended to other diffusivity formalisms, comparing its results.

As we are interested in analyzing how different diffusion coefficients $D(x)$ influence persistence of the population within the refuge, we will simplify the equation in order to have only the diffusive term and the growth term, as it follows

$$\partial_t \rho(x,t) = \partial_x \left[\sqrt{D(x)}\partial_x \left(\sqrt{D(x)}\rho(x,t)\right)\right] + a\rho(x,t). \tag{6-1}$$

If $D(x) = D_0$ is constant, the critical habitat size for the species' survival is [27]

$$L_c = \pi\sqrt{\frac{D_0}{a}}. \tag{6-2}$$

That is, if the size is $L > L_c$, the population goes extinct and, if $L < L_c$, the population grows indefinitely.

Two different forms of diffusion were chosen: diffusion varying with a power law, and a periodic diffusion following the cosine function. We solve numerically the Eq. (6-1) using the forward-time-centered-space (FTCS) second order scheme. The initial condition is $\rho_0(x) = 10^{-3} \pm \varepsilon(x)$, where $\varepsilon \in [-10^{-4}, 10^{-4}]$ is an uniformly distributed random perturbation. First, we consider a power law for diffusion. Afterwards, we will further explore

two possibilities, when diffusion is minimum $D_1(x)$ or maximum $D_2(x)$ in the center:

$$D_1^{pl}(x) = D_0 \left| \frac{x}{L/2} \right|^{\nu}, \tag{6-3}$$

$$D_2^{pl}(x) = D_0 \left[1 - \left| \frac{x}{L/2} \right|^{\nu} \right], \tag{6-4}$$

where the diffusion exponent ν is positive.

In Fig. 6.1, we present the diffusion as a function of x (on the left panel) and the population density in a refuge of size $L = 10$ (on the right panel) for different values of ν.

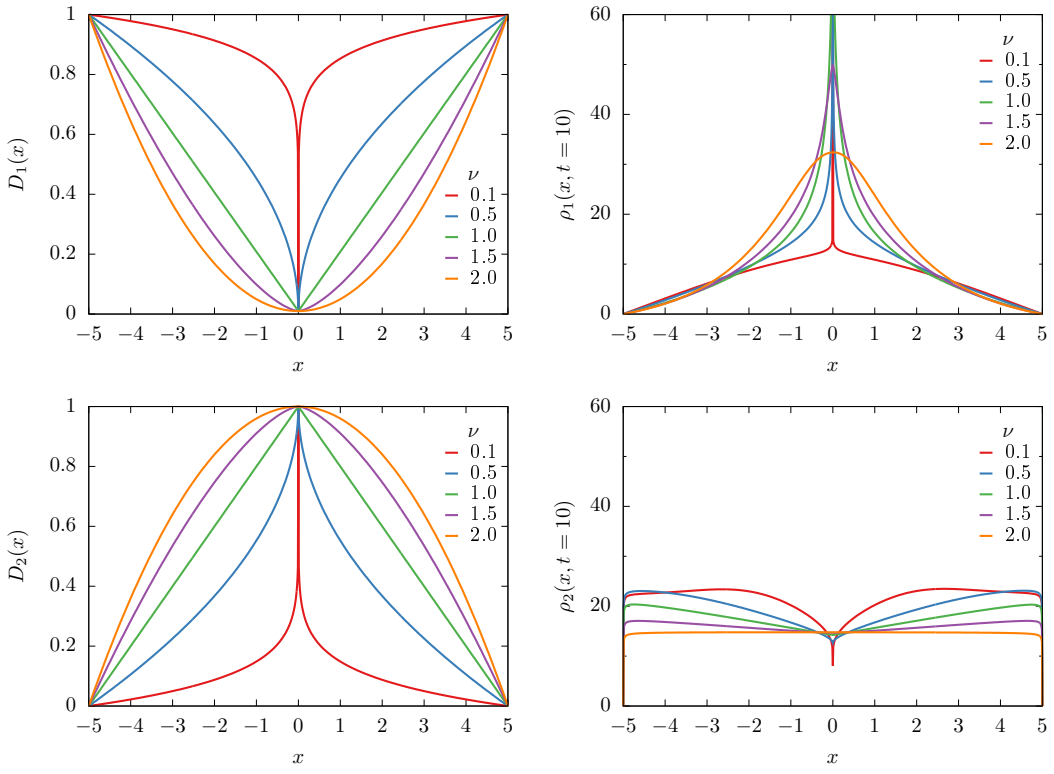

Figure 6.1: **Diffusion and their respective population density for different exponents of diffusion**. Upper panels: $D_1(x)$; and bottom panels:$D_2(x)$. On the left panels, the diffusion $D(x)$ given by Eq. (6-4) is represented, while on the right panels, the population density $\rho(x, t = 10)$ obtained by the numerical solution of Eq. (6-1) is represented. The parameters are $D_0 = 1$, $L = 10$, $a = 1$, and the value of ν is described on the legend.

The size of the refuge chosen in Fig. 6.1 is large enough for the population to survive. As Eq. (6-1) does not have the logistical term, which limits growth, the population grows exponentially and the density shown is not the stationary solution.

In Fig. 6.2, the temporal evolution of the population density for a specific value of ν is shown. On the left panel for diffusion $D_1(x)$ and on the right panel for diffusion $D_2(x)$.

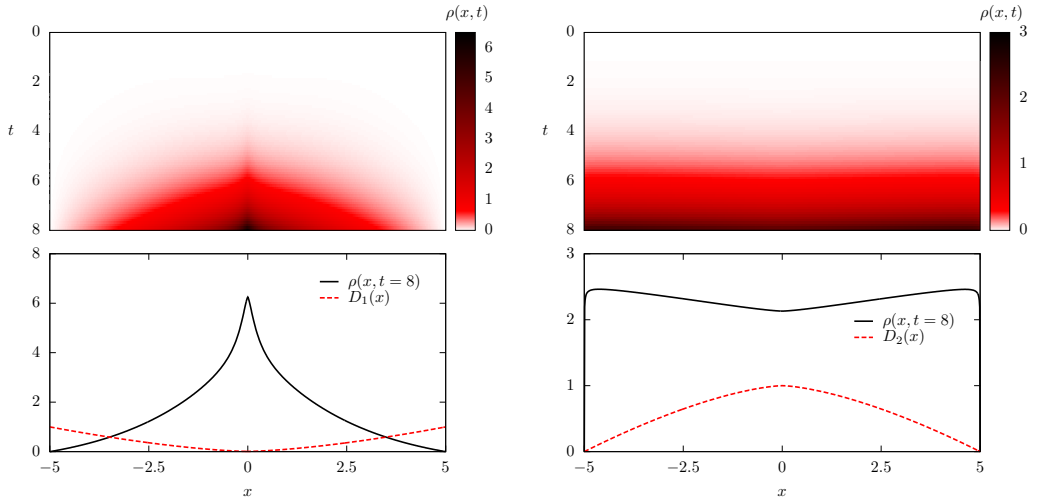

Figure 6.2: **Temporal evolution of the density** as a function of x for $\nu = 1.5$ and the same parameters of Fig. 6.1. Left: D_1 and Right: D_2.

A previous result is shown in Fig. 6.3, where we see how the exponent of the diffusion influences the critical size L_c of the refuge, obtained numerically.

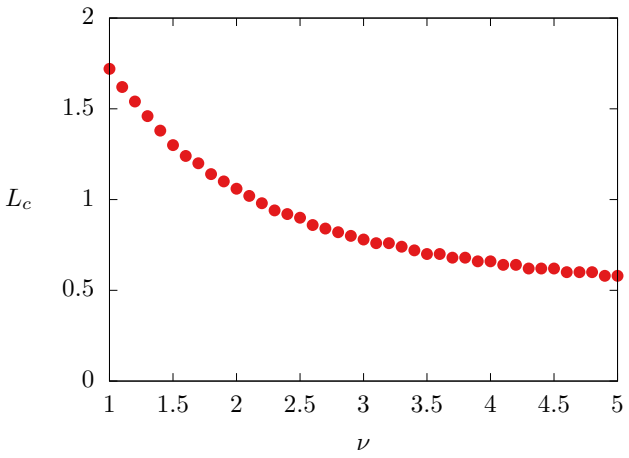

Figure 6.3: **The critical size of the refuge as a function of the diffusion exponent.** Obtained for $D_1(x)$ with $a = 1$.

The second expression for the diffusion coefficient for which we intend to study survival/extinction has an oscillatory behavior within the habitat, following a cosine type function, that is

$$D^p(x) = D_0 \left[1 + \alpha \cos\left(\frac{\beta\pi}{L}(x - x_0)\right)\right], \tag{6-5}$$

which temporal evolution and density behavior are shown in Fig. 6.4, for a particular case of parameters.

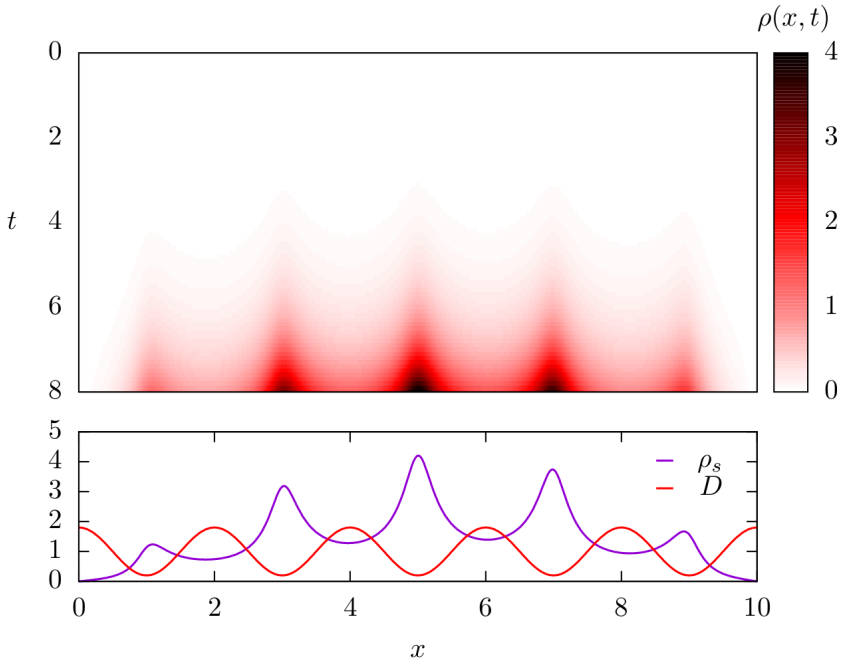

Figure 6.4: **Periodic diffusion: Temporal evolution of the density** as a function of x for $D_0 = 1$, $\alpha = 0.8$, $\beta = 10$, $x_0 = 0$, $a = 1$, and $L = 10$.

In summary, in this thesis, we describe the organization of single-species populations in homogeneous and heterogeneous environments. The material described in this chapter is just one example of how we can extend the scope of this study.

Furthermore, since nonlocality and anomalous diffusion are found in diverse complex systems, the impact of our results can go far beyond the context of population dynamics.

Bibliography references

[1] PRINGLE, R. M.; TARNITA, C. E.. **Spatial self-organization of ecosystems: Integrating multiple mechanisms of regular-pattern formation**. Annual Review of Entomology, 62(1):359–377, 2017. PMID: 28141964.

[2] DORNELAS, V.; COLOMBO, E. H.; LÓPEZ, C.; HERNÁNDEZ-GARCÍA, E. ; ANTENEODO, C.. **Landscape-induced spatial oscillations in population dynamics**. arXiv preprint arXiv:2003.00100, 2020.

[3] PERRY, N.. **Experimental validation of a critical domain size in reaction-diffusion systems with Escherichia coli populations**. Journal of the Royal Society, Interface, 2(4):379–387, Sep 2005.

[4] MONTAGNE, R.; HERNÁNDEZ-GARCÍA, E.; AMENGUAL, A. ; SAN MIGUEL, M.. **Wound-up phase turbulence in the complex Ginzburg-Landau equation**. Phys. Rev. E, 56:151–167, Jul 1997.

[5] HERNÁNDEZ-GARCÍA, E.; LÓPEZ, C.. **Clustering, advection, and patterns in a model of population dynamics with neighborhood-dependent rates**. Phys. Rev. E, 70:016216, Jul 2004.

[6] LUDWIG, D.; ARONSON, D. ; WEINBERGER, H.. **Spatial patterning of the spruce budworm**. Journal of Mathematical Biology, 8(3):217–258, 1979.

[7] COLOMBO, E. H.; ANTENEODO, C.. **Nonlinear diffusion effects on biological population spatial patterns**. Phys. Rev. E, 86:036215, Sep 2012.

[8] FUENTES, M. A.; KUPERMAN, M. N. ; KENKRE, V. M.. **Nonlocal Interaction Effects on Pattern Formation in Population Dynamics**. Physical Review Letters, 91(15):158104, Oct. 2003.

[9] KLAUSMEIER, C. A.. **Regular and Irregular Patterns in Semiarid Vegetation**. Science, 284(5421):1826–1828, June 1999.

[10] SASAKI, A.. **Clumped distribution by neighbourhood competition**. Journal of Theoretical Biology, 186(4):415–430, 1997.

[11] MARTÍNEZ-GARCÍA, R.; CALABRESE, J. M.; HERNÁNDEZ-GARCÍA, E. ; LÓPEZ, C.. **Minimal mechanisms for vegetation patterns in semiarid regions**. Phil. Trans. R. Soc. A, 372(2027):20140068, 2014.

[12] FERNANDEZ-OTO, C.; TZUK, O. ; MERON, E.. **Front instabilities can reverse desertification**. Physical Review Letters, 122(4):048101, 2019.

[13] WALKER, M.; HALL, A.; ANDERSON, R. M. ; BASÁÑEZ, M.-G.. **Density-dependent effects on the weight of female ascaris lumbricoides infections of humans and its impact on patterns of egg production**. Parasites & Vectors, 2:11–11, 2009.

[14] BIRZU, G.; MATIN, S.; HALLATSCHEK, O. ; KOROLEV, K.. **Genetic drift in range expansions is very sensitive to density feedback in dispersal and growth**. bioRxiv, 2019.

[15] HAKOYAMA, H.; IWASA, Y.. **Extinction risk of a density-dependent population estimated from a time series of population size**. Journal of Theoretical Biology, 204(3):337 – 359, 2000.

[16] BÄUERLE, T.; FISCHER, A.; SPECK, T. ; BECHINGER, C.. **Self-organization of active particles by quorum sensing rules**. Nature Communications, 9(1):3232, 2018.

[17] GIOMETTO, A.; ALTERMATT, F. ; RINALDO, A.. **Demographic stochasticity and resource autocorrelation control biological invasions in heterogeneous landscapes**. Oikos, 126(11):1554–1563, 2017.

[18] GIOMETTO, A.; ALTERMATT, F.; MARITAN, A.; STOCKER, R. ; RINALDO, A.. **Generalized receptor law governs phototaxis in the phytoplankton euglena gracilis**. Proceedings of the National Academy of Sciences of the United States of America, 112(22):7045–7050, 06 2015.

[19] HANSKI, I.; KUUSSAARI, M. ; NIEMINEN, M.. **Metapopulation structure and migration in the butterfly melitaea cinxia**. Ecology, 75(3):747–762, 1994.

[20] HANSKI, I.. **Metapopulation Ecology**. Oxford series in ecology and evolution. Oxford University Press, 1999.

[21] KEYMER, J. E.; MARQUET, P. A.; VELASCO-HERNÁNDEZ, J. X. ; LEVIN, S. A.. **Extinction thresholds and metapopulation persistence in dynamic landscapes**. The American Naturalist, 156(5):478–494, 2000.

[22] PERRY, N.. **Experimental validation of a critical domain size in reaction–diffusion systems with escherichia coli populations**. Journal of The Royal Society Interface, 2(4):379–387, 2005.

[23] KENKRE, V. M.; KUMAR, N.. **Nonlinearity in bacterial population dynamics: Proposal for experiments for the observation of abrupt transitions in patches**. Proceedings of the National Academy of Sciences, 105(48):18752–18757, 2008.

[24] SEDDON, P. J.; ARMSTRONG, D. P. ; MALONEY, R. F.. **Developing the science of reintroduction biology**. Conservation Biology, 21(2):303–312, 2007.

[25] KÖNIG, S.; WORRICH, A.; BANITZ, T.; CENTLER, F.; HARMS, H.; KÄSTNER, M.; MILTNER, A.; WICK, L. Y.; THULLNER, M. ; FRANK, K.. **Spatiotemporal disturbance characteristics determine functional stability and collapse risk of simulated microbial ecosystems**. Scientific reports, 8(1):9488–9488, Jun 2018. 29934540[pmid].

[26] RYABOV, A. B.; BLASIUS, B.. **Population growth and persistence in a heterogeneous environment: the role of diffusion and advection**. Mathematical Modelling of Natural Phenomena, 3:42–86, 1 2008.

[27] COLOMBO, E.; ANTENEODO, C.. **Nonlinear population dynamics in a bounded habitat**. Journal of Theoretical Biology, 446:11 – 18, 2018.

[28] FISHER, R.. **The Wave of Advance of Advantageous Genes.** Annals of Eugenics, 7:355–369, 1937.

[29] KOLMOGOROV, A. N.; PETROVSKII, I. ; PISKUNOV, N.. **Study of a diffusion equation that is related to the growth of a quality of matter and its application to a biological problem**. Moscow University Mathematics Bulletin, 1:1–26, 1937.

[30] CENCINI, M.; LOPEZ, C. ; VERGNI, D.. **Reaction-Diffusion Systems: Front Propagation and Spatial Structures**, p. 187–210. Springer Berlin Heidelberg, Berlin, Heidelberg, 2003.

[31] BIALEK, W.; CAVAGNA, A.; GIARDINA, I.; MORA, T.; SILVESTRI, E.; VIALE, M. ; WALCZAK, A. M.. **Statistical mechanics for natural flocks of birds**. Proceedings of the National Academy of Sciences, 109(13):4786–4791, 2012.

[32] WARD, A. J. W.; SUMPTER, D. J. T.; COUZIN, I. D.; HART, P. J. B. ; KRAUSE, J.. **Quorum decision-making facilitates information transfer in fish shoals**. Proceedings of the National Academy of Sciences, 105(19):6948–6953, 2008.

[33] CASTELLANO, C.; FORTUNATO, S. ; LORETO, V.. **Statistical physics of social dynamics**. Rev. Mod. Phys., 81:591–646, May 2009.

[34] BEN-JACOB, E.; SCHOCHET, O.; TENENBAUM, A.; COHEN, I.; CZIROK, A. ; VICSEK, T.. **Generic modelling of cooperative growth patterns in bacterial colonies**. Nature, 368(6466):46–49, 1994.

[35] RUDGE, T. J.; FEDERICI, F.; STEINER, P. J.; KAN, A. ; HASELOFF, J.. **Cell polarity-driven instability generates self-organized, fractal patterning of cell layers**. ACS Synthetic Biology, 2(12):705–714, 2013.

[36] MURRAY, J. D.. **Mathematical Biology: I. An Introduction**. Interdisciplinary Applied Mathematics. Springer, 2002.

[37] MARTÍNEZ-GARCÍA, R.; CALABRESE, J. M.; HERNÁNDEZ-GARCÍA, E. ; LÓPEZ, C.. **Vegetation pattern formation in semiarid systems without facilitative mechanisms**. Geophysical Research Letters, 40(23):6143–6147, 2013.

[38] TARNITA, C. E.; BONACHELA, J. A.; SHEFFER, E.; GUYTON, J. A.; COVERDALE, T. C.; LONG, R. A. ; PRINGLE, R. M.. **A theoretical foundation for multi-scale regular vegetation patterns**. Nature, 541(7637):398, 2017.

[39] FERNANDEZ-OTO, C.; CLERC, M. G.; ESCAFF, D. ; TLIDI, M.. **Strong nonlocal coupling stabilizes localized structures: An analysis based on front dynamics**. Phys. Rev. Lett., 110:174101, Apr 2013.

[40] LIU, J.; MARTINEZ-CORRAL, R.; PRINDLE, A.; LEE, D.-Y. D.; LARKIN, J.; GABALDA-SAGARRA, M.; GARCIA-OJALVO, J. ; SÜEL, G. M.. **Coupling between distant biofilms and emergence of nutrient time-sharing**. Science, 356(6338):638–642, 2017.

[41] DA CUNHA, J. A. R.; PENNA, A. L. A. ; OLIVEIRA, F. A.. **Pattern formation and coexistence domains for a nonlocal population dynamics**. Physical Review E, 83(1):15201, Jan. 2011.

[42] SOSA-HERNÁNDEZ, J. E.; SANTILLÁN, M. ; SANTANA-SOLANO, J.. **Motility of escherichia coli in a quasi-two-dimensional porous medium**. Phys. Rev. E, 95:032404, Mar 2017.

[43] MUSKAT, M.; WYCKOFF, R. D. ; OTHERS. **Flow of homogeneous fluids through porous media**. McGraw-Hill Book Company, Inc., 1937.

[44] CATES, M. E.; MARENDUZZO, D.; PAGONABARRAGA, I. ; TAILLEUR, J.. **Arrested phase separation in reproducing bacteria creates a generic route to pattern formation**. Proceedings of the National Academy of Sciences, 107(26):11715–11720, 2010.

[45] NEWMAN, W. I.. **Some exact solutions to a non-linear diffusion problem in population genetics and combustion**. Journal of Theoretical Biology, 85(2):325 – 334, 1980.

[46] GURTIN, M. E.; MACCAMY, R. C.. **On the diffusion of biological populations**. Mathematical Biosciences, 33(1):35 – 49, 1977.

[47] KAREIVA, P.. **Local movement in herbivorous insects: applying a passive diffusion model to mark-recapture field experiments**. Oecologia, 57(3):322–327, 1983.

[48] TSALLIS, C.; BUKMAN, D. J.. **Anomalous diffusion in the presence of external forces: Exact time-dependent solutions and their thermostatistical basis**. Physical Review E, 54(3):R2197–R2200, Sept. 1996.

[49] FUENTES, M. A.; KUPERMAN, M. N. ; KENKRE, V. M.. **Nonlocal interaction effects on pattern formation in population dynamics**. Phys. Rev. Lett., 91:158104, Oct 2003.

[50] HERNÁNDEZ-GARCÍA, E.; LÓPEZ, C.. **Clustering, advection, and patterns in a model of population dynamics with neighborhood-dependent rates**. Phys. Rev. E, 70:016216, Jul 2004.

[51] LÓPEZ, C.; HERNÁNDEZ-GARCÍA, E.. **Fluctuations impact on a pattern-forming model of population dynamics with non-local interactions**. Physica D: Nonlinear Phenomena, 199(1):223 – 234, 2004.

[52] PIGOLOTTI, S.; LÓPEZ, C. ; HERNÁNDEZ-GARCÍA, E.. **Species clustering in competitive Lotka-Volterra models**. Phys. Rev. Lett., 98:258101, Jun 2007.

[53] COLOMBO, E. H.; ANTENEODO, C.. **Nonlinear diffusion effects on biological population spatial patterns**. Physical Review E, 86(3):036215, 2012.

[54] PIGOLOTTI, S.; LÓPEZ, C.; HERNÁNDEZ-GARCÍA, E. ; ANDERSEN, K. H.. **How gaussian competition leads to lumpy or uniform species distributions**. Theoretical Ecology, 3(2):89–96, 2010.

[55] BARBOSA, F. V.; PENNA, A. A.; FERREIRA, R. M.; NOVAIS, K. L.; DA CUNHA, J. A. ; OLIVEIRA, F. A.. **Pattern transitions and complexity for a nonlocal logistic map**. Physica A: Statistical Mechanics and its Applications, 473:301–312, 2017.

[56] PRESS, W. H.; TEUKOLSKY, S. A.; VETTERLING, W. T. ; FLANNERY, B. P.. **Numerical recipes in C**, volumen 2. Cambridge university press Cambridge, 1996.

[57] BAPTESTINI, E. M.; DE AGUIAR, M. A. ; BAR-YAM, Y.. **Conditions for neutral speciation via isolation by distance**. Journal of Theoretical Biology, 335:51 – 56, 2013.

[58] TURNER, M. G.; GARDNER, R. H.; O'NEILL, R. V. ; OTHERS. **Landscape ecology in theory and practice**. Springer, 2001.

[59] LEVIN, S. A.. **Dispersion and population interactions**. The American Naturalist, 108(960):207–228, 1974.

[60] FAHRIG, L.. **Effects of habitat fragmentation on biodiversity**. Annual review of ecology, evolution, and systematics, 34(1):487–515, 2003.

[61] BLANCHARD, A. E.; LU, T.. **Bacterial social interactions drive the emergence of differential spatial colony structures**. BMC Systems Biology, 9(1):59, Sep 2015.

[62] NADELL, C. D.; FOSTER, K. R. ; XAVIER, J. B.. **Emergence of spatial structure in cell groups and the evolution of cooperation**. PLOS Computational Biology, 6(3):1–9, 03 2010.

[63] HALLATSCHEK, O.; HERSEN, P.; RAMANATHAN, S. ; NELSON, D. R.. **Genetic drift at expanding frontiers promotes gene segregation**. Proceedings of the National Academy of Sciences, 104(50):19926–19930, 2007.

[64] KREFT, J.-U.. **Biofilms promote altruism**. Microbiology, 150(8):2751–2760, 2004.

[65] PIGOLOTTI, S.; BENZI, R.; JENSEN, M. H. ; NELSON, D. R.. **Population genetics in compressible flows**. Phys. Rev. Lett., 108:128102, Mar 2012.

[66] DORNELAS, V.; COLOMBO, E. H. ; ANTENEODO, C.. **Single-species fragmentation: The role of density-dependent feedback**. Phys. Rev. E, 99:062225, Jun 2019.

[67] LENZI, E.; ANTENEODO, C. ; BORLAND, L.. **Escape time in anomalous diffusive media**. Physical Review E, 63(5):051109, 2001.

[68] ANTENEODO, C.. **Brownian motors in nonlinear diffusive media**. Physical Review E, 76(2):021102, 2007.

[69] ANTENEODO, C.. **Non-extensive random walks**. Physica A: Statistical Mechanics and its Applications, 358(2):289 – 298, 2005.

[70] TRONCOSO, P.; FIERRO, O.; CURILEF, S. ; PLASTINO, A.. **A family of evolution equations with nonlinear diffusion, verhulst growth, and global regulation: Exact time-dependent solutions**. Physica A: Statistical Mechanics and its Applications, 375(2):457 – 466, 2007.

[71] TSALLIS, C.. **Introduction to nonextensive statistical mechanics: approaching a complex world**. Springer Science and Business Media, 2009.

[72] HERNÁNDEZ-GARCÍA, E.; LÓPEZ, C.; PIGOLOTTI, S. ; ANDERSEN, K. H.. **Species competition: coexistence, exclusion and clustering**. Philosophical Transactions of the Royal Society A: Mathematical, Physical and Engineering Sciences, 367(1901):3183–3195, 2009.

[73] ANTENEODO, C.. **Non-extensive random walks**. Physica A: Statistical Mechanics and its Applications, 358(2-4):289–298, 2005.

[74] FERNANDEZ-OTO, C.; TLIDI, M.; ESCAFF, D. ; CLERC, M.. **Strong interaction between plants induces circular barren patches: fairy circles**. Philosophical Transactions of the Royal Society A: Mathematical, Physical and Engineering Sciences, 372(2027):20140009, 2014.

[75] MARTÍNEZ-GARCÍA, R.; CALABRESE, J. M.; HERNÁNDEZ-GARCÍA, E. ; LÓPEZ, C.. **Minimal mechanisms for vegetation patterns in semiarid regions**. Phil. Trans. R. Soc. A, 372(2027):20140068, 2014.

[76] VAN DE KOPPEL, J.; GASCOIGNE, J. C.; THERAULAZ, G.; RIETKERK, M.; MOOIJ, W. M. ; HERMAN, P. M.. **Experimental evidence for spatial self-organization and its emergent effects in mussel bed ecosystems**. science, 322(5902):739–742, 2008.

[77] RUIZ-REYNÉS, D.; GOMILA, D.; SINTES, T.; HERNÁNDEZ-GARCÍA, E.; MARBÀ, N. ; DUARTE, C. M.. **Fairy circle landscapes under the sea**. Science advances, 3(8):e1603262, 2017.

[78] ESCAFF, D.; FERNANDEZ-OTO, C.; CLERC, M. G. ; TLIDI, M.. **Localized vegetation patterns, fairy circles, and localized patches in arid landscapes**. Phys. Rev. E, 91:022924, Feb 2015.

[79] RIOU, J.; ALTHAUS, C. L.. **Pattern of early human-to-human transmission of wuhan 2019 novel coronavirus (2019-ncov), december 2019 to january 2020**. Eurosurveillance, 25(4), 2020.

[80] BERTI, S.; CENCINI, M.; VERGNI, D. ; VULPIANI, A.. **Extinction dynamics of a discrete population in an oasis**. Phys. Rev. E, 92:012722, Jul 2015.

[81] RIDOLFI, L.; D'ODORICO, P. ; LAIO, F.. **Noise-Induced Phenomena in the Environmental Sciences**. Cambridge University Press, 2011.

[82] COLOMBO, E. H.; ANTENEODO, C.. **Metapopulation dynamics in a complex ecological landscape**. Phys. Rev. E, 92:022714, Aug 2015.

[83] DA SILVA, L. A.; COLOMBO, E. H. ; ANTENEODO, C.. **Effect of environment fluctuations on pattern formation of single species**. Phys. Rev. E, 90:012813, Jul 2014.

[84] FONSECA, C. R.; COUTINHO, R. M.; AZEVEDO, F.; BERBERT, J. M.; CORSO, G. ; KRAENKEL, R. A.. **Modeling habitat split: Landscape and life history traits determine amphibian extinction thresholds**. PLOS ONE, 8(6):1–7, 06 2013.

[85] TSALLIS, C.. **Introduction to nonextensive statistical mechanics: approaching a complex world**. Springer Science & Business Media, 2009.

[86] BUTIKOV, E. I.. **Square-wave excitation of a linear oscillator**. American Journal of Physics, 72(4):469–476, 2004.

[87] GARCÍA-OJALVO, J.; SANCHO, J.. **Noise in spatially extended systems**. Springer Science & Business Media, 2012.

[88] GANAN, Y. A.; KESSLER, D. A.. **Front propagation and clustering in the stochastic nonlocal Fisher equation**. Physical Review E, 97(4):042213, 2018.

A
Influence functions of non-local competition

The mathematical model used in this work, Eq. (2-5), takes into account that individuals in the population compete for resources with all neighbors within an ℓ distance, and this interaction is mediated by an influence function $\gamma(x)$. When the range of competitive interaction between individuals is too short $\ell \to 0$, this corresponds to well-located delta distribution function,

$$\gamma_{\ell\to 0}(x - x') = \delta(x - x'), \tag{A-1}$$

and the competitive term is described by $-b\rho^2(x,t)$. In this case, we recover the original FKPP equation described by the Eq. (2-1), and the stationary profile is homogeneous, i.e., there are not patterns.

In Table A.1, we collect the influence functions presented during the work and their respective Fourier transform.

Top-hat	$\gamma_h(x) = \frac{1}{2\ell}\Theta(\ell - \lvert x\rvert)$	$\tilde{\gamma}_h(k) = \frac{\sin(k\ell)}{k\ell}$
q-exponential	$\gamma_q(x) = \frac{2-q}{2\ell}[1-(1-q)\lvert x\rvert/\ell]_+^{1/(1-q)}$	–
$q \to -\infty$ (Top-hat)	$\gamma_{\text{-}\infty}(x) = \frac{1}{2\ell}\Theta(\ell - \lvert x\rvert)$	$\tilde{\gamma}_{\text{-}\infty}(k) = \frac{\sin(k\ell)}{k\ell}$
$q = 0$ (Triangular)	$\gamma_0(x) = \frac{1}{\ell}[1 - \lvert x\rvert/\ell]_+$	$\tilde{\gamma}_0(k) = \frac{\sin^2(k\ell)}{(k\ell)^2}$
$q = 1$ (Exponential)	$\gamma_1(x) = \frac{1}{2\ell}e^{-\lvert x\rvert/\ell}$	$\tilde{\gamma}_1(k) = \frac{1}{1+(k\ell)^2}$
Stretched exponential	$\gamma_\alpha(x) = \frac{e^{-(\lvert x\rvert/\ell)^\alpha}}{2\ell\,\Gamma(1+1/\alpha)}$	–
$\alpha = 1$ (Exponential)	$\gamma_1(x) = \frac{1}{2\ell}e^{-\lvert x\rvert/\ell}$	$\tilde{\gamma}_1(k) = \frac{1}{1+(k\ell)^2}$
$\alpha = 2$ (Gaussian)	$\gamma_2(x) = \frac{1}{\sqrt{\pi}\ell}e^{-(\lvert x\rvert/\ell)^2}$	$\tilde{\gamma}_2(k) = e^{-(k\ell)^2/4}$
$\alpha \to \infty$ (Top-hat)	$\gamma_\infty(x) = \frac{1}{2\ell}\Theta(\ell - \lvert x\rvert)$	$\tilde{\gamma}_\infty(k) = \frac{\sin(k\ell)}{k\ell}$

Table A.1: **Summary of the influence function adopted throughout the work,** and some particular cases in which there is an exact Fourier transform. When $q \to -\infty$, we made the change $\ell \to \ell(1-q)$.

In Fig. A.1, we can observe, in the left panel, the influence kernel, and, in the right panel, the mode growth rate (Eq. (2-9) presented in the Chap. 2) for three functions defined in the Tab. A.1.

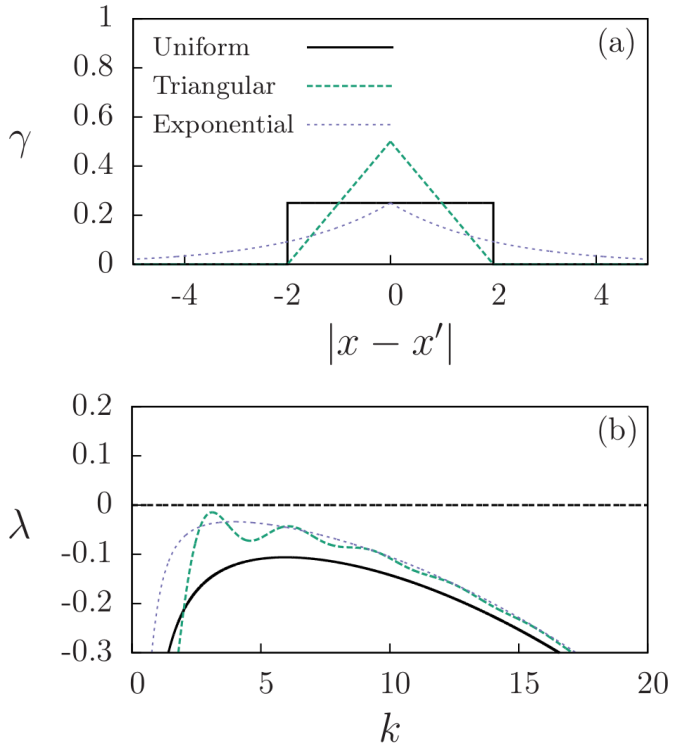

Figure A.1: **Interaction kernel and mode growth rate.** (a) Interaction profiles γ for the uniform, triangular, and exponential kernels with $\ell = 2$ (see Table A.1), and (b) mode growth rate $\lambda(k)$, where the parameters used are $D = 10^{-3}$, $\nu = \mu = 1$, and $\rho_0 = 1$.

For the particular cases where there is no exact expression for the Fourier transform $\tilde{\gamma}(k)$ (see Table A.1), we need to find numerically the value of the mode stability $\lambda(k)$.

In Fig. A.2, we present a direct comparison between the results of the two families of influence functions used in Chap. 4, γ_q and γ_α. We can observe the interaction kernel, its respective mode growth rates. Remembering that, when $q \leq -0.093$, the profile shows sustained oscillation for $D = 10^{-3}$ (see Fig. 4.9b). The same occurs when $\alpha \geq 2.16$ and $D = 10^{-3}$ (see Fig. 4.11b).

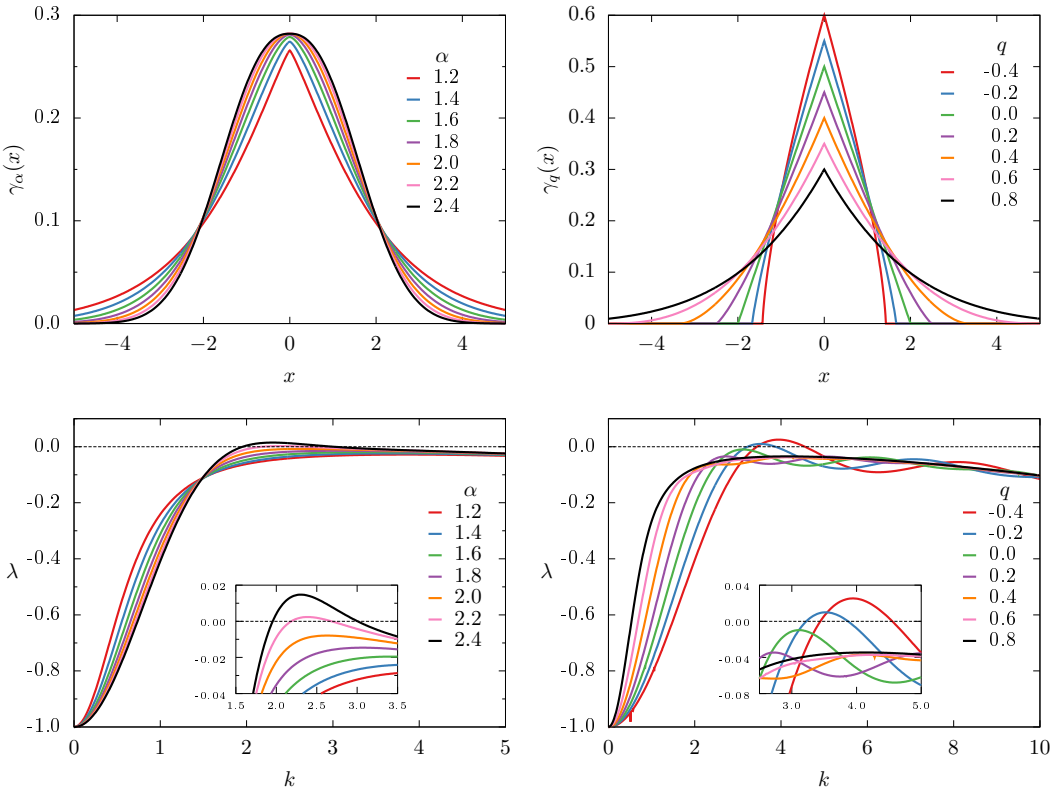

Figure A.2: **Comparison between the two families of influence functions and their respective mode growth rate,** using $\ell = 2$ and $D = 10^{-3}$. Left: Results for γ_α. Right: Results for γ_q.

In Figs. A.3, A.4 and A.5, we present the maximal value of the mode growth rate and profiles of mode growth rate.

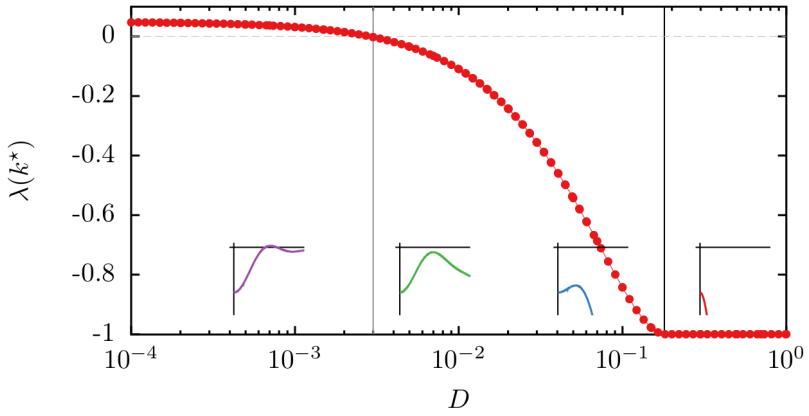

Figure A.3: **Maximal value of the mode growth rate as a function of D with $q = -0.5$, and profiles of mode growth rate $\lambda(k)$.** The vertical lines indicate the values of D above which (i) the maximal value of λ becomes negative ($D \simeq 0.003$), and (ii) this maximum becomes located at $k = 0$ ($D \simeq 0.18$).

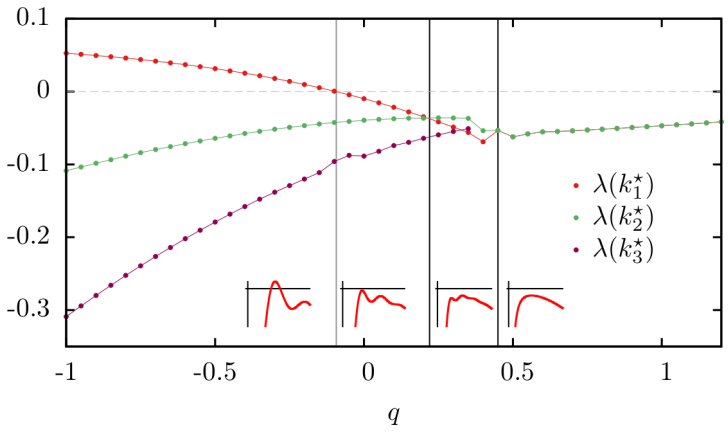

Figure A.4: **Maximal value of the mode growth rate as a function of q with $D = 10^{-3}$, and profiles of mode growth rate $\lambda(k)$.** The $k_i^\star$ represent the i-th local maximum. The vertical lines indicate the values of q above which (i) the maximum value of λ becomes negative ($q \simeq -0.093$), (ii) the second peak becomes the global maximum of the dispersion ratio ($q \simeq 0.21$) and (iii) the dispersion ratio stops oscillating ($q \simeq 0.45$).

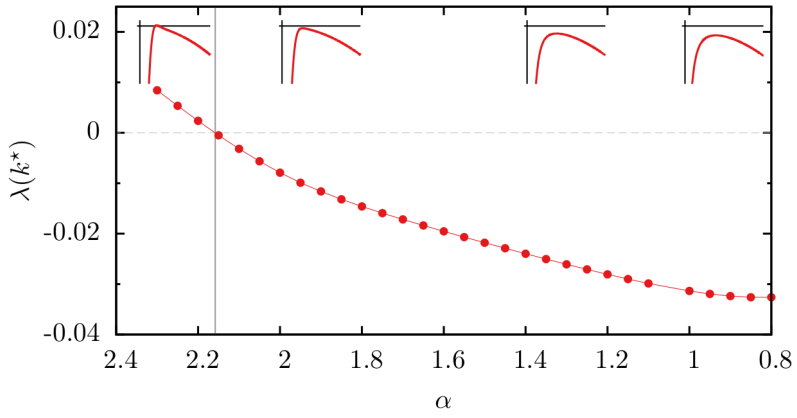

Figure A.5: **Maximal value of the mode growth rate as a function of α with $D = 10^{-3}$, and profiles of mode growth rate $\lambda(k)$.** The vertical line represents $\alpha \simeq 2.16$, at which $\lambda(k^\star) = 0$.

B
Complementary results for heterogeneity

In this appendix, we present complementary results for the population within a refuge (Section 4.2.1).

Weak heterogeneity

In Fig. B.1, we show numerical results for the stationary patterns of the kernels shown in Fig. A.1, for different values of D. As we increase the diffusion coefficient D, oscillations are more damped. Notice that the uniform kernel (top-hat) is the one that promotes more oscillatory profiles.

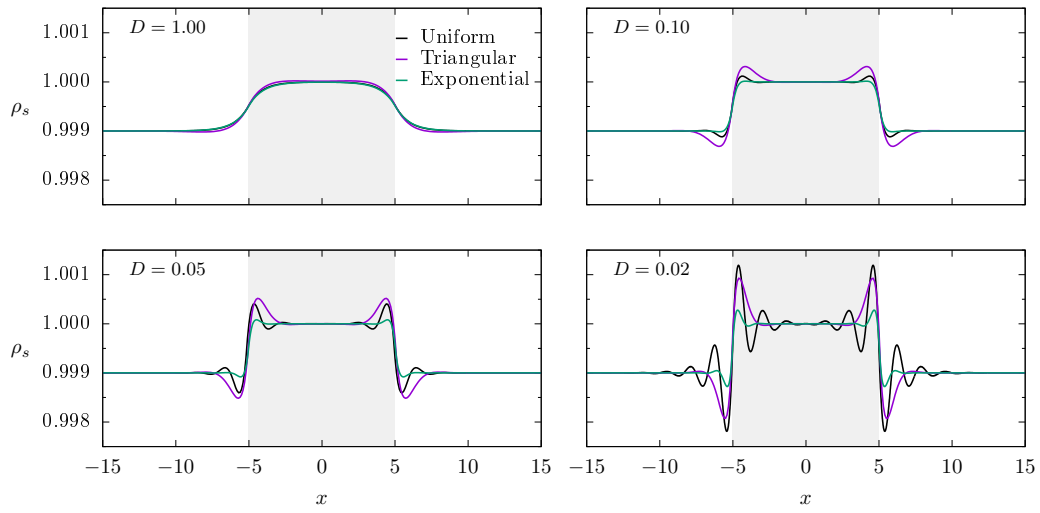

Figure B.1: **Comparison of profiles for different influence functions with $\ell = 1$.** Stationary population density as a function of x obtained from numerical integration of Eq. (4-1) , for different values of D and $L = 10$. We use $A = 10^{-3}$, so the growth rate outside of the mask is negative ($A - a = 0.999$). The gray region correspond to the refuge.

In Fig. B.2 we present comparisons between analytical (Eq. 4-9) and numerical (Eq. 4-1) solutions for the population density distribution. For the particular cases where there is no exact expression for the Fourier transform $\tilde{\gamma}(k)$(see table), we need to find numerically the value of the mode stability $\lambda(k)$.

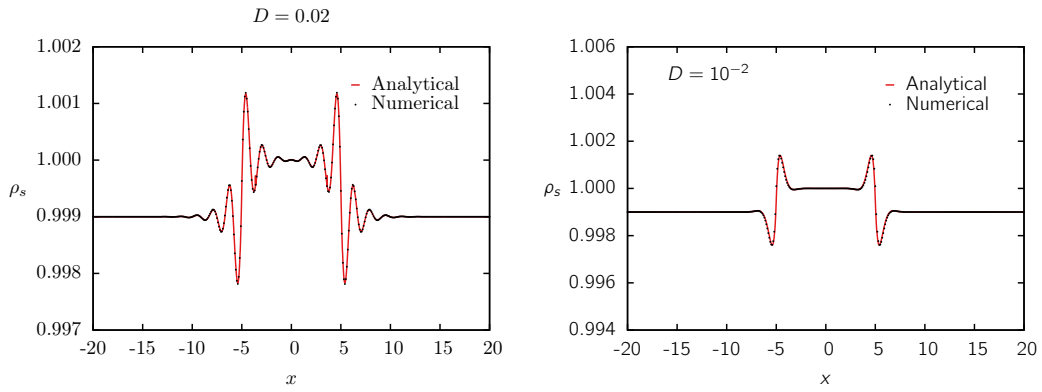

Figure B.2: **Comparisons between analytical and numerical results. Left: Top-hat kernel; Right: Exponential kernel.** Steady population density as a function of x obtained numerically from Eq. (4-1), and analytically from Eq. (4-9), for $L = 10$, $\ell = 1$, $A = 10^{-3}$, and D described in the figure.

Strong heterogeneity

In Fig. B.3, we present the patterns within a refuge (with zero growth rate outside), for the same kernels presented in Fig. A.2.

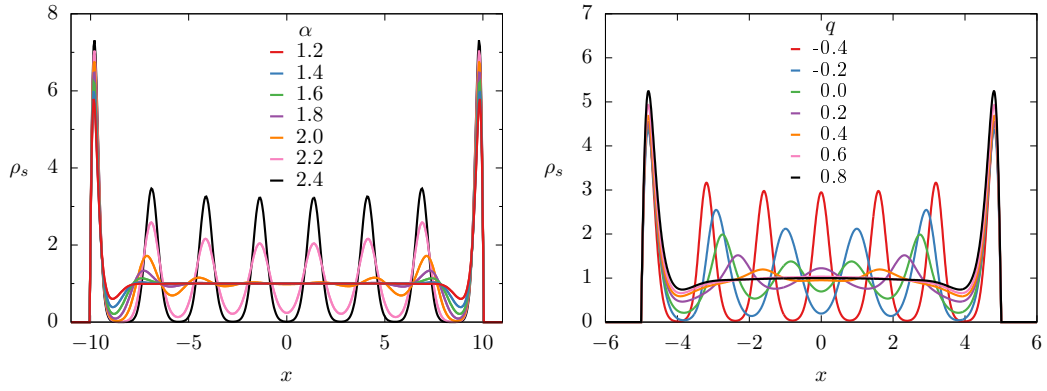

Figure B.3: **Comparison between the patterns of the two families of influence functions.** Left: population density using the γ_α kernel inside a refuge of size $L = 20$. Right: population density using the γ_q kernel inside a refuge of size $L = 10$. The others parameters are $\ell = 2$ and $D = 10^{-3}$.

Critical refuge size

For $A > a$, the population outside the refuge goes to zero, since the growth rate is negative there. Inside the refuge the profiles are almost insensitive to $A > a$, mainly for decreasing D.

Furthermore, a critical refuge size for population survival emerges [27],

$$L_c = 2\sqrt{D/a}\arctan\sqrt{(A-a)/a}\,. \tag{B-1}$$

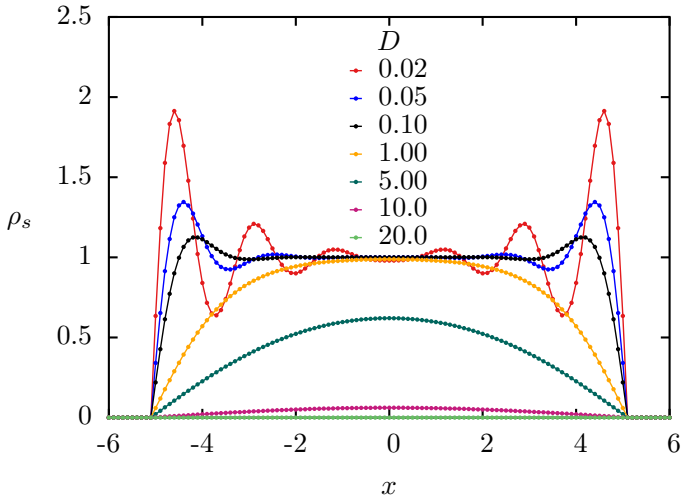

Figure B.4: **Uniform influence function γ_h, with $\ell = 1$.** The steady population density as a function of x obtained numerically from Eq. (2-5), for different values of D. In this case $D_c \simeq 10.1$, then the populations goes extinct when $D = 20$.

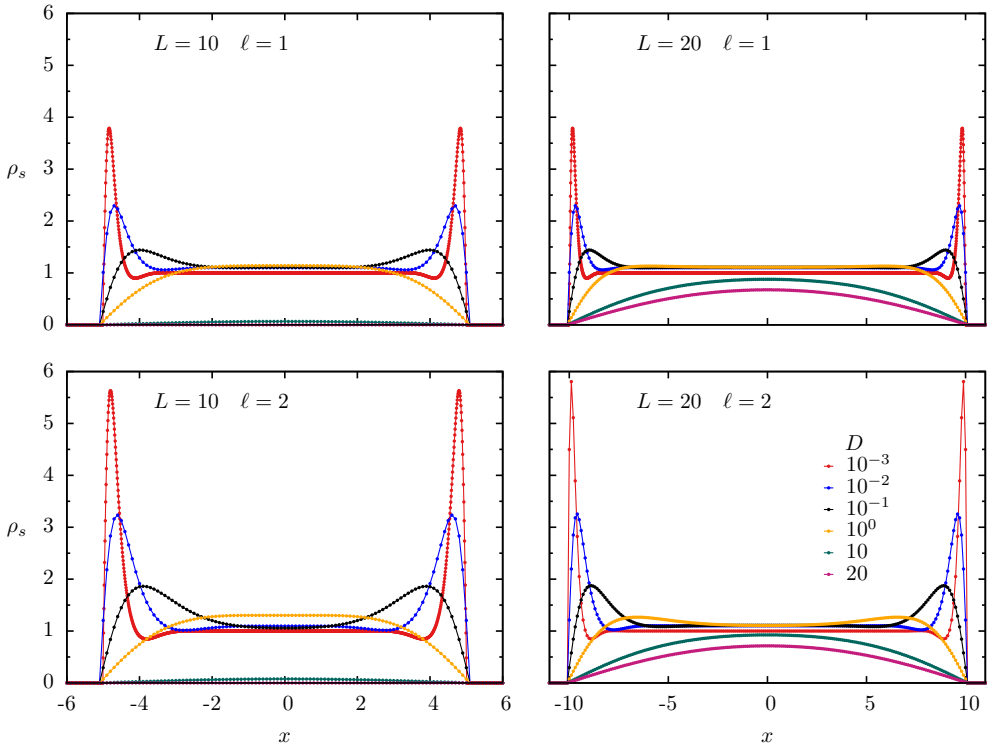

Figure B.5: **Exponential influence function γ_1.** Steady population density as a function of x obtained numerically from Eq. (2-5), for different values of L, ℓ and D described in the figure. In this case, for $L = 10$ (or 20), we have $D_c \simeq 10.1$ (or 40.4).

Large-A approximation

We will repeat here the analytical derivations made in Section 4.2.1, now for $A \to \infty$. In this case, the stationary form of Eq.(4-1) becomes

$$D\partial_{xx}\rho + a\rho - b\rho(\gamma \star \rho) = 0\,, \tag{B-2}$$

inside of the mask, while outside, $\rho(x,t) = 0$.

We Fourier transform Eq. (B-2), obtaining

$$-Dk^2\tilde{\rho} + a\tilde{\rho} - b\mathcal{F}\left\{\rho(\gamma \star \rho)\right\} = 0\,. \tag{B-3}$$

Moreover, we assume that inside the mask there is a perturbation around a homogeneous state $\rho_0 = a/b$, such that

$$\rho(x,t) = [\rho_0 + \varepsilon\rho_1(x,t)]T(x), \tag{B-4}$$

where $T(x) = \Theta(L/2 - |x|)$. Assuming $\rho(\gamma \star T) \simeq \rho$ and $T(\gamma \star \rho) \simeq \gamma \star \rho$, which is valid for $\ell \ll L$, and discarding terms of order higher than $\mathcal{O}(\varepsilon^2)$, then we

have

$$\mathcal{F}\{\rho(\gamma \star \rho)\} \quad = \quad \rho_0 \tilde{\gamma}\tilde{\rho} + \rho_0\tilde{\rho} - \rho_0^2\tilde{T}\,.$$

Therefore

$$\tilde{\rho}(k) = \frac{b\rho_0^2\tilde{T}(k)}{Dk^2 + b\rho_0\tilde{\gamma}}\,. \tag{B-5}$$

Finally, by applying the inverse Fourier transform to Eq. (B-5), we obtain the steady population density distribution for infinite A, inside the refuge, that in the particular case $\tilde{T}(k) = 2\sin(kL/2)/k$ reads

$$\rho(x) = \frac{b\rho_0^2 L}{\pi}\int_0^\infty \frac{\cos(kx)\sin(kL/2)/(kL/2)}{Dk^2 + b\rho_0\tilde{\gamma}}\,dk, \tag{B-6}$$

that unless a linear transformation has the same shape that the case for small A, inside the refuge.

In Fig. B.6, we compare results for different values of A including infinite A. Four different values of D are considered, and the kernel is γ_h.

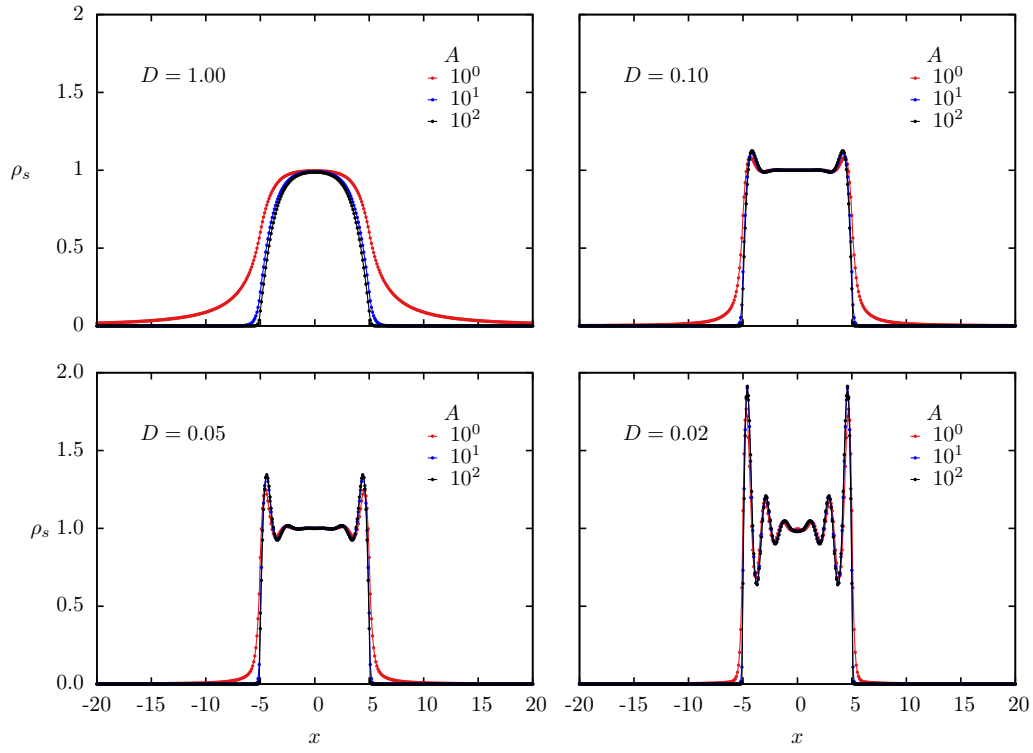

Figure B.6: **Uniform influence function γ_h, with $\ell = 1$ and $L = 10$.** Steady population density as a function of x obtained numerically from Eq. (2-5), for different values of A and D described in the figure.

C
Calculation of poles

The following figures show the poles of the mode growth rate, using the Taylor expansion of $\lambda(k)$ around $k = 0$, where $\lambda(k)$ is given by

$$Dk^2 + \sum_{n=0}^{N} \frac{1}{n!} \frac{d^n \tilde{\gamma}}{dk^n}|_{k=0}\, k^n = 0, \tag{C-1}$$

as shown in the Sec 4.3.

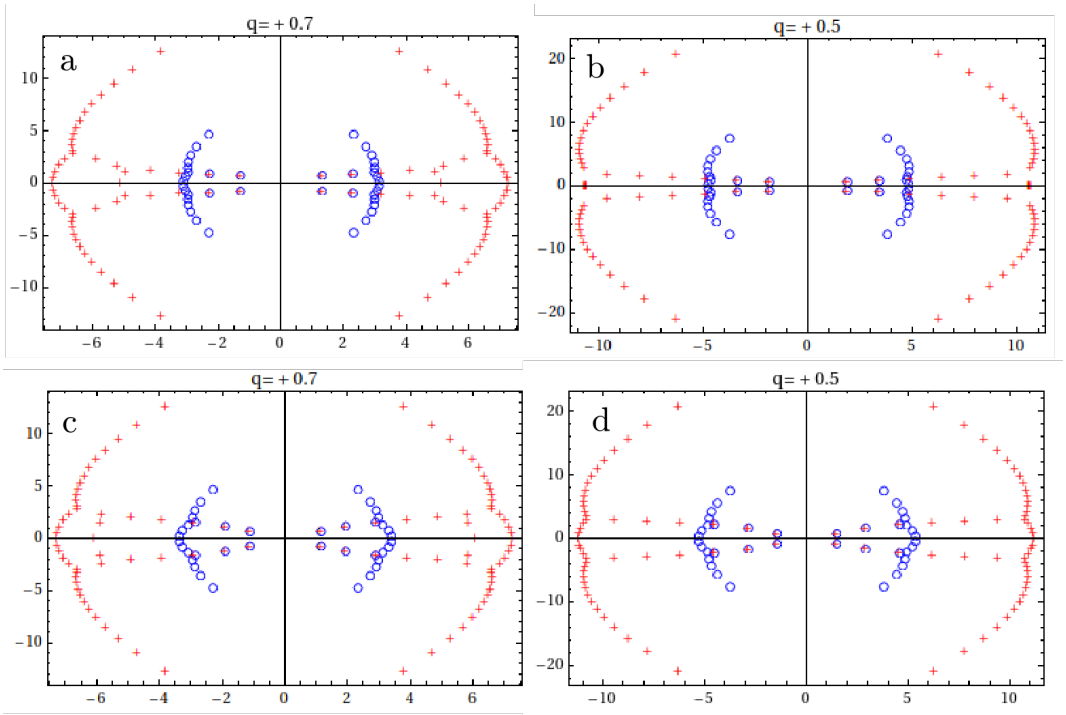

Figure C.1: **Poles of the mode growth rate $\lambda(k)$ in the complex plane for γ_q.** The influence function used was γ_q, with $\ell = 2$ and q indicated in the figure. In panels *a-b*: $D = 10^{-3}$, and *c-d*: $D = 10^{-1}$. The blue dots are for N=20, and the red crosses for N=50.

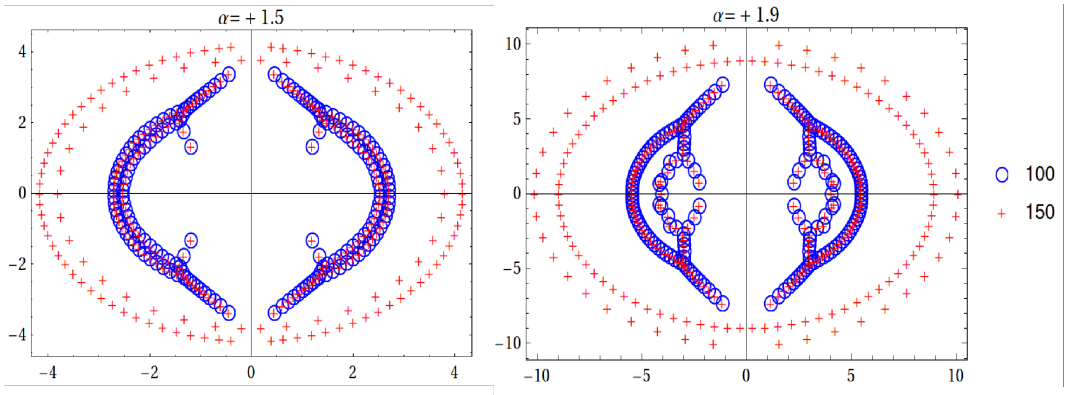

Figure C.2: **Poles of the mode growth rate $\lambda(k)$ in the complex plane for γ_α and $D = 10^{-3}$.** The influence function used was γ_α, with $\ell = 2$ and α indicated in the figure. The blue dots are for N=100, and the red crosses for N=150.